Coherent Ultrafast Spectroscopy of Noble Metal Surfaces

by

Andi Li

B.S. in Applied Physics, University of Science and Technology of China, 2016

M.S. in Physics, University of Pittsburgh, 2017

Submitted to the Graduate Faculty of the

Dietrich School of Arts and Sciences in partial fulfillment

of the requirements for the degree of

Doctor of Philosophy

University of Pittsburgh

2022

UNIVERSITY OF PITTSBURGH

DIETRICH SCHOOL OF ARTS AND SCIENCES

This dissertation was presented

by

Andi Li

It was defended on

April 5, 2022

and approved by

Jeremy Levy, Professor, Department of Physics and Astronomy

W. Vincent Liu, Professor, Department of Physics and Astronomy

Tao Han, Professor, Department of Physics and Astronomy

Sean Garrett-Roe, Associate Professor, Department of Chemistry

Dissertation Director: Hrvoje Petek, Professor, Departmental of Physics and Astronomy

Coherent Ultrafast Spectroscopy of Noble Metal Surfaces

Andi Li, PhD

University of Pittsburgh, 2022

I investigate the coherent ultrafast nonlinear photoexcitation spectra and dynamics of noble metal surfaces by angle- and interferometric time-resolved multi-photon photoemission (mPP) spectroscopy. By tuning excitation photon energies, exploring wider Brillouin zone areas, and measuring coherent polarization signals excited in the sample, I find a plethora of interesting features, which are compiled in this dissertation.

The anisotropic Ag(110) surface is studied with mPP spectroscopy, which enables the surface band structure of its unoccupied states to be recorded over a wider energy-momentum range than has been available to linear photoemission spectroscopy. I observe rich spectroscopic features which I assign to excitations involving two Shockley-type surface states at the $\overline{Y}$ point, one strongly anisotropic surface state at the $\overline{\Gamma}$ point, image potential state series, and the bulk bands.

The tunability of excitation photon energies enables studies on the bulk plasmon response of all three low-index silver surfaces. By tuning the photon energies through the epsilon near zero region, I observe signals that represent the excitation of the bulk plasmon of silver. Under intense laser field, I record that the decay of this plasmon mode excites electrons nonlinearly from the Fermi level. Such mode of plasmon decay into nonthermal electrons is important for many plasmonic applications.

I investigate the principles of mPP excitation dynamics by studying the non-resonantly excited Shockley surface (SS) state on Ag(111) surfaces with two to up to five photons. By Fourier

transformation of the interferometric mPP spectra, I discover the correlation between the polarization field excited in the sample and the final photoelectron distribution. I also identify the coherent excitation nature of the above-threshold photoemission process.

Lastly, I analyze the mPP excitation dynamics of a three-photon resonant transition from the SS to first image potential (IP1) state on Cu(111) surfaces. By Fourier filtering the excitation interferogram according to different order polarization fields, I discover signatures of optical dressing, where the optical field induces shifts and splitting of the surface eigenstates. By realizing dressing of solid-state matter, I can manipulate material band dispersions by laser fields, and change corresponding material properties on ultrafast timescales.

Table of Contents

List of Figures

List of Equations

List of Abbreviations

mPP: multi-photon photoemission, m is the nonlinear order of the photoemission process

SS: Shockley surface state

IP: image potential state

IP1, IP2: the first and second image potential state

fcc: face-center-cubic

L_{sp}, U_{sp}: lower and upper *sp*-band

E_F: energy position of Fermi level

$k_{\perp}$: momentum component perpendicular to the surface

$k_{||}$: momentum component parallel to the surface

m_{eff}: effective mass of the Bloch bands

SR: surface resonance

m_e: free electron mass

E_{vac}: energy position of vacuum level

1PP: conventional photoemission

ARPES: angle-resolved photoemission spectroscopy, often referred to as 1PP

ATP: above-threshold photoemission

ATI: above-threshold ionization

IPE: inverse photoemission

SSHG: surface second harmonic generation

STM: scanning tunneling microscopy

2PP/3PP/4PP: two/three/four-photon photoemission

$\hbar\omega_l$: photon energy

OBE: optical Bloch equation

UHV: ultrahigh vacuum chamber

MZI: Mach-Zehnder interferometer

NOPA: non-collinear optical parametric amplifier

BS: beam splitter

BBO: β-barium borate

WLG: white light generation

SHG: second harmonic generation

THG: third harmonic generation

ITR-mPP: interferometric time-resolved multi-photon photoemission

2D/3D: two/three dimension

θ: photoemission angle of the photoelectron

DLD: delay line detector

E_{kin}: electron kinetic energy

TOF: time-of-flight

Φ: work function of the sample

τ: delay time between pump and probe pulses

E_f: final state energy relative to E_F

ENZ: epsilon near zero

DOS: density of states

ω_p: bulk plasmon frequency

$\varepsilon(\omega_l)$: complex dielectric response function

MP: multiple surface plasmon

EELS: electron energy loss spectroscopy

I2PC: interferometric two-pulse correlation

FT: Fourier transform

ATS: Autler-Townes splitting

E_{SS}: SS state binding energy

MT: Mollow triplet

AT doublet: Autler-Townes doublet

IFT: inverse Fourier transform

Preface

I would like to thank everyone who helped and supported me through this long journey, without whom I could not have achieved this point in my Ph.D. research and become who I am today.

Firstly, I would like to thank my advisor Dr. Hrvoje Petek for his continuous support and encouragement for my Ph.D. work. His solid and extensive knowledge background and his rigorous and passionate scientific spirit teaches me how to do research. It is impossible to complete my research without his supervision and dedication.

I would also like to thank the other members in my thesis committee: Dr. Jeremy Levy, Dr. W. Vincent Liu, Dr. Tao Han, and Dr. Sean Garrett-Roe, for their guidance, supervision, criticism, and encouragement to improve my research.

I also appreciate all the valuable discussions and fruitful collaborations with Dr. Stefan Mathias' group in University of Göttingen, Germany (experiment), and Dr. Dino Novko and Dr. Branko Gumhalter in Institute of Physics, Zagreb, Croatia (theory).

I also need to thank all my lab mates who have always been constructing this wonderful environment where we work and become friends. I would like to thank Dr. Marcel Reutzel for his tutoring in experimental skills, cooperation in research, and the continuous collaboration after he left the group. He made it possible for me to visit University of Göttingen where the I took the data shown in Chapter 3. I would also like to thank Dr. Shijing Tan and Dr. Yanan Dai who helped and encouraged me during my tough period and from whom I learned much in every aspect. I would also like to thank all the other past and current post-docs and graduate students in this group for the valuable discussions including, but not limited to Dr. Min Feng, Dr. Jin Zhao, Dr. Chao Zhang,

Dr. Heeseon Lim, Dr. Sena Yang, Dr. Jindong Ren, Dr. Cong Wang, Karan Kapoor, Namitha Ann James, Zhikang Zhou, Atreyie Ghosh, Zehua Wang, Tianyi Wang, with special memories shared with my batchmates Namitha and Zhikang for these 6 years we have been going through together.

I would also like to thank my friends, from the department, from my undergrad school, or from whatever destiny that brought us together, who are always staying with me.

Last but not least, I would like to thank my family, especially my parents, my aunts and uncles. Their unconditional love and support is the most precious thing in my life and has always been encouraging me to go forward, no matter good times or bad. I must also memorize my grandma and grandpa, who passed away recently and a few years ago, who brought me up from my early days, but whom I cannot accompany at their side in their last days.

Day comes, day passes. Something changes, something remains.

1.0 Introduction

Ever since the Bronze Age when human first constructed metallic mirrors [1], they started to involuntarily deal with its electronic response to optical fields, which is encoded in the atomic and electronic structure of the metal surfaces, to be studied by their descendants thousands of years later. Even after decades of evolution of the experimental techniques, however, high electron density metals like noble metals (silver, copper, and gold) still serve as fertile soil for researchers to explore. In surface science, they are model systems for studying electronic band structures, many-body screening effects, and linear and non-linear light-matter interactions [2-7]. Upon chemisorption of atoms or molecules, metals acquire even more complex properties leading to, for example, interfacial charge transfer, thermionic and photoelectric emission, and catalysis [8-10]. They are also employed as substrates for atomic or molecular orbital alignment, imaging, nanostructure growth, and photocatalysis [11-16]. The understanding and design of such properties enables contributions to science and technology, for example, via plasmonic chemistry or solar energy harvesting [10, 17, 18]. Thus, a thorough understanding of the pristine, atomically-defined metal surfaces is a prerequisite for exploring and manipulating their electronic and dynamical properties, which is the goal of this dissertation.

In this chapter, I will discuss the electronic band structures of three low-index silver surfaces as a representative of single crystal noble metal surfaces. Since the (111) and (100) surfaces are widely studied by spectroscopies, I will briefly introduce their band structures and focus more on the (110) surface, which is hardly explored and present new phenomena. I will also introduce the background of photoemission, the nonlinear photoemission approach, and the organization of this dissertation.

1.1 Characteristics of Noble Metal Surfaces

1.1.1 Surface Projected Band Structures of Ag(111)

I will first introduce the surface projected band structures taking the example of Ag(111) surface, which includes bulk bands and surface states, to be discussed sequentially.

Noble metal single crystals have face-centered cubic (fcc) crystalline structures. Their reciprocal space structures are described by their first Brillouin zone, which is a truncated octahedron. The high symmetry L-point is at the center of (111) planes (Figure 1.1). For Ag(111), the silver bulk bands are projected along the momentum direction perpendicular ($k_\perp$) to the (111) surface (ΓL) and form the surface projected bulk bands, shown as brown and blue shaded areas in Figure 1.2(a), and labelled as the lower L_{sp} and upper U_{sp} *sp*-band. The surface projected *sp*-band gap on Ag(111) extends from -0.4 eV below Fermi level E_F to 3.9 eV above E_F at the $\bar{\Gamma}$ point [19]. The *d*-bands of Ag(111) start from ~-4.03 eV below E_F [20, 21].

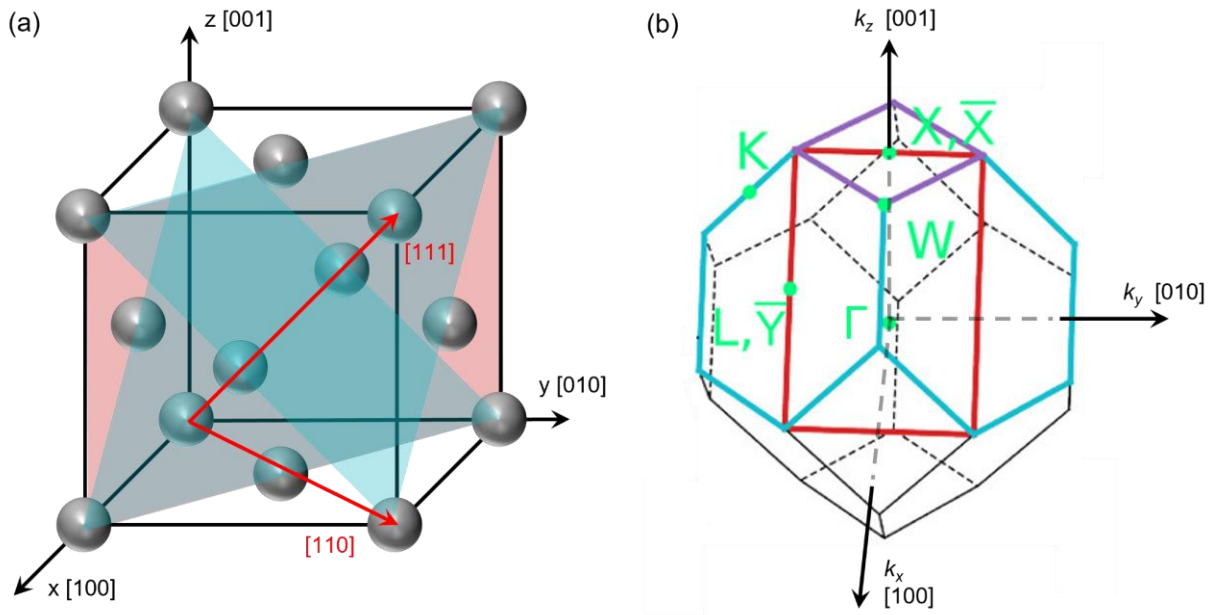

Figure 1.1 Real and reciprocal space lattice structures of fcc crystals. (a) Unit cell of the fcc crystal. The blue and red shaded areas represent the (111) and (110) crystalline planes. (b) The first Brillouin zone of an fcc crystal. In the reciprocal space, the hexagon (blue), square (purple), and rectangle (red) regions designate the (111), (100), and (110) planes, respectively.

The surface states appear where periodic crystal structures terminate at vacuum. The surface state wave functions are mainly localized in the surface region and their amplitudes decay exponentially both into the vacuum and the bulk. For noble metals, the surface states can be described by parabolic dispersion curves with $E = E_0 + \frac{\hbar^2 k_{||}^2}{2m_{eff}}$, where E_0 is the band minimum relative to E_F at the $\bar{\Gamma}$ point, m_{eff} is the effective mass of the band or the curvature of the band dispersion curve, and $k_{||}$ is the parallel momentum of electrons. $k_{||}$ is a good quantum number, which labels the band states. I will introduce the two types of surface states which are involved in my research.

The first type of surface states is the Shockley surface (SS) state on Ag(111) surfaces as shown in Figure 1.2(a), which exists on surfaces because they break the lattice periodicity of the bulk [22, 23]. It arises as a solution of the Schrödinger equation in the framework of the nearly free electron model considering the boundary conditions of a semi-infinite crystal. The SS state of the Ag(111) surface stays in the band gap and is partially occupied, lying at -0.063 eV below E_F at $\overline{\Gamma}$ point with an effective mass of 0.4 m_e where m_e is the free electron mass [4].

The other type of surface states that I study is the image potential (IP) states [24]. They originate from the Coulomb interaction of an electron with its image charge in the material bulk. The presence of an electron in front of a metal surface induces a screening image potential in the surface, which can be solved by the method of image charges [25]. Solution of the image potential term in the Schrödinger equation gives rise to a series of Rydberg-like states $E_n = E_{\mathrm{vac}} - \frac{0.85\ eV}{(n+a)^2}$ $(n = 1, 2, 3 \ldots)$, where E_{vac} is the vacuum level, n is the integer order of IP states, and a is the quantum defect [26]. For Ag(111), the first and second IP states (IP1, IP2) lie ~0.8 and ~0.2 eV below E_{vac}, with nearly free electron dispersions (IP1: m_{eff}~1.3m_e) [27]. Their wave functions are localized in vacuum several angstroms above the topmost atomic layer.

Different noble metals share similar band structures with slightly different energy positions and dispersions of the states.

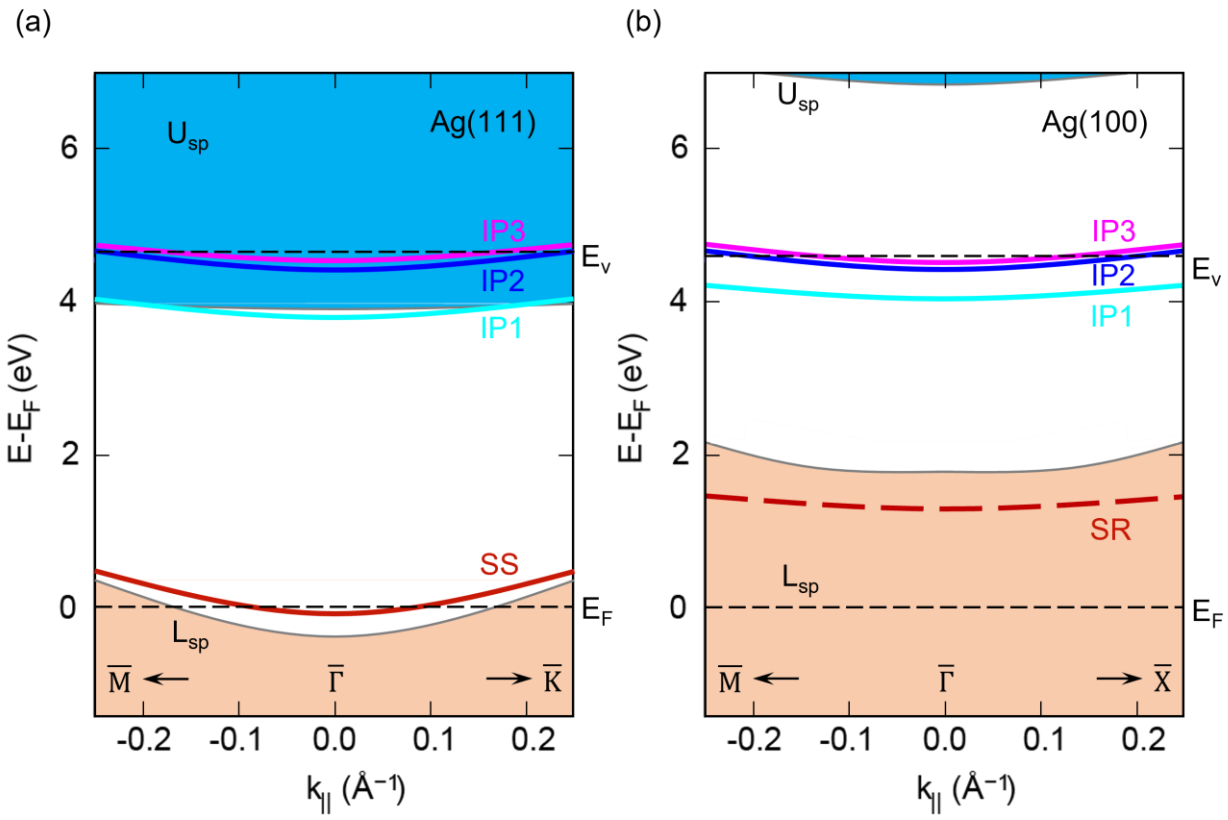

Figure 1.2 Surface projected band structures for (a) Ag(111) and (b) Ag(100) surfaces. The brown- and blue-shaded areas represent the lower and upper *sp*-bands, respectively. The brown solid line in (a) represents the Shockley surface state and the brown dashed line in (b) represents the surface resonance. A series of image potential states (IP1, IP2, IP3) is colored in cyan, blue, and magenta.

1.1.2 Surface Projected Band Structures of Ag(100)

Unlike the Ag(111) surface, the surface projected bulk bands of Ag(100) comprise the bulk bands of Ag along the ΓX direction. The L_{sp} bands extend to ~1.6 eV above E_F from where the band gap extends to ~6.6 eV above E_F at the $\overline{\Gamma}$ point [26]. The corresponding Shockley surface state, in this case, broadens into a surface resonance (SR), because it is degenerate with the bulk bands from which it derives its bulk character. The IP state series also converges to the vacuum level and IP1 and IP2 state lie at ~0.5 eV and ~0.2 eV below E_{vac} [26].

1.1.3 Surface Projected Band Structures of Ag(110)

Compared with the extensively studied Ag(111) and Ag(100) surfaces, the Ag(110) surface structure is much less well-known. Therefore, I will introduce it in detail based on previous experiments by conventional photoemission (1PP), inverse photoemission (IPE), surface second harmonic generation (SSHG) spectroscopy, and scanning tunneling microscopy (STM) [28-33]. Results from a theoretical parametrized model of Ag(110) surface by Tsirkin *et al.* [34, 35] and a band structure calculation [shown in Figure 1.3(b)] by our theoretical collaborators Novko [36, 37] are also included.

As discussed above, the Ag(111) and Ag(100) surfaces have inverted *sp*-projected band gaps centered at the $\overline{\Gamma}$ point that separate the nearly free electron conduction bands from their Mahan cones, which are derived by translating the dispersing bands from the Brillouin zone boundaries by reciprocal lattice vectors $\vec{G}$ [38]. The reciprocal vector translation enables interband excitations to occur within the *sp*-conduction band. The projected band gaps support surface states that penetrate evanescently into the bulk, and consequently have relatively long phase and energy relaxation times [3, 39-44]. The Ag(110) surface occurs at junctions of (111) and (100) surfaces, where their corresponding band gaps project in the off-normal L and X directions. This construction from pairs of proximate crystallographic planes defines the electronic anisotropy of the (110) surface, as illustrated in Figure 1.3(a) and (b). Moreover, the *sp*-band of the Ag(110) surface disperses in the bulk ΓK direction without opening an evident gap at the $\overline{\Gamma}$ point. Therefore, the image potential and other surface states become broad resonances at energies and parallel momenta where they are degenerate with the bulk *sp*-band. The wave functions of such surface resonances propagate into the bulk where they can scatter with the bulk bands, which causes their broadening. Hence, the

resonance decay rates are enhanced with respect to the evanescent surface states [3, 42, 45]. Consequently, the fast decay and resonance broadening lessens their impact as bright intermediate states in two-photon photoemission (2PP) spectra [45]. This anticipated lack of sharp surface state structure at the $\overline{\Gamma}$ point has discouraged the studies of unoccupied surface electronic structure of the Ag(110) surface. The only historical 2PP study of the Ag(110) surface at the $\overline{\Gamma}$ point reported the hot electron lifetimes for excitation below the interband threshold of 3.87 eV [46] involving primarily what was considered to be the intraband Drude absorption [47], but in reality coincided with excitation of the bulk plasmon resonance, as will become evident in Chapter 4. No 2PP spectroscopic study of the Ag(110) surface had been reported prior to my research.

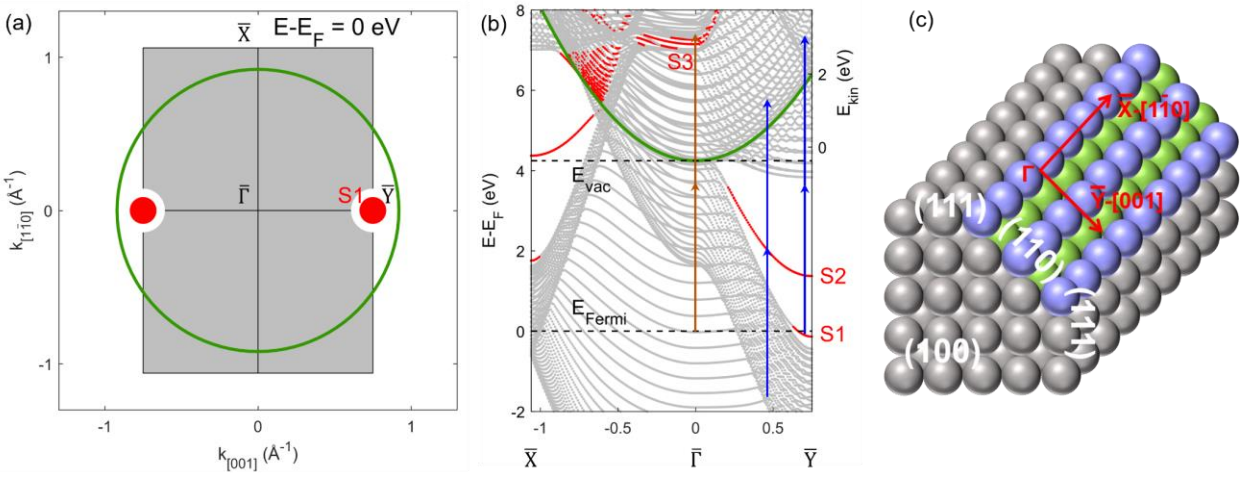

Figure 1.3 Electronic structure of Ag(110) and accessible in-plane momentum range with 3.72 eV photon in 2PP spectroscopy. (a) Two-dimensional cut through the surface projected Brillouin zone of Ag(110) at E_F; the grey region represents surface projected occupied bulk bands of the first Brillouin zone. At the $\overline{Y}$ point, the S1 state (red circles) is found in the surface projected band gap (white semicircle). The green circle depicts the photoelectron horizon, i.e., the maximum accessible in-plane momentum that can be photoemitted by two 3.72 eV photons from the Fermi level. (b) Surface projected band structure of Ag(110) calculated by our theory collaborator Novko. Grey lines represent bulk bands, while red bands are surface states, as well as

bulk bands with large surface density. Blue arrows indicate excitation of S1 and S2 states with 3.72 eV photons. Brown arrows indicate the plasmonic photoemission pathway terminating in the surface state S3. With two 3.72 eV photon excitation, only excitations above the photoemission horizon (green parabola) can be recorded. (c) The atomic structure of Ag(110) surface formed at a junction of two (111) surfaces. The blue (high) and green (low) balls emphasize the ridges and troughs of the anisotropic (110) surface.

The (110) surface is also formed by slicing the apex from a junction of two proximate (111) surfaces of an fcc lattice. The surface structure, as depicted in Figure 1.3(c), is serrated consisting of close-packed rows of atoms that belong to the two joining (111) planes and propagate in the $\overline{\Gamma X}$, or the $[1\bar{1}0]$ direction. The two contributing (111) surfaces form serried two-atoms wide upper ridge and lower trough corrugations. The corrugation of these ridge-and-trough close-packed atomic rows runs in the $\overline{\Gamma Y}$, or the $[001]$ direction [48]. These features define the Ag(110) surface structure, which has made it an epitome for its anisotropic dielectric response to polarized optical fields [49-54]. The two (111) plane junctions support two Shockley surface states within a band gap that, according to our DFT-based calculation, extends from -0.4 eV to 3.8 eV similar to the one on the (111) surface, but with band minima at the $\overline{Y}$ point (0.75 $Å^{-1}$) [right part of Figure 1.3(b) where the surface states are colored red]. The lower energy one is the partially occupied Shockley surface state (S1) with its band minimum at -0.1 eV below E_F and a nearly isotropic band mass of 0.26 m_e [29], which has similar characteristics to that of the (111) plane, and is localized predominantly within the corrugation troughs [48]. The upper one is an unoccupied surface state (S2) running on top of the Ag atom ridges [48], and with a band minimum at ~1.7 eV above E_F and mass of ~0.7 m_e [31]. Despite the surface atomic and electronic structure being anisotropic, the surface state band masses are isotropic with our ability to measure them.

The surface states at the $\overline{Y}$ point have been investigated by 1PP, IPE, and mPP [29, 30, 33, 55]. They also resonantly enhance the SSHG signal and can be imaged as tunneling resonances in STM [28, 31, 56]. The S2←S1 transition, which is one-photon resonant for photon energy $\hbar\omega_l$~1.7 eV, enhances the nonlinear SSHG as well as four-photon photoemission (4PP) spectra [28, 55]. An unusual aspect of this transition is that it is excited by the in-plane optical field polarized in the [001] crystalline direction. Although the surface parallel optical fields must nominally pass through zero in the near-surface region [2], the spatial separation of S2 and S1 at single-atom-high ridges and troughs on the Ag(110) surface [48] requires their coupling by in-plane surface fields that are orthogonal to the serration [28, 36]. This optical transition thus entails charge transduction both normal and parallel to the surface.

In the less investigated orthogonal $[1\overline{1}0]$ direction, according to our calculation, the $\overline{X}$-point band gap extends from 1.6 eV to 7.0 eV above E_F and hosts two surface states at 1.8 eV and 4.4 eV [36]. While the latter has been confirmed in the IPE spectra [30], the former has not been reported. We have also found a new surface state S3 located at an energy of ~7.6 eV above E_F at the $\overline{\Gamma}$ point within a previously unknown minigap in the *sp*-band. The minigap is confirmed by our electronic band structure calculations. I will describe this previously unknown aspect of the Ag(110) band structure in detail in Chapters 3 and 4. These are some of the established, but in many respects uncommon or previously unknown features of the Ag(110) surface.

1.2 Multi-Photon Photoemission Background

Angle-Resolved photoemission spectroscopy (ARPES; often referred to as 1PP) is an effective and conventional technique of mapping occupied electronic structures of solids and solid

surfaces [57-60]. Because the energy and parallel momentum of primary excited electrons are conserved during photoemission processes, information from photoelectron spectra can be converted to the energy and $k_{\|}$ dispersions of bands in the electronic structure. By increasing the power of the laser and decreasing the photon energies to below E_{vac}, nonlinear photoemission processes such that electrons absorb more than one photon quanta to overcome work function can occur. We refer to such processes as mPP (m = 2, 3, 4…), where m indicates the nonlinear order or the number of photon quanta absorbed to induce photoemission. Among different nonlinear order mPP processes, 2PP spectroscopy is widely applied to study the unoccupied band structures and interband transitions [e.g., bulk transition from L_{sp} to U_{sp} bands on Ag(111)] [39, 61-63]. Moreover, by changing the relative delay time between two pulses and conducting time-resolved measurements, 2PP can also be applied to study excitation dynamics of the system, including lifetime of the intermediate states [41, 64-67], dephasing of polarization fields [68, 69], and so on. An example is that, on Ag(111) surfaces, IP1 state has been measured to have ~30 fs lifetime [41].

In Figure 1.4, I show a typical energy- and $k_{\|}$-resolved 2PP spectra of Ag(111) taken with $\hbar\omega_1$ =3.32 eV ultraviolet photons. 2PP spectroscopy of Ag(111) in this energy range is well documented in literature [62, 63]. The 2PP spectra are dominated by the SS state and the *sp*-band, which are, respectively, detected by non-resonant and resonant (L_{sp} to U_{sp}) coherent two-photon absorption. The SS state is occupied in a narrow $k_{\|}$-range where it exists below E_F [excitation diagram in Figure 1.4(b)] [63]; the $k_{\|}$ asymmetry of the surface and bulk photoemission intensities are discussed in Ref. 63. The IP1 state is detuned from resonance with SS, and hence, appears with a low intensity; significantly, it appears only in the $k_{\|}$-range where SS state is occupied, which indicates that it is populated by non-resonant one-photon excitation from SS [70], rather than by

resonant two-photon excitation from the bulk L_{sp}-band, which is possible, but as an inelastic process would not limit $k_{||}$-range.

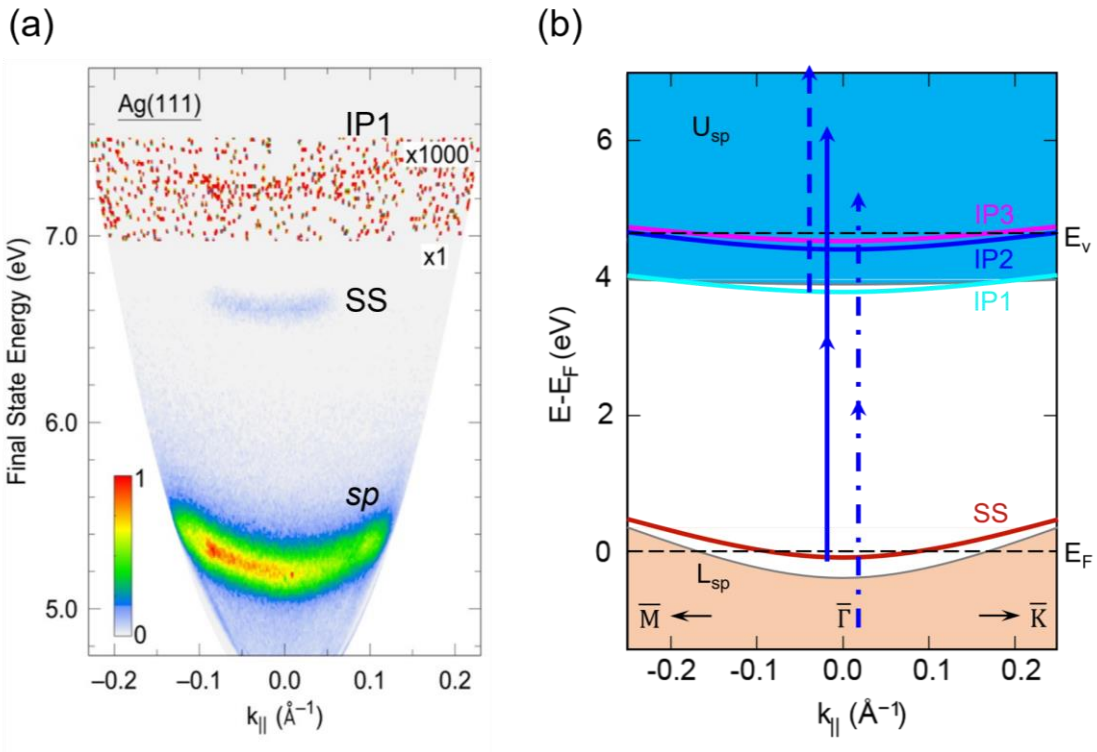

Figure 1.4 2PP excitations of the Ag(111) surface. (a) Ag(111) 2PP spectrum taken with *p*-polarized $\hbar\omega_l$=3.32 eV photons. The normalized color intensity scale is based on photoelectron counts.The SS state and the bulk *sp*-transition are observed. A weak IP1 signal is also observed with 1000 times magnified intensity (the intensified signal shows mostly single or no counts). (b) The excitation diagram of the three excitation channels in (a). The dashed line, solid line, and dash-dotted line represent excitations from IP1, SS, and bulk transitions, respectively.

Higher nonlinear order photoemission processes (3PP, 4PP) can be excited by lower energy photons (e.g., visible to infrared energy range) and higher laser power because electrons need to absorb more photon quanta to overcome the work function. For example, a report from our group studied 3PP excitation from the SS and IP1 state of Ag(111), and described the formation of an

excitonic state following the two-photon resonant excitation from the SS to IP1 state [19]. Moreover, above-threshold photoemission (ATP) can also occur when electrons are excited above the work function by absorbing more photons than the minimum amount needed. ATP is the solid-state analogue of above-threshold ionization (ATI) of atomic and molecular gases. It will appear as replicas of the lower order signals and stay at one or more photon energies above them [71-74].

1.3 Organization of the Dissertation

Based on the kind of spectrum discussed in Figure 1.4, my dissertation concerns similar measurements on different sample surfaces. I tune the excitation photon energies and multiple photon orders to explore different unoccupied electronic structures and to study their electron dynamics. The next chapters of this dissertation is organized as follows.

In Chapter 2, I will first introduce the instruments used throughout the experiments at the University of Pittsburgh, including the ultrafast laser and the ultrahigh vacuum ARPES systems to perform angle-resolved mPP spectroscopy. Then the time-of-flight momentum microscope system I used at the University of Göttingen for part of the research is also discussed briefly. I will also introduce the optical Bloch equation (OBE) model I used to simulate the experimental data.

My research falls into two parts: studying the electronic structure and excitation pathways of surfaces under optical excitation, and studying the coherent dynamics of those excitations. I will introduce the results that belong to the former part in Chapters 3 and 4, and that to the latter part in Chapters 5 and 6.

In Chapter 3, I will discuss the nonlinear excitation spectra of an anisotropic Ag(110) surface where I systematically recorded 2PP-4PP spectroscopic features that are assigned to either the single particle band structures or collective responses of the surface.

In Chapter 4, I will report the plasmonic photoemission response of three low-index silver surfaces and show that except for the Einsteinian single particle excitation pathways, light can also excite the bulk plasmon modes of silver, which contributes to photoemission spectra in a surprising non-Einsteinian manner. This plasmonic photoemission can also occur through final states of single particle origin.

In Chapter 5, I will discuss the coherent excitation dynamics of non-resonantly excited Shockley surface states on Ag(111). I will combine experiment data with OBE simulation to showcase how the polarization field excited in the sample coherently correlates to the final photoelectron distributions in 2PP-4PP. I will also show how this correlation improved our understanding of the mechanism of above-threshold photoemission.

In Chapter 6, I will discuss the effect of time periodicity of optical field on surface excitation dynamics. By analyzing Fourier-filtered coherent dynamics signals of a resonant IP1←SS transition, I found signatures of optical dressing of surface states on Cu(111) surface, which can be explained by Floquet theory and Autler-Townes splitting. Such dressing can tune the electronic band structure of surfaces with external optical field, thereby enabling us to control the electronic properties of materials.

The last Chapter 7 will summarize the results of this dissertation.

2.0 Experiment and Simulation Techniques

In this chapter, I will introduce the photoemission apparatus for conducting experiments and the OBE models for simulating the nonlinear optical excitations. The photoemission apparatus consists of two parts, the excitation laser source, and the ultrahigh vacuum (UHV) photoemission spectroscopy system. To excite photoemission, I use a femtosecond laser system, which is broadly tunable in the ~270-900 nm wavelength range with 20~30 fs pulse durations working at a 1 MHz repetition rate. By producing delay-scanning of pump-probe pulse pairs with a Mach-Zehnder interferometer (MZI), I am able to temporally resolve the coherent nonlinear dynamics in the sample under photoexcitation. To detect and analyze photoelectrons, a hemispherical electron energy analyzer ARPES system is integrated in an UHV chamber where the in situ sample cleaning and preparation is performed. I will also introduce the momentum microscope setup for collecting photoelectrons at the University of Göttingen in Germany where I was invited for a research visit. Concerning the interferometric time-resolved measurements, I will describe the OBE methods to simulate and interpret the experimental results.

2.1 The Ultrafast Laser System

2.1.1 The Non-collinear Optical Parametric Amplifier (NOPA) System

The schematic of our femtosecond laser system is shown in Figure 2.1. The fundamental laser source is a Yb-doped fiber laser (Impulse, Clark-MXR), which can operate at a variable

repetition rate, but in my experiments, I typically used 1 MHz repetition rate. The fiber laser produces a train of 250 fs duration pulses at 1035 nm wavelength (fundamental frequency, ω_0) with an energy of 1 μJ per pulse. The output is used to pump the NOPA system, which produces broadly wavelength tunable and intense ultrafast laser pulses.

The NOPA is constructed based on design of Dr. Eberhardt Riedle at the University of Munich [75]. To operate the NOPA, the fiber laser output is directed into three separate beams. A polarized beam splitter (BS) sends 80% of the total power to two β-barium borate (BBO) crystals to generate second ($2\omega_0$; second harmonic generation, SHG; λ=517 nm) and third ($3\omega_0$; third harmonic generation, THG; λ=345 nm) harmonics of pump light, while the remaining 20% is focused onto a sapphire single crystal plate for white light generation (WLG). The white light continuum spectrum is split into two colors by a dichroic mirror that transmits (reflects) above (below) 650 nm. These two colors provide seed pulses for the NOPA processes using SHG and THG pumps. The choice of 650 nm is determined by the fact that both SHG and THG can amplify this color, but it can be inconvenient when light in this transition region is necessary. The dichroic mirror can be changed to a different transition color or removed to generate light in this transition region. The longer wavelength part (>650 nm) is overlapped in space and time with the SHG $2\omega_0$ beam in another BBO crystal. The phase matching condition of the BBO crystal which is established by requirement to conserve the pump, seed, and the output light momenta is set so that a portion of the white light is parametrically amplified by the $2\omega_0$ pump beam. The wavelength of the output signal light is tuned by the spatial and temporal overlap of the pump and white light beams, ranging from 650-900 nm (1.91-1.38 eV) for the $2\omega_0$ beam line. Similar process also amplifies the shorter wavelength part of white light (<650 nm) by nonlinear interaction with the THG $3\omega_0$ pump light to generate output in the 500-650 nm (2.48-1.91 eV) range. These

interactions are referred to as the NOPA processes [75, 76]. At the output of the NOPA system, the frequency chirp of these pulses is set to compensate for the dispersion of the optical system to thereby achieve the minimum pulse duration of ~20-30 fs at the point of their nonlinear interaction, which usually occurs at the sample, or at an additional external SHG nonlinear crystal. These dispersion-compensating mirrors are set as matched pairs because their design dispersion has a wavelength dependent oscillation, which can be minimized by using in pair. If necessary, the NOPA output can be further frequency-doubled by appropriate SHG-BBO crystals to extend the accessible laser wavelength range to 270-450nm (4.59-2.76 eV).

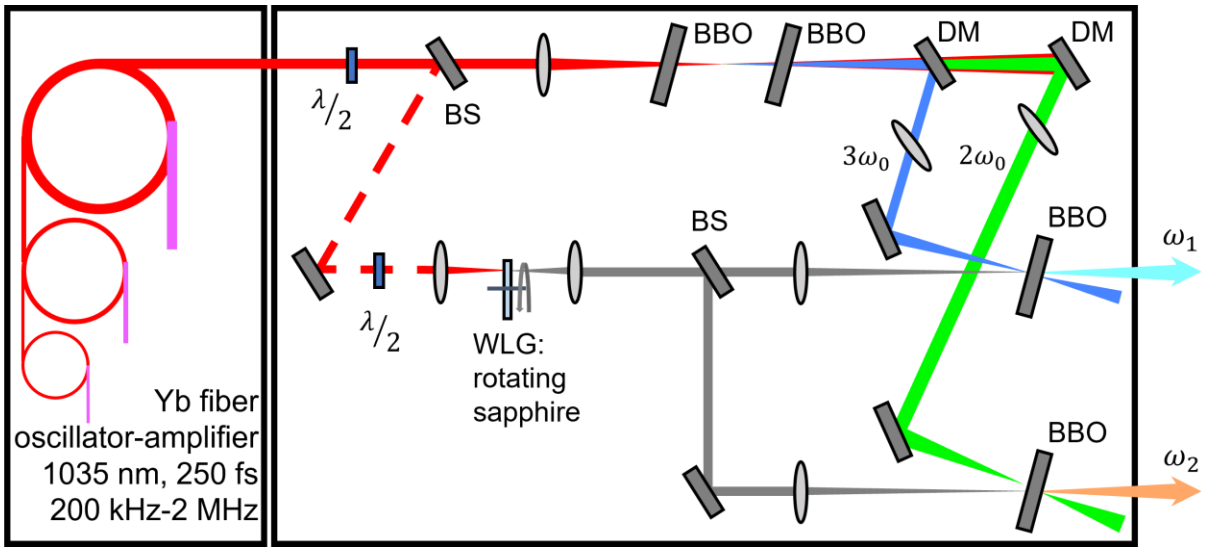

Figure 2.1 Schematic of the NOPA laser system. λ/2: half waveplate; BS: beam splitter; DM: dichroic mirror.

2.1.2 The Mach-Zehnder Interferometer

Electronic measurement devices are not sufficiently fast to resolve electron dynamics on the femtosecond (fs, 10^{-15} s) or attosecond (as, 10^{-18} s) time scales. Therefore, to achieve fs- or even as-resolution, I make use of the optical autocorrelation method, which employs a mechanical

scanning of an optical delay line to scan delay between pump and probe pulse pairs that excite and probe nonlinear interactions in the sample to perform time-resolved measurements. The delay is established by setting separate optical pathlengths for the pump and probe pulses within an MZI. The laser light is directed through the MZI (shown in Figure 2.2), where the first BS splits incoming optical pulses into two paths, and the second BS recombines them to proceed collinearly at its output. One of the paths has retroreflecting mirrors on a translation stage. Piezoelectric scanning of the mirror stage scans the relative path length and therefore the experimental pump-probe pulse delay time. The MZI has two nearly identical outputs, which produce pulse pairs, whose relative intensities oscillate with a π-phase shift when the two pulses overlap in time. In other words, when the two pulses are in-phase, they interfere constructively, and their combined output is directed to the sample. When they are out-of-phase, however, the reflected pulse experiences a π-phase shift, such that both pulses are combined and directed towards the calibration system. The calibration signal is sent through a monochromator, where the wavelength narrowing of the output spectrum at the center wavelength of the laser pulse generates a sinusoidally oscillating interference signal over the time duration of the delay scan. This interference signal whose intensity is detected by a photodiode, has a sharp profile with maxima arriving periodically at the center wavelength of the pulse. This comb of intensity maxima is used to calibrate time delay between pump and probe pulses. Although the pump-probe delay scan can be nonlinear, particularly due to nonlinearity of the piezoelectric actuator scanning, the recorded interference pattern provides a frequency comb for calibrating and linearizing the time delay scan. The MZI delay scan calibration defines the pulse delay to <50 as resolution for typical delay scan conditions. By measuring the photoelectron spectrum as a function of the pump and probe delay time, we can record the coherent polarization and population dynamics leading to a nonlinear

multiphoton photoemission process. This is referred to as the interferometric time-resolved mPP (ITR-mPP) method [77].

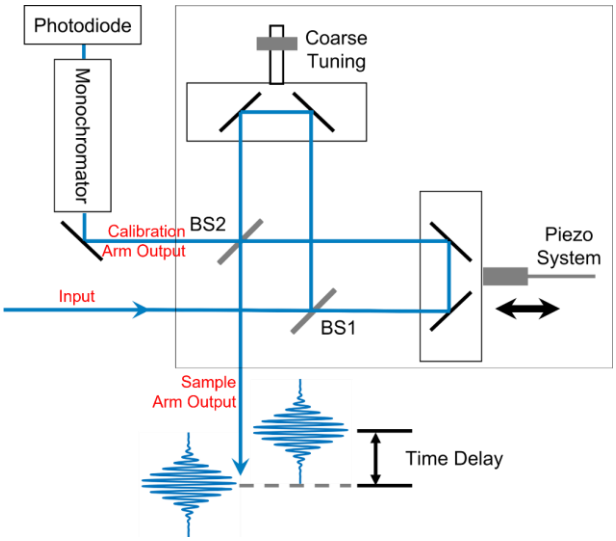

Figure 2.2 Schematic of the MZI. The blue lines indicate the optical pulse pathways.

2.2 The Ultrahigh Vacuum Chamber and Electron Detection System

2.2.1 The UHV System

Photoemission experiments are performed in UHV environment to keep sample free of contamination and electronics to operate without environmental perturbation. The UHV system for photoemission experiments consists of a load-lock chamber for introducing and storing samples under UHV conditions, and an analysis chamber for conducting photoemission experiments. The UHV conditions are sustained at a pressure of $<1.0\times10^{-10}$ mbar by a pumping system consisting of a rotary vane roughing pump and a turbomolecular pump for achieving high

vacuum, and an ion pump which attains the ultimate vacuum to enable studies of clean surfaces. In addition, periodic operation of a titanium sublimation pump helps to remove residual impurities that accumulate over time to maintain the necessary vacuum.

The analysis chamber is the locus of experiments, where most functional components of experiments are located. The sample is held in place for various experiments by a sample manipulator. The manipulator is located on the top of the chamber and is equipped with the sample ion bombardment heating and liquid N_2 cooling. It provides 4-dimensional sample positioning including 3 dimensions of translation and 1 dimension of azimuthal rotation around the axis of the manipulator. The manipulator can locate the sample at different positions for transferring, sample preparation, adsorbate deposition, and photoelectron emission. On the chamber circumference, several viewports hold evaporators for deposition of different kinds of adsorbates onto the sample, a sputter gun for cleaning the sample by ion ablation, a thin-film thickness monitor for deposition calibration, and other instrumentation for the sample preparation or evaluation. One of the viewports holds a plano-convex lens, which both forms the vacuum barrier, as well as acts to focus the excitation laser onto the sample. It is made of CaF_2 to maximize transmission bandwidth from infrared to vacuum ultraviolet light, and to minimize dispersion.

2.2.2 Sample Preparation

Samples used throughout this dissertation are single crystal noble metal surfaces with different crystal facets, including Cu(111), Ag(111), Ag(100), Ag(110), and Au(111). They are prepared by repeated cycles of sputtering and annealing. Ar^+ ion bombardment of sample surface sputters material to expose clean surface. Typical ion sputtering conditions expose the surface to 3 μA emission current with 1500 V acceleration voltage for 20 min. Subsequently, the surfaces are

annealed by electron-beam bombardment heating at 550 K (all Ag and Au surfaces) or 800 K [Cu(111)] for 10 min to remove the sputtering damage and embedded Ar atoms, and restore the surface crystallography. Repeated cycles of cleaning and annealing can prepare a well-ordered atomically clean and flat surface. The surface quality can be judged by the correct work function energy, low signal of secondary electrons at the work function edge, and sharp surface state features in mPP spectra.

2.2.3 The Angle-Resolved Photoemission Spectroscopy System

The ARPES system is the essential part of the photoemission experiments. It consists of a hemispherical electron energy analyzer and a two-dimensional (2D) delay line electron counting detector that records photoelectron counts and for each, the *x* and *y* coordinates, for the analysis of its energy and parallel momentum.

The working principles of our PHOIBOS 100 hemispherical electron energy analyzer, from SPECS GmbH, is shown in Figure 2.3. After photoexciting the sample, the emitted electrons with a wide angular distribution are focused into the lens system. The analyzer electron lens has an angular acceptance angle of ±13°. The collected electrons are imaged onto the entrance slit of the hemispherical electron analyzer, and the electrons with different photoemission angles (θ) are focused along the slit. The slit width can be set mechanically to define the instrument energy resolution. Reducing the slit width improves the energy resolution, but also decreases the signal intensity. For high electron density materials like metal surfaces, the narrowest 0.2 mm×20 mm entrance slit is typically used. The hemispherical lens of the analyzer acts as an energy filter. The static electric potential difference between inner and outer hemispheres deflects electrons according to their kinetic energies. Lower energy electrons (red arrows in Figure 2.3) are deflected

to the inner hemisphere while higher energy ones (blue arrows in Figure 2.3) towards the outer hemisphere. Electrons with energies out of the preset energy range cannot pass through the energy filter. Under the 0.2 mm×20 mm entrance slit width and also considering the photoelectron energy range of interest (which is usually 4-6 eV in my experiments), the energy resolution of the analyzer is ~0.1-0.2 eV. Thus, electrons with different energies and photoemission angles (parallel momenta) are dispersed to land in different regions of a 2D microchannel plate image intensifier to record energy-$k_{||}$ dispersion spectra. The intensified pulses from each photoelectron, which are amplified by at least 10^7, are counted by pulse counting electronics (detector). The detection system can count at most one photoelectron per pulse pair. Thus, high laser pulse repetition rate is necessary to obtain high signal-to-noise spectra.

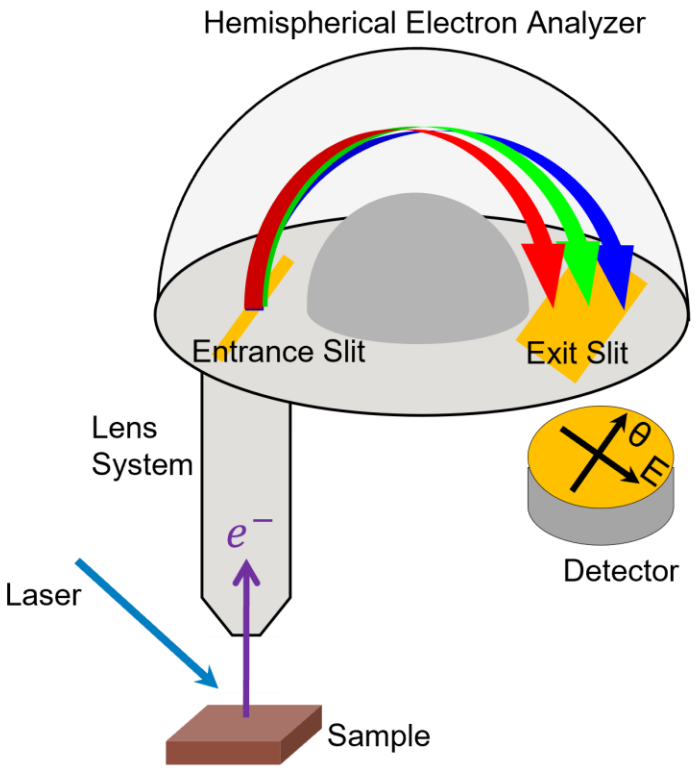

Figure 2.3 Schematic of the hemispherical electron energy analyzer.

The two-dimensional delay line detector (2D-DLD) consists of two sets of overlayered meandering wire delay lines (X and Y) where one set is rotated by 90 degrees with respect to the other (Figure 2.4). The electronic signal that is captured by the 2D delay line grid travels to both ends of the wires. By recording the relative time delay Δt_x and Δt_y of the pulse arrival for photoelectron hitting at position (x, y), the spatial coordinates can be determined, to define its energy and photoemission angle θ. The photoemission angle is converted to the parallel momentum $k_{||}$ through $k_{||} = \frac{\sqrt{2m_e E_{kin}}}{\hbar} \sin\theta$, where E_{kin} is the photoelectron kinetic energy and θ is the angle between photoelectron momentum direction (or the direction of the analyzer optical axis) and surface normal.

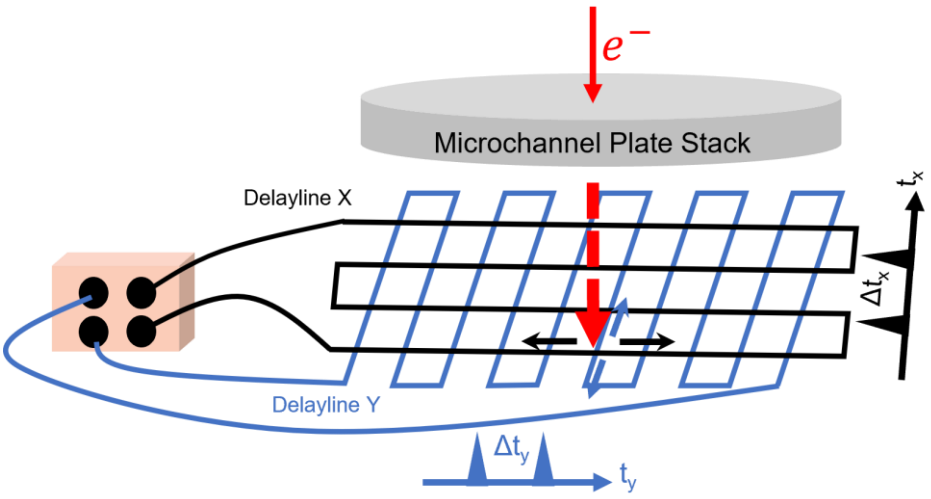

Figure 2.4 Schematic of the 2D-DLD structure.

2.2.4 The Momentum Microscopy System

Part of my research (Chapter 3) was performed with a METIS time-of-flight (TOF) momentum microscope from Surface Concept GmbH at the University of Göttingen. I measured the anisotropic band structure of Ag(110) by recording three-dimensional (3D) 2PP data consisting of energy vs. in-plane k_x and k_y parallel momenta [78, 79]. Here, I briefly explain the principles of momentum microscopy measurements (Figure 2.5). At the University of Göttingen, the ultrafast laser excitation pulses are directed onto the sample at an angle of incidence of 68° from the surface normal. To collect photoelectrons from a solid angle of up to 2π centered on the surface normal, an extractor voltage of 10 kV is applied with respect to the sample. This collects all of the photoemitted electrons within the full photoemission horizon [78, 80].

The photoemission horizon refers to the kinetic energy that is tied in the surface parallel motion, so that it cannot do work against the work function because the $k_{||}$ of electrons passing through a solid-vacuum interface is conserved [71, 81]. Since $E_{kin} = \frac{\hbar^2}{2m_e}\left(\frac{k_{||}}{\sin\theta}\right)^2 \geq \frac{\hbar^2 k_{||}^2}{2m_e}$, to detect 2PP or mPP, photoelectrons must possess kinetic energy which is larger than their kinetic energy components tied in the surface parallel motion to be detected. It will cause photoemission signals to have a parabolic low-energy cut-off, as predicted in Figure 1.3, and will be shown in Chapter 3.

The long TOF drift tube enables measuring electron energies defined by the time it takes them to reach the delay line detector. As explained already, the DLD records the arrival time and the (x, y) position of each photoelectron, from which one obtains its kinetic energy and 2D parallel momentum information (k_x, k_y) [78, 80]. The energy- and momentum-axes are calibrated as explained in Ref. 78.

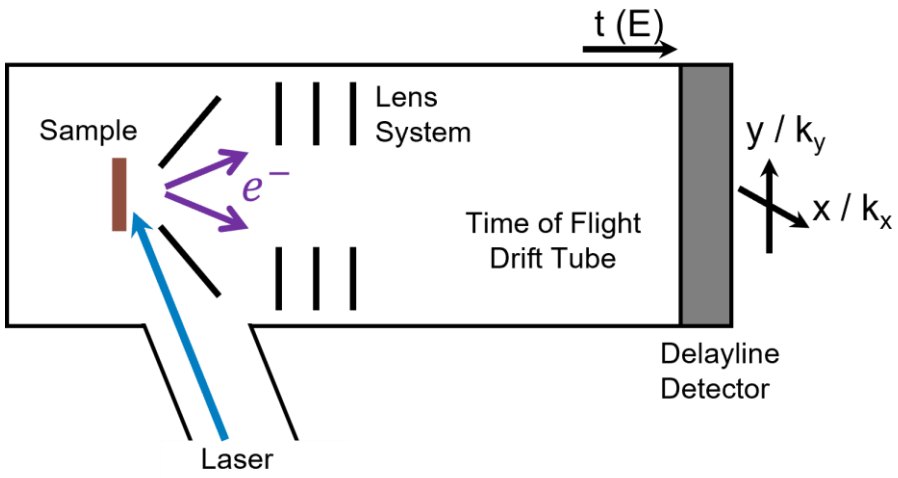

Figure 2.5 Schematic of the TOF momentum microscope.

2.3 The Optical Bloch Equation Simulation

In photoemission experiments, many mPP processes involve interband transitions between different energy eigenstates in the surface band structure. This can make such processes suitable to model and analyze their excitation dynamics by OBE method, which originates from research on optical transitions between atomic eigenstates [41, 43, 68, 82-85]. Here I will introduce the approach based on a 4-level system applied to 3PP study of Ag(111). Applying the method to fewer or more levels can be generalized straightforwardly.

As shown in Figure 2.6(a), 3PP can excite electrons from SS state to vacuum continuum via nonresonant excitation, or via IP1 state. In the OBE model that I employ, the excitation proceeds from the initial state, which is typically the SS state, via real intermediate state (e.g., IP1), and terminates in the final state (FS) that exists in photoemission continuum [Figure 2.6(b)]. To construct the 3PP OBE model, however, we need to include a virtual intermediate state (VS) to describe the multi-photon transition process. The distinction between the real and virtual

intermediate states will be discussed later. Excitation of this four-state system by light fields is described by transition dipole coupling between the neighboring states; the deexcitation of states is described phenomenologically, as will be discussed later.

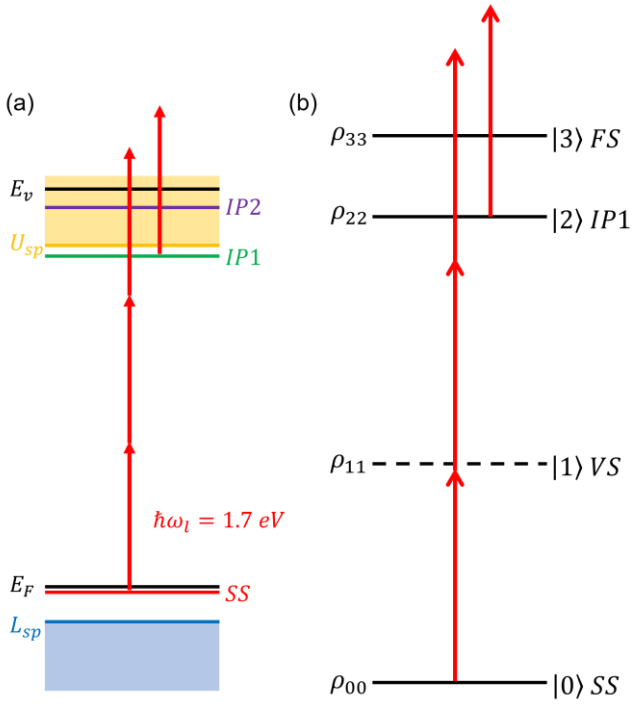

Figure 2.6 (a) The energy level diagram for 3PP excitations, shown for Ag(111). (b) The corresponding four-level system adopted in the OBE model.

OBE is based on the density matrix formalism [Equation (2.1)] where the diagonal density matrix elements ρ_{mm} represent the population of each energy eigenstate (states $|m\rangle, m = 0\text{-}3$) and off-diagonal elements $\rho_{mn\ (m\neq n)}$ represent the coherences between states $|m\rangle$ and $|n\rangle$. Coherence between each pair of states is induced by the light field and leads to population transfer between them. Because density matrix is Hermitian, the symmetric off-diagonal matrix elements are

complex conjugates, $\rho_{mn} = \rho_{nm}^{*}$. Thus, for a 4-level system, the density matrix has 10 independent elements.

$$\rho = \begin{pmatrix} \rho_{00} & \rho_{01} & \rho_{02} & \rho_{03} \\ \rho_{10} & \rho_{11} & \rho_{12} & \rho_{13} \\ \rho_{20} & \rho_{21} & \rho_{22} & \rho_{23} \\ \rho_{30} & \rho_{31} & \rho_{32} & \rho_{33} \end{pmatrix} \tag{2.1}$$

Time evolution of a density matrix is described by the Liouville–von Neumann equation (2.2)

$$\frac{\partial \rho}{\partial t} = -\frac{i}{\hbar}[H(t), \rho] \tag{2.2}$$

where

$$H(t) = H_0 + H'(t) \tag{2.3}$$

H_0 is Hamiltonian of the unperturbed system with

$$H_0|m\rangle = \hbar\omega_m|m\rangle, \tag{2.4}$$

and $H'(t)$ is the perturbation of the system by the interaction with the optical field. The interaction is approximated as dipole coupling

$$H'(t) = -p \cdot E(t) \tag{2.5}$$

where $p = -er$ is the dipole moment. External field $E(t)$ that causes the interaction is assumed to have Gaussian envelope with

$$E(t) = e^{-4\ln 2\left(\frac{t}{T_0}\right)^2} \cos(\omega_l t) + e^{-4\ln 2\left(\frac{t-\tau}{T_0}\right)^2} \cos[\omega_l (t-\tau)] \tag{2.6}$$

where T_0 is the pulse duration (full width half maximum, FWHM), ω_l is the field frequency, and τ is the delay between otherwise identical pump and probe pulses. Such field will describe interferometric two-pulse excitation, where the delay τ is scanned interferometrically and variation of the final state population is recorded.

Exponential decay terms are added empirically in Equation (2.2) to get the Liouville–von Neumann equation with dissipation terms (2.7) to describe the deexcitation of populations and coherences that usually occur through interactions with the environment bath states that are not included in the simulation. The relaxation is described by a matrix, where T_{mm} is the decay time of state $|m\rangle$ population representing, for example, inelastic electron-electron scattering process, and $T_{mn\ (m\neq n)}$ is the dephasing time of the coherence between two states, which also involves interactions with the environment. Because dephasing can include inelastic scattering processes as well as quasi-elastic electron-photon and defect scattering, the total dephasing time consists of two parts $\frac{1}{T_{mn}} = \frac{1}{T_{mn}^*} + \frac{1}{2T_{mm}} + \frac{1}{2T_{nn}}$, where T_{mn}^* is referred to as the pure dephasing time (quasi-elastic scattering processes) [5-7, 86]. For real states, depopulation times T_{mm} are set to infinity for the occupied ground state and the final state, while for the real intermediate state, it is their lifetime, which can be extracted from experiment data. For example, a lifetime of the IP1 state on Ag(111) of 30 fs has been determined in two-color 2PP time resolved measurements [41]. The pure dephasing times T_{mn}^* between real states are set to be in a range between 15 and 1500 fs. For virtual states, a very fast 1 fs depopulation time and a very long pure dephasing time ($\gg 1$) are used since their only role is to enable the ladder climbing process in OBE. In actuality, the ladder climbing process involves nonresonant interaction with higher lying states. Such interactions occur on short time scales that are defined by the energy-time uncertainty.

$$\frac{\partial \rho}{\partial t} = -\frac{i}{\hbar}[H(t), \rho] - \frac{\rho}{T} \tag{2.7}$$

The OBE calculation is usually simplified by transforming to the rotating frame where only the terms evolving with an angular frequency ω_l are kept, and terms evolving at $2\omega_l$ are set to zero, because they do not have measurable effects on the final state excitation. After the rotating wave

approximation (RWA) that retains only the slowly varying components of the density matrix, we get the final OBE expressions given in equations (2.8) and ((2.9) for the off-diagonal and diagonal terms.

$$\frac{\partial \rho_{mn}}{\partial t} = -\left[i(\omega_m - \omega_n - (m-n)\omega_l) + \frac{1}{T_{mn}}\right]\rho_{mn} - \frac{i}{\hbar}\sum_k H'_{mk} e^{i(m-k)\omega_l t}\rho_{kn} + \frac{i}{\hbar}\sum_k H'_{nk} e^{-i(n-k)\omega_l t}\rho_{mk} \tag{2.8}$$

$$\frac{\partial \rho_{nn}}{\partial t} = -\frac{\rho_{nn}}{T_{nn}} - \frac{i}{\hbar}\sum_k H'_{nk}(e^{i(n-k)\omega_l t}\rho_{kn} - e^{-i(n-k)\omega_l t}\rho_{nk}) \tag{2.9}$$

Although OBE is a simple model which does not account for collective effects, e.g., many-body screening of metals to the optical field, solving OBE can still qualitatively simulate the mPP process and extract the effective population and coherence information to interpret signatures of coherent excitation as well as excited state population decays in the experiment data. Note that for surface states OBE is a reasonable approach because $k_{||}$ is a good quantum number, meaning that the dipole transitions of each state in a band can be treated independently, but for bulk states, where $k_{\perp}$ is not conserved in an optical transition, it is difficult to capture the inhomogeneous broadening of the interacting bands by the OBE method.

3.0 mPP from the Anisotropic Ag(110) Surfaces

Interrogating the different excitation pathways in a sample is a fundamental goal in photoemission experiments. In this chapter, I investigate the strongly anisotropic near-surface electronic structure of Ag(110) by multidimensional momentum microscopy and explain the origin of different spectroscopic features in mPP spectra ($m \geqslant 2$), comprehensively. These mPP features arise from surface-surface, surface-bulk, and bulk-bulk optical transitions, and their assignment to either single particle band structure or collective excitation modes of silver will be discussed specifically. The content in this chapter is based on publications in Physical Review B and New Journal of Physics [55, 87].

3.1 Overview of the Photoemission Data

Among the data of pristine Ag(110) surfaces, 2PP spectra are taken with a time-of-flight momentum microscope [78, 80] to gain access simultaneous to 3D information on photoelectron energy and 2D parallel momenta ($k_{[1\bar{1}0]}$ and $k_{[001]}$). These measurements are augmented by 2D energy-momentum 3PP/4PP spectroscopy taken with a hemispherical electron energy analyzer with the Ag(110) surface aligned such that its $k_{[001]}$ direction is in the optical plane.

2PP data taken with the momentum microscope is excited with $\hbar\omega_l$=3.43-3.86 eV, *p*-polarized, ~40 fs light pulses. Figure 3.1 shows the 2PP momentum microscopy data of the pristine Ag(110) surface with *p*-polarized, $\hbar\omega_l$=3.72 eV excitation. In normal emission, the accessible final state, E_f, range of the 2PP measurements is limited by the work function of Ag(110) of Φ~4.25 eV

on the low end, and E_f=2$\hbar\omega_l$+E_F = 7.4 eV by 2PP from the Fermi level at the high end [36]. The momentum microscope collects the entire $k_{||}$ photoelectron distribution for energies and momenta above the photoemission horizon, which is discussed in Chapter 2. The effect of photoemission horizon is evident in the data as the parabolic cut-off photoemission signals at low-energy boundaries in Figure 3.1(b, d); below this threshold no momentum conserving photoemission can occur [55]. Figure 3.1(a) shows selected energy slices of data from a 3D spectrum, where the color scale expresses the photoemission yields at several final state energies, E_f, relative to E_F for the accessible in-plane momenta $k_{[1\bar{1}0]}$ and $k_{[001]}$ (directions are indicated). In Figure 3.1(b, d), the 3D data are presented as $E_f(k_{||})$ 2D cross sections through fixed $k_{[1\bar{1}0]}$=0 Å^{-1} and $k_{[001]}$=0 Å^{-1}, respectively. The recorded data terminate above the E_f=2$\hbar\omega_l$+E_F [Figure 3.1(c)].

The spectra in Figure 3.1(b, d) show evidence of one feature at $\bar{\Gamma}$ point, which is assigned to plasmonically excited surface state S3 [36, 37, 87], and seven additional transitions involving strongly dispersive bands that extend over the entire accessible Brillouin zone. As we will show, four of these features (B1-B4) involve transitions between the bulk *sp*-bands of Ag(110), whereas the remaining ones are assigned to S1 and S2 surface state excitations, in some cases involving optical transitions from or to the bulk bands in the mPP process [55, 87]. The bulk bands that optically couple to surface states must have a large spatial overlap with the latter.

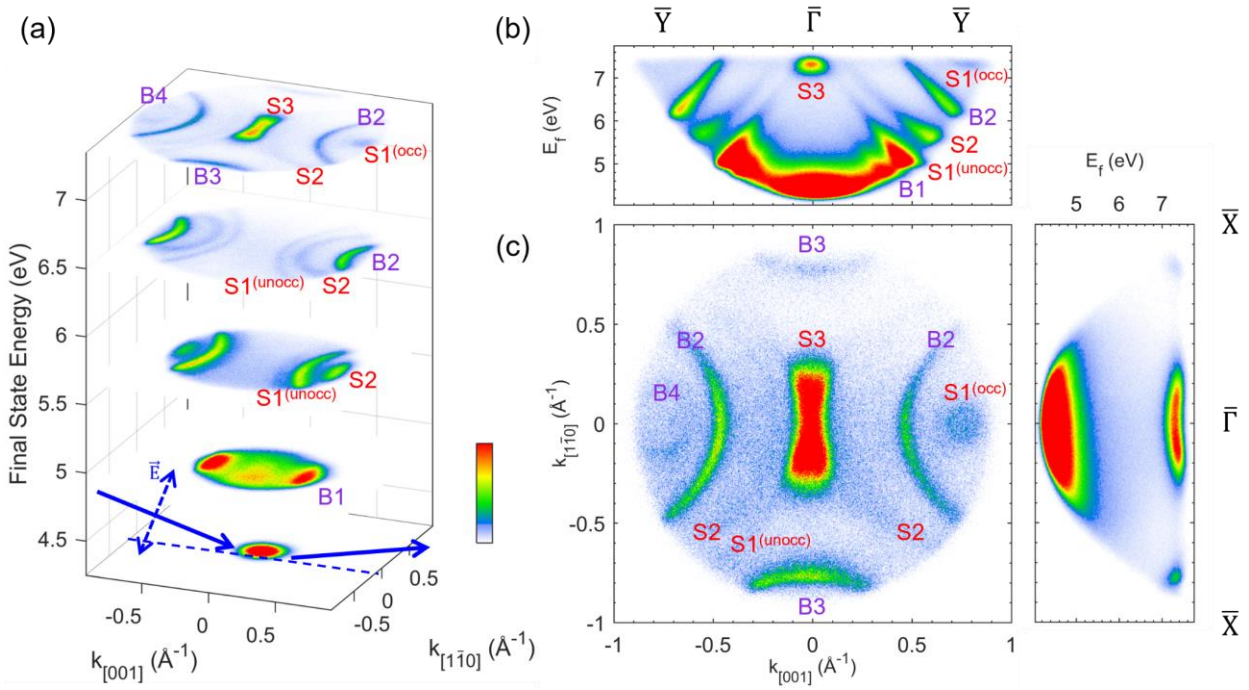

Figure 3.1 2PP momentum microscopy of Ag(110) with *p*-polarized $\hbar\omega_l$=3.72eV light. (a) 3D data stack illustrating the photoemission yield (color-coded) as a function of energy (bottom to top slices are cut at 4.25, 4.85, 5.65, 6.5, and 7.35 eV final state energy) and in-plane momenta. Solid blue arrows indicate laser propagation direction and dashed blue arrow indicates electric field direction of *p*-polarized light. (b) $E_f(k_{[001]})$-resolved spectra cut at $k_{[1\bar{1}0]}$= 0 ± 0.07 Å^{-1} window. (c) ($k_{[001]}$, $k_{[1\bar{1}0]}$)-resolved spectra cut at $E_F+2\hbar\omega_l$, or E_f =7.44 ±0.04 eV window. (d) $E_f\left(k_{[1\bar{1}0]}\right)$-resolved spectra cut at $k_{[001]}$=0 ± 0.07 Å^{-1} window. Purple and red text labels indicate transitions assigned to specific bulk and surface states, respectively.

To further characterize the optically coupled transitions, I increase the nonlinear order of photoemission process by tuning the photon energies between $\hbar\omega_l$=1.47-2.28 eV. These excitations in the visible region cannot excite one-photon momentum conserving bulk interband transitions in silver, which become available at ~3.88 eV [21]. Instead, the high fluences available from ultrafast lasers can excite interband transitions in higher order 3PP and 4PP processes [88]. However, as discussed in Chapter 2, our ARPES system has a limited angular acceptance range

which can only collect photoelectrons from a certain range of Brillouin zone. Thus, to measure additional features across the Brillouin zone, we need to rotate the sample around the axis normal to the optical plane to collimate electrons with different photoemission angles towards the analyzer. We can get a full Brillouin zone mapping by combining photoelectron spectra taken at different sample rotation angles. To eliminate the discontinuous jumps due to the assembly of spectra, we can normalize each spectrum to its background noise level before assembling.

Such kind of assembled spectra taken at $\hbar\omega_l$=2.09 and 1.72 eV are shown in Figure 3.2(a, c) and the extracted peak dispersions are plotted in the band structure as thick colored solid lines in the left (3PP) and right (4PP) parts of Figure 3.2(b). In addition, in Figure 3.2(a, c), red and orange dashed parabolas, representing S1 and S2 states, respectively, are plotted using the parameters extracted from the 2PP momentum microscopy data; they are plotted at the 3PP and 4PP final state energy positions, showing a good agreement in band dispersions between data obtained from photoemission processes of different nonlinearities.

Furthermore, in 3PP and 4PP, we detect spectral densities belonging to the image potential state series (IP1, IP2) centered at the $\overline{\Gamma}$ point [blue and brown dashed parabolas in Figure 3.2(a, c)]. The IP states are resonant with the bulk *sp*-band at the $\overline{\Gamma}$ point, leading to their broadening, and therefore, weak signal strengths [45], but become surface states at larger $k_{||}$, where they gain intensity because they enter into the projected band gaps.

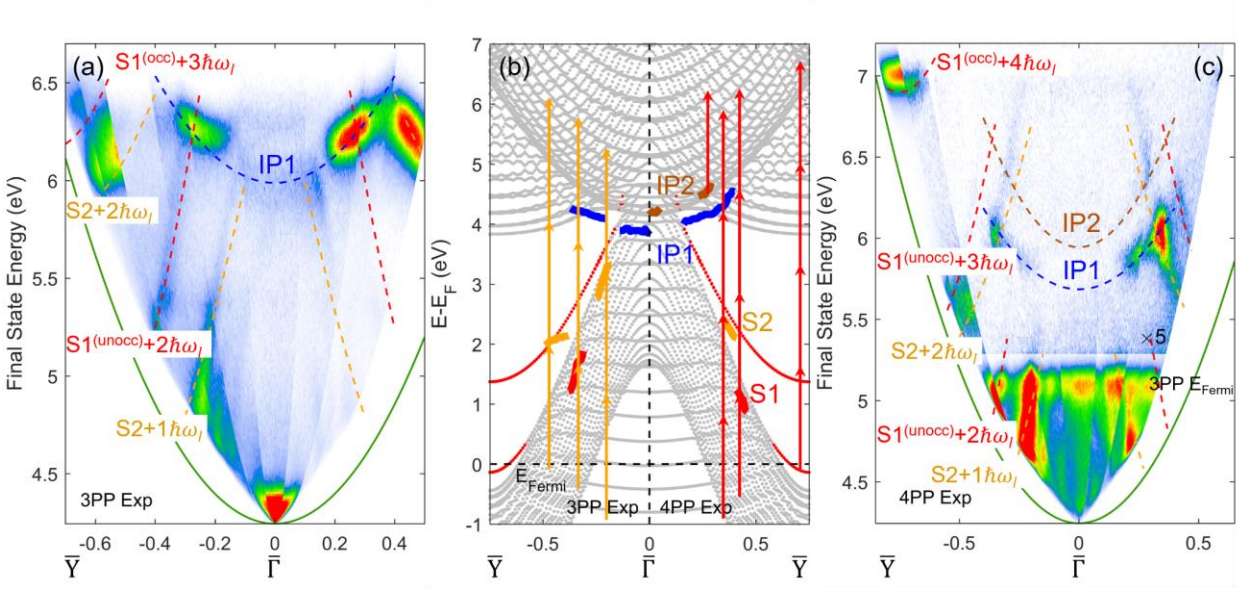

Figure 3.2 $E_f(k_{[001]})$-resolved 3PP and 4PP spectra of Ag(110) excited with (a) $\hbar\omega_l$=2.09 eV and (c) $\hbar\omega_l$=1.72 eV light. Surface state dispersions in (a) and (c) are extracted and plotted in the left and right parts of (b) that contains the calculated Ag(110) surface and bulk band structure in $\overline{\Gamma Y}$ direction. Specific assignments are indicated in the figure. Green solid lines in (a) and (c) represent photoemission horizon. Discontinuous jumps in the mPP intensity [(a) and (c)] are caused by the assembly of multiple $E_f(k_{[001]})$ measurements at different sample angles with respect to the electron analyzer optical axis. The signal below 5.16 eV in (c) is from 3PP and above is from 4PP excitation (amplified by five times).

In the following sections, I will elaborate assignments of the observed transitions involving the surface states S1-S3, the image potential states IP1 and IP2, and the bulk bands B1-B4 in different orders of excitation.

3.2 Surface States Response

3.2.1 The Partially Occupied Shockley Surface State S1

The Shockley surface state S1 is occupied in the range $k_{[001]} \sim 0.75 \pm 0.08$ Å^{-1}, from its band minimum at the $\overline{\text{Y}}$ point up to E_F. Therefore, it can act as an initial as well as an intermediate state in a nonlinear photoemission process, depending on the $k_{||}$ of detection. In Figure 3.1(b), two-photon absorption lifts the electrons from the occupied range of the S1 state [S1$^{(occ)}$] to $E_f \sim$ 7.3 eV. The effective mass of the band S1$^{(occ)}$ around 0.2-0.4 m_e is consistent with its literature value of 0.26 m_e from a 1PP study [29]. The unoccupied part of the S1 band [S1$^{(unocc)}$] also participates as an intermediate state in mPP processes when it is excited from the bulk *sp*-band continuum. This will be discussed further in conjunction with the 3PP and 4PP measurements.

The S1 state can be detected in the photoemission experiment only when electrons are excited above the photoemission horizon [compare blue arrows and green parabola in Figure 1.3(b)]. Consequently, in the constant energy cuts through the 2PP spectra [Figure 3.1(a, c)], it appears as concentric circles or circle arcs centered at the $\overline{\text{Y}}$ point (0.75 Å^{-1}). The abrupt constraint of the photoemission horizon allows S1$^{(occ)}$ to appear entirely as a complete circle, whereas S1$^{(unocc)}$ appears as an arc centered on $k_{[001]}$ at a larger distance from the $\overline{\text{Y}}$ point [Figure 3.1(a, c)]. As the final state energy increases, the arc diameters increase towards the $\bar{\Gamma}$ point.

Similar excitations as in 2PP also occur in higher order 3PP and 4PP processes with infrared to visible light. The S1$^{(occ)}$ state can be excited by absorbing 3 or 4 photons, labelled as '$S1^{(occ)}+3\hbar\omega_l$' and '$S1^{(occ)}+4\hbar\omega_l$' features at the $\overline{\text{Y}}$ point in Figure 3.2(a) and (c), respectively. Note that in 1.72 eV excitation data [Figure 3.2(c)], 3 photons is enough to excite electrons in S1$^{(occ)}$

above vacuum level, but it cannot be detected because of the photoemission horizon unless it undergoes momentum scattering within the sample to transfer kinetic energy from the surface parallel to normal motion, and thereby alter their photoemission angle [55]. We also emphasize that the enhancement of '$S1^{(occ)}+4\hbar\omega_l$' signal results from the 1-photon resonance between $S1^{(occ)}$ and S2 states at ~1.7 eV excitation [55]. Thus, in this way, spectroscopic information on surface bands that are otherwise hidden below the photoemission horizon, become accessible in higher-order mPP processes. Instead of the conventional way of using extreme ultraviolet photons to explore features deep in the sample Brillouin zone which requires more complicated instruments, we can exploit the non-linear response of the sample with lower energy photons.

Once the S1 band crosses the Fermi level, the $S1^{(unocc)}$ state between the $\overline{Y}$ and $\overline{\Gamma}$ points can be populated through one photon absorption from the *sp*-band and then be detected in 3PP and 4PP. Similar to the 2PP case, however, it requires absorption of two more photons to overcome the work function and thus is labelled as '$S1^{(unocc)}+2\hbar\omega_l$' in Figure 3.2(a, c). Moreover, its corresponding ATP signal, '$S1^{(unocc)}+3\hbar\omega_l$', where it is excited above Φ by absorbing an extra photon, is observed in 1.72 eV excitation data [Figure 3.2(c)] above the 3PP Fermi level edge signal. We mention here that a 2-photon resonant transition from $S1^{(unocc)}$ to IP1 states resonantly enhances the '$S1^{(unocc)}+3\hbar\omega_l$' signal, as will be documented later. Furthermore, the IP2 state can also come into a 2-photon resonance with the $S1^{(unocc)}$ state, but the contribution of this process is considerably weaker such that it is not clearly evident in the color scale display in Figure 3.2(c). A similar excitation process is more evident from the S2 state, as we show next.

3.2.2 The Unoccupied Shockley Surface State S2

Similar to the unoccupied part of the S1 state, the S2 state contributes to 2PP signal only as an intermediate state dispersing upward from the band minimum at ~1.6 eV above E_F [Figure 3.1(b)]; its recorded effective mass 0.7 m_e matches the literature value from scanning tunneling spectroscopy [31]. In Figure 3.3(b), we plot the photon energy dependent data of the S1 and S2 states from two-photon momentum microscopy. In agreement with an Einsteinian photoemission process, the slope of E_f with respect to the $\hbar\omega_l$ at a constant $k_{\parallel}$ depends on the number of photons needed to photoemit from the last real state that is populated in an mPP process, instead of the total number of photons that excite it. Thus, the $S1^{(occ)}$ state, serving as an initial state, and the $S1^{(unocc)}$ and S2 states, serving as intermediate states in 2PP excitation, appear with slopes of 2.11, 1.35, and 1.15, respectively, as shown in Figure 3.3(b). The deviations from integer slope values may indicate that other unknown states participate in the multiphoton process, or simply reflect the uncertainties of determining the slopes from narrow spectral ranges.

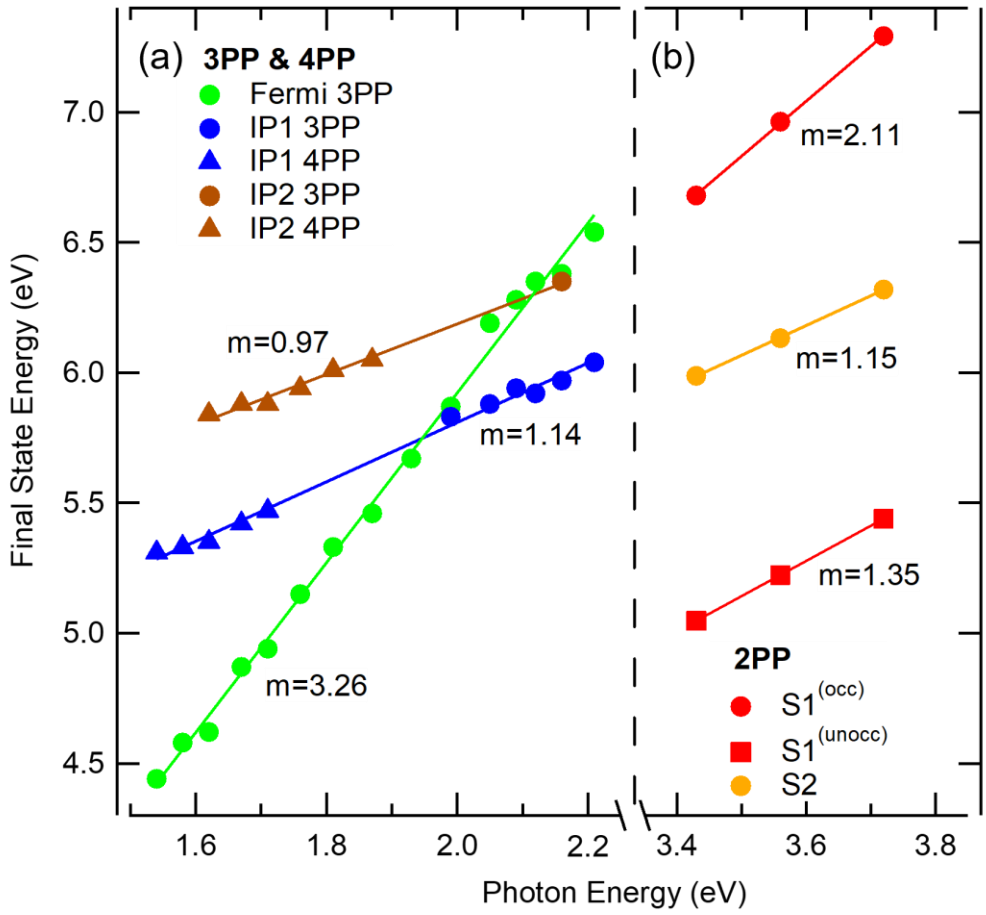

Figure 3.3 Photon energy dependent E_f-energies of (a) the IP states and the Fermi level in 3PP and 4PP and (b) the surface states S1 and S2 in 2PP. 3PP and 4PP peak energies are extracted at $k_{[001]}$=0 Å^{-1} ($\overline{\Gamma}$ point). S1$^{(unocc)}$ and S2 energy positions are extracted at an intermediate momentum of $k_{[001]}$=0.37 Å^{-1} while S1$^{(occ)}$ energy positions are extracted at the $\overline{Y}$ point ($k_{[001]}$=0.75 Å^{-1}). The slope *m* values given in the figure report the number of photons needed to photoemit electrons from specific states.

In the $\hbar\omega_l$=2.09 eV 3PP excitation data [Figure 3.2(a)], different momentum regions of the S2 state are excited with the same order 3PP process, but involving different excitation pathways. For instance, the component of the 'S2+1$\hbar\omega_l$' signal, which is located at a smaller $k_{[001]}$ and a higher energy is populated by 2-photon absorption from the bulk *sp*-band, and detected by

photoemission of one more photon, while in the case of 'S2+2$\hbar\omega_l$' signal, S2 is populated by one photon absorption from the *sp*-band followed by two-photon photoemission. The 'S2+1$\hbar\omega_l$' 3PP signal is also observed in $\hbar\omega_l$=1.72 eV excitation data [Figure 3.2(c)], and at one photon higher energy, the 'S2+2$\hbar\omega_l$' feature appears once more as a 4-photon ATP process where S2 is emitted by 2 photons. The 2 photon excitation from S2 is enhanced when it involves one-photon resonant transitions to the IP states [71], but in this case it does not involve ATP. For example, a 1-photon resonant transition between IP1 and S2 states at $k_{[001]}$ ~ 0.3 Å^{-1} enhances the signal intensity at the crossing point of blue and orange dashed parabolas in Figure 3.2(c). Similar enhancement also occurs for the S2 and IP2 resonance, but with lower intensity.

3.2.3 The Anisotropic Surface State S3 at the $\bar{\Gamma}$ Point

Contrary to S1 and S2, the S3 state exists at the $\bar{\Gamma}$ point at an energy of ~7.6 eV above E_F within a minigap in the *sp*-band in the final state energy region, with a highly anisotropic distribution that is derived from the real space anisotropy of the Ag(110) surface [36]. The density functional electronic structure calculation [37] predicts such a state at E-E_F ~ 7.14 eV within a mini gap spanning the interval of 7.0-7.3 eV [S3 in Figure 1.3(b)].

In Figure 3.1(c), S3 appears as a bright, narrow rectangle. In the serrated $\overline{\Gamma Y}$ direction the calculated band structure of Ag(110) surface predicts the S3 band to be highly dispersive with a band mass of 0.11 m_e [36]. The consequence of the strong dispersion is that it limits the S3 spectral density to a narrow $|k_{[001]}| < 0.05$ Å^{-1} region of high density-of-states (DOS) near its band minimum. In the smooth $\overline{\Gamma X}$ direction, however, it is much less dispersive with a calculated band mass of 1.75 m_e, which gives it a large DOS over a larger $k_{[1\bar{1}0]}$ range. Ergo, it appears as an

elongated rectangle in the momentum microscope images in Figure 3.1(c). DFT calculations in Figure 3.4 of 2D DOS reproduce this unusual rectangular-shaped high DOS region at E_f =7.2 eV, which confirms the highly anisotropic S3 state dispersions. Further orbital analysis shows that the S3 state has mainly contributions from the *s* and *d* atom-projected states (not shown). The charge density calculation also shows that the S3 state mostly locates in the first two atomic layers (Figure 3.5), and electrons occupying this state can either decay from the surface into vacuum, or decay into the bulk, where they have a small but finite density. The calculated S3 state density shows that it overlaps with the near-surface bulk bands.

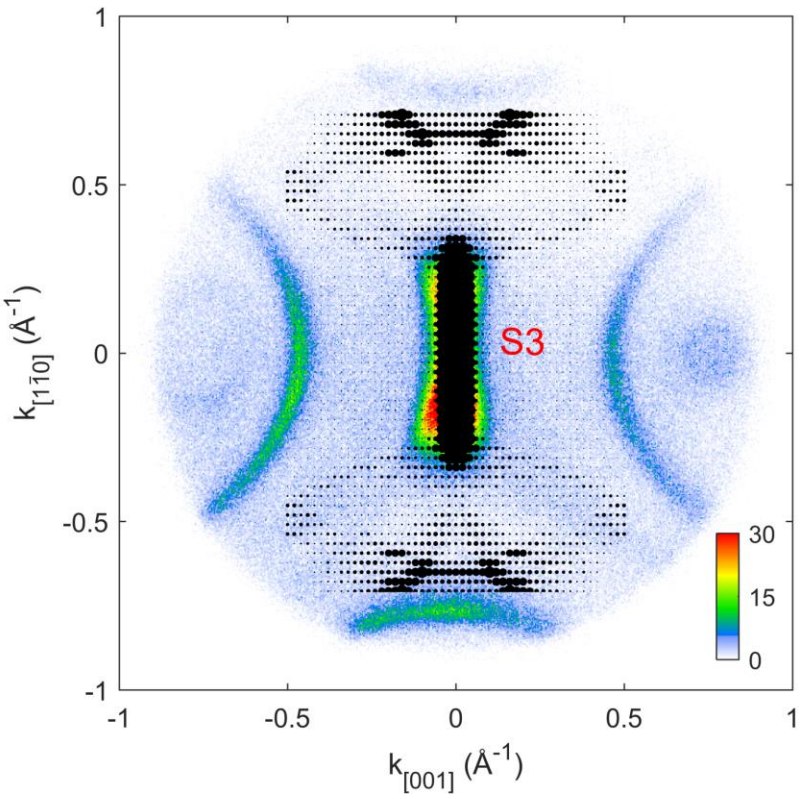

Figure 3.4 $k_{[001]}$ and $k_{[1\bar{1}0]}$-resolved momentum microscope spectrum cut at E_f=7.2 eV from Figure 3.1(a). The superposed black dots with different radii represent the calculated 2D ($k_{[001]}$, $k_{[1\bar{1}0]}$) DOS at 7.2 eV

above Fermi level. Areas with large DOS, therefore, cause the black dots to overlap. The calculated DOS dispersion reproduces the rectangular shape of the S3 state.

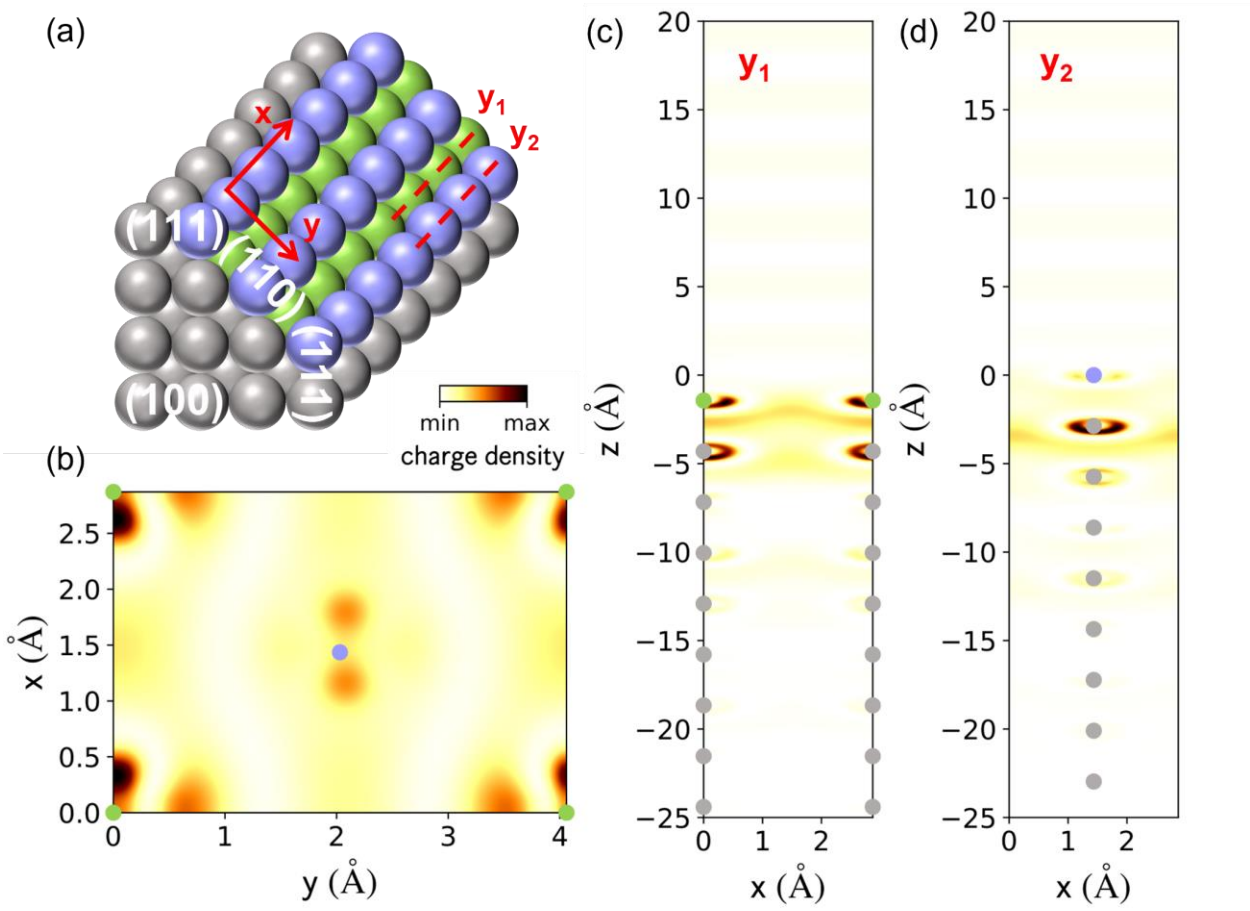

Figure 3.5 The calculated charge density of the S3 surface state. (a) Atomic structure of Ag(110) surface indicating the trough (y_1) and ridge (y_2) atom rows. (b-d) Charge density calculations in the *x*-*y* plane (integrated in first two layers in the *z* direction) and in the *z*-*x* plane cut at y_1 (troughs) and y_2 (ridges), respectively. The blue (high) and green (low) balls indicate ridge and trough atom positions of the anisotropic (110) surface. The gray balls indicate the bulk atoms.

The excitation mechanism of S3 state involves the bulk plasmon response of the Ag(110) surface, which is the focus of Chapter 4, so I only describe the S3 state characteristics here and will elaborate on the excitation mechanism later.

3.3 Image Potential States Excitation

The IP states or resonances of Ag(110) have only been reported in inverse photoemission [30], not in mPP experiments. In 2PP momentum microscopy data shown in Figure 3.1, we do not observe spectroscopic signatures of these states, even though the excitation light in the $\hbar\omega_l$=3.43-3.86 eV energy range is sufficiently energetic to excite them from the *sp*-bulk bands at the $\overline{\Gamma}$ point. By contrast, in Figure 3.2, the IP states do appear as the penultimate intermediate states in the 3PP and 4PP processes, where their nearly free electron dispersions are represented by the blue and brown dashed parabolic lines in Figure 3.2(a, c). The band minima at the $\overline{\Gamma}$ point, the free electron-like band masses 1.1-1.2 and 0.8 m_e, and the binding energies -0.5 and -0.1 eV identify them as the IP1 and IP2 states [89]. Note that the recorded IP state intensities are strongly momentum dependent and are particularly weak near the $\overline{\Gamma}$ point where they are resonances.

In Figure 3.3(a), we plot the $\hbar\omega_l$ dependent E_f data of IP states detected in 3PP and 4PP spectra. In addition, we plot the 3PP Fermi level, which has a slope of 3.26 expected for an initial state in a 3PP process. By contrast, the IP1 and IP2 states appear with slopes of 1.14 and 0.97, as expected for the penultimate states in the excitation processes. The binding energies of IP1 and IP2 states relative to the vacuum level are comparatively small, which suggests a large quantum defect for the (110) surface that could result from their interaction with the bulk [7].

As explained above, the resonance character of the IP states due to their interaction with bulk *sp*-band limits their participation in the 2PP excitation at the $\overline{\Gamma}$ point of Ag(110). Moreover, in 4PP measurements at the $\overline{\Gamma}$ point [Figure 3.6(b)], the IP states hardly emerge from the continuous background, but their participation is confirmed by their dispersions. Therefore, in

Figure 3.6(a), the relatively strong IP state contrast at the $\overline{\Gamma}$ point in 3PP measurements is surprising.

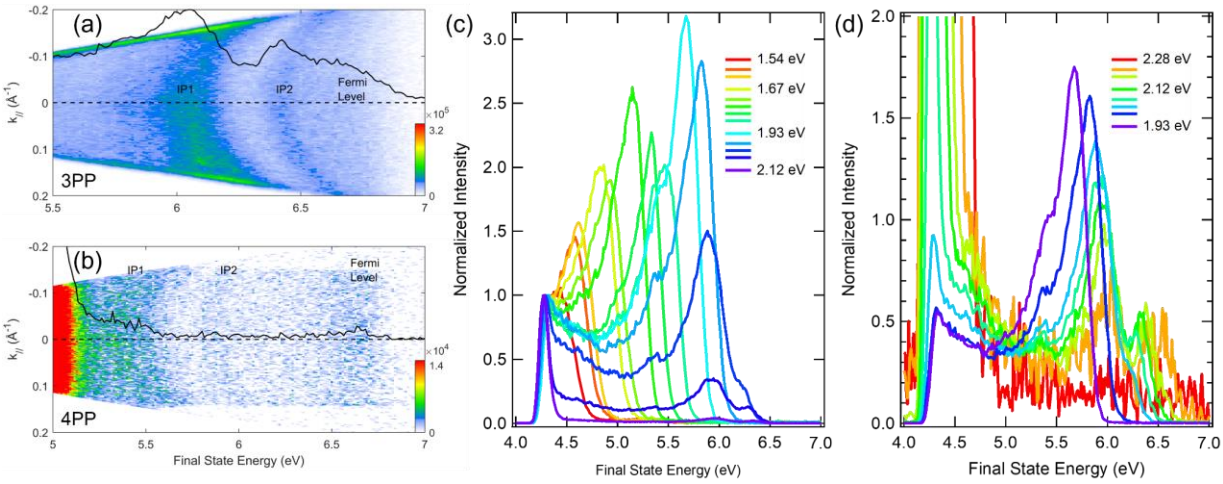

Figure 3.6 IP states excitation of Ag(110) at $\overline{\Gamma}$ point when sample $\overline{\Gamma X}$ direction is in the optical plane. The $E_f\left(k_{[1\bar{1}0]}\right)$ spectra are collected for (a) 2.28eV and (b) 1.67eV photon energy, and the IP states are detected in 3PP and 4PP, respectively. The black solid lines represent line profiles taken at the $\overline{\Gamma}$ point. IP1 and IP2 states and E_F signals are visible. (c, d) Photon energy dependent energy line profiles taken at the $\overline{\Gamma}$ point. Note that in (c) the intensities are normalized at the work function edge, which suppresses the E_F edge amplitude for the highest $\hbar\omega_l$ data because the work function edge signal is enhanced by onset of the signal from 2PP. In (d), the intensities at selective $\hbar\omega_l$ are normalized by the photoemission yield in the E_f range of 4.6-7 eV to avoid the large work function signal onset by 2PP as shown in (c). The spectra are taken with the sample aligned in the $\overline{\Gamma X}$ direction to eliminate the contributions from other surface states; otherwise, they have the same appearance.

Additional photon energy dependent data at the $\overline{\Gamma}$ point in Figure 3.6(c, d) show that below ~2 eV photon energy, the 3PP Fermi level signal is abnormally elevated, forming a peak-like structure instead of an expected shoulder representing the occupied Fermi-Dirac DOS that is

commonly observed in photoemission spectra of metals [90]. Above 2 eV excitation, this elevated signal evolves into a separate shoulder-like Fermi level and a peak which we attribute to IP1 state. This structure may be interpreted as an enhanced Fermi level excitation promoting 3PP by two-photon excitation via the IP state. Note also that the $\hbar\omega_l$=1.9 eV excitation is special for silver, because it is not only one-half of the bulk plasmon frequency, and as such could enhance nonlinear processes, but it also corresponds to the energy where the transient exciton feature appears in two-photon resonant transition from SS to IP1 state on Ag(111) [19, 28, 91]. We note that there is no surface or bulk band structure in the single particle Ag(110) spectra that could explain the intensification of the Fermi edge. The reason for the enhancement of the E_F edge in 3PP is robust and requires further scrutiny. Nevertheless, we speculate that these circumstances enhance the visibility of the IP states in 3PP over 2PP and 4PP.

Apart from the nonlinear order intensity differences, the IP state signal intensifies as $k_{[001]}$ moves from a resonance at the $\overline{\Gamma}$ point to a surface state within the projected band gap in the $\overline{\Gamma Y}$ direction; this is evident in 3PP and 4PP spectra in Figure 3.2(a) where the IP1 state signal is enhanced between $k_{[001]}$~0.2 and ~0.4 Å^{-1}. Besides the role of the band gap, this intensity enhancement can also be attributed to resonant transitions from the S1/S2 surface states to IP states. For instance, the IP1 state appears with high intensity at the crossing with the 'S2+2$\hbar\omega_l$' signal where it participates in a one-photon resonant transition from the S2 band, as already discussed. Moreover, at larger $k_{[001]}$, the 2-photon resonant IP1←S1$^{(unocc)}$ transition can also enhance the signal. The IP2 has similar resonances but with less intensity, probably because of a smaller wave function overlap.

3.4 Bulk Band Transitions of Ag(110)

After accounting for the known surface states, the remaining photoemission spectral features in the 2PP momentum microscopy data in Figure 3.1 must involve transitions from the occupied to the unoccupied *sp*-bands. Such transitions have been extensively studied for the (111) oriented Ag surface [59, 62, 63, 92, 93], where below the bulk plasmon frequency they are promoted by the dynamical multipole plasmon screening response of silver; they, however, have not been investigated for the (110) crystal orientation [32, 36, 94].

To define where the bulk band transitions may occur, we use the calculated $k_{\perp}$ bulk band structures by plotting E-E_F vs. $k_{||}$ dispersions at equidistant $k_{\perp}$-intervals along the bulk ΓK direction. These calculations allow consideration of how the bulk band structure of Ag(110) is involved in photoexcitations. The relevant bulk band structure profiles at three different $k_{\perp}$= 0.82, 0.93, and 0.77 Å^{-1} regions are plotted separately in Figure 3.7(a, b, c), where, in the following, the B3, B1, and B2 excitations in 2PP are assigned to the respective B←A, D←A, and C←A transitions. These transitions can also be excited with *s*-polarized light (not shown).

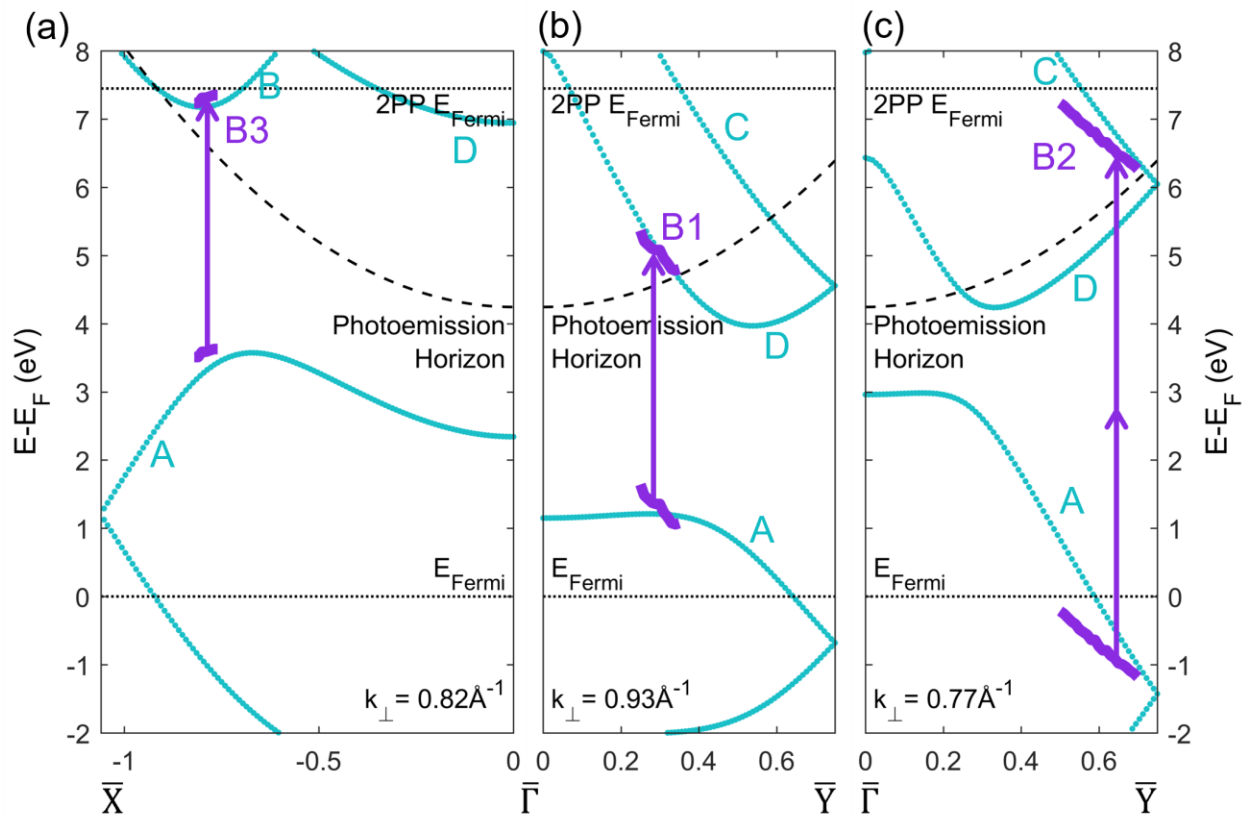

Figure 3.7 Bulk band transition assignments from 2PP spectroscopy plotted relative to the calculated Ag(110) $k_{||}$-resolved bulk band structure at different $k_{\perp}$. The panels (a), (b), and (c) show $\overline{\Gamma X}$ and $\overline{\Gamma Y}$ cuts for selected $k_{\perp}$-momenta along the bulk ΓK direction. The calculated *sp*-bulk bands are labelled with upper-case letters (A, B, C, and D). The spectroscopic features B1, B2, and B3 identified in Figure 3.1 are plotted as solid purple lines.

The B1 band [Figure 3.7(b)], whose dispersion is shown for the $\overline{\Gamma Y}$ direction, involves a 1-photon transition from band A to band D and appears over the photon energy ranging from $\hbar\omega_l$ =2.83 eV to above 4.15 eV (not shown). Varying the excitation energy defines different $k_{\perp}$ and $k_{||}$ in B1 that satisfy the energy and parallel momentum conservation in resonant optical transitions. Due to the different $k_{||}$ dispersions of bands A and D, the resonant transitions between them are excited over a limited energy range (~1 eV).

The B3 band [Figure 3.7(a)] in $\overline{\Gamma X}$ direction involves a similar excitation mechanism, but disappears for $\hbar\omega_l$<3.5 eV excitation because of a larger gap between bands A and B, which shows good agreement between the experiment and theory.

The B2 band [Figure 3.7(c)], involving a 2-photon resonant transition between bands A and C near the $\overline{Y}$ point, corresponds to the well-known two-photon transition between the lower and upper *sp*-bands of Ag(111) that is centered at the $\overline{\Gamma}$ point, which will also be discussed in Chapter 4 [63, 93]; on the (110) surface, however, it is observed normal to the (111) planes that form it. Although the *sp*-band signal appears for excitations ranging between 2.6 eV and 3.9 eV for Ag(111) [36, 93], the B2 band on Ag(110) disappears below $\hbar\omega_l$=3 eV excitation at large $k_{||}$ because it is cut off by the photoemission horizon. A common feature of both surfaces is that the bulk 2PP signals disappear for $\hbar\omega_l$>3.9 eV excitation, although the transition is allowed from a pure band structure perspective, as will be shown in Figure 4.3(a). We attribute the vanishing of B2 signal to the multipole plasmon response of Ag, which becomes ineffective above the bulk plasmon frequency of ~3.9 eV, which will be discussed in detail in Chapter 4.2.1 [37, 93, 95-97]. Moreover, this C←A bulk band transition can also be excited by 3- and 4-photon resonance with a weaker intensity because the resonant transition involves the unoccupied part of band A, which must be populated first by absorbing an additional photon (Figure 3.8).

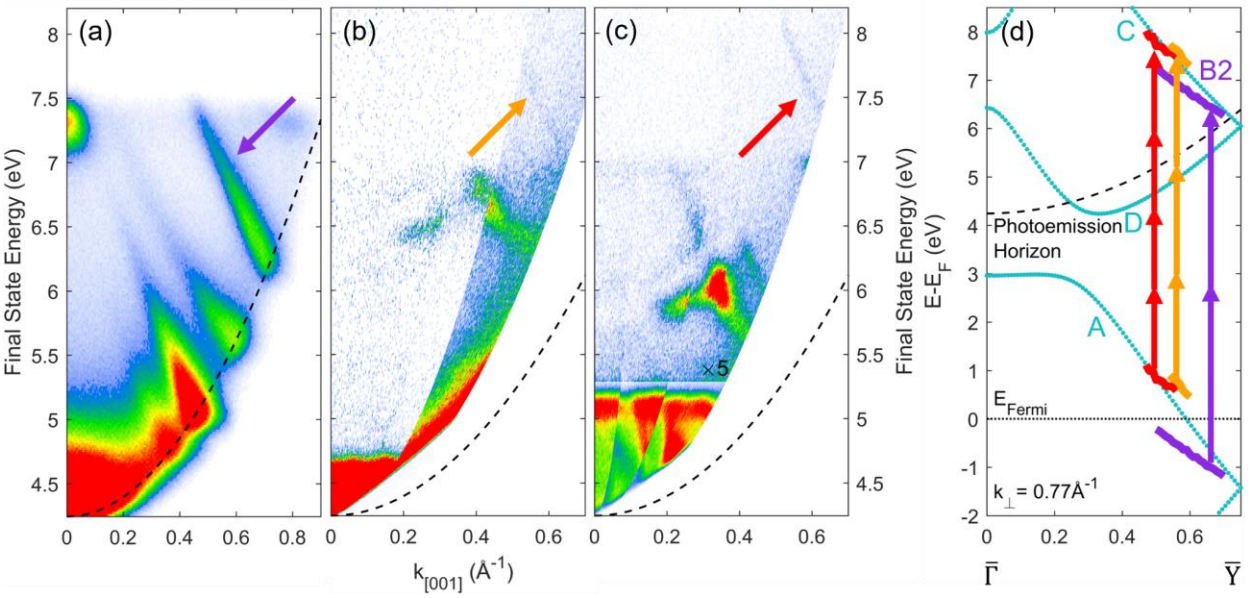

Figure 3.8 Bulk excitations between bands A&C measured as resonances in (a) 2PP, (b) 3PP and (c) 4PP with $\hbar\omega_l$=3.72, 2.28, and 1.72 eV, respectively. Corresponding peak dispersions are plotted in (d) $k_{||}$-resolved bulk band structure at $k_\perp$ = 0.77 Å^{-1} in purple, orange, and red color. 3PP and 4PP peaks appear with a weaker intensity because the resonances initiate from the unoccupied part of band A which needs to be populated by absorption of an additional photon such that these processes are actually 4PP and 5PP.

We note that transitions between the initial and final bulk bands can occur between states of different $k_\perp$, which is not conserved in photoemission. Our analysis, which considers fixed $k_\perp$ for resonant transitions, however, already has a good match to experiments. The matching could be improved by considering the 3D bulk band structure, but because the calculated electronic band structures are not exact, this is unlikely to generate more accurate assignments.

Finally, there is a very weak feature B4 in Figure 3.1(a, c) which we assign to a one-photon photoemission from the upper *sp*-band gap edge of Ag(110) around the $\overline{\text{Y}}$ point, which must be populated from the lower *sp*-band. The photon energy is insufficient for one photon excitation, so such transition must involve either a two-photon excitation, or promotion of hot electrons from

above E_F. The detection of electrons in the upper *sp*-band has been previously proposed [98], and it also occurs weakly in 2PP spectra of Ag(111) at the $\overline{\Gamma}$ point. There, an additional dispersive feature clearly separates from that of the IP1 state at parallel momentum $k_{\|}$~0.15 Å^{-1} above the IP1 state, which can be seen in Figure 4.2(d); this feature, however, is not the focus of this work.

Although we attribute these features to the bulk bands, we note that their appearance is promoted by a strong surface character arising from several factors. Because light cannot penetrate deeply, and more pertinently, because the multipole plasmon response screens its penetration by generating intense surface local fields for excitation below the bulk plasmon frequency [97, 99, 100], the bulk bands that have large transition moments must also have a large near-surface density [92].

3.5 Comparison between Momentum Microscopy and ARPES

In conclusion, I have described and assigned the 3D non-linear photoemission momentum microscopy energy-$k_{||}$ images of anisotropic electronic bands of the Ag(110) surface. Specifically, I have identified three surface states (S1, S2, and S3), the first and the second image potential states (IP1 and IP2), as well as four bulk interband transitions (B1, B2, B3, and B4). All the band dispersions are plotted in Figure 3.9 as thick solid lines at energies where they appear in 2PP spectra as the initial, intermediate, or final states, giving a comprehensive understanding of the possible electronic transitions taking place at the pristine Ag(110) surface. Before finishing this chapter, I want to discuss some points regarding (i) implications of using higher-order photoemission spectroscopy for mapping complex band structures and (ii) strength of momentum microscopy and ARPES techniques in studying mPP.

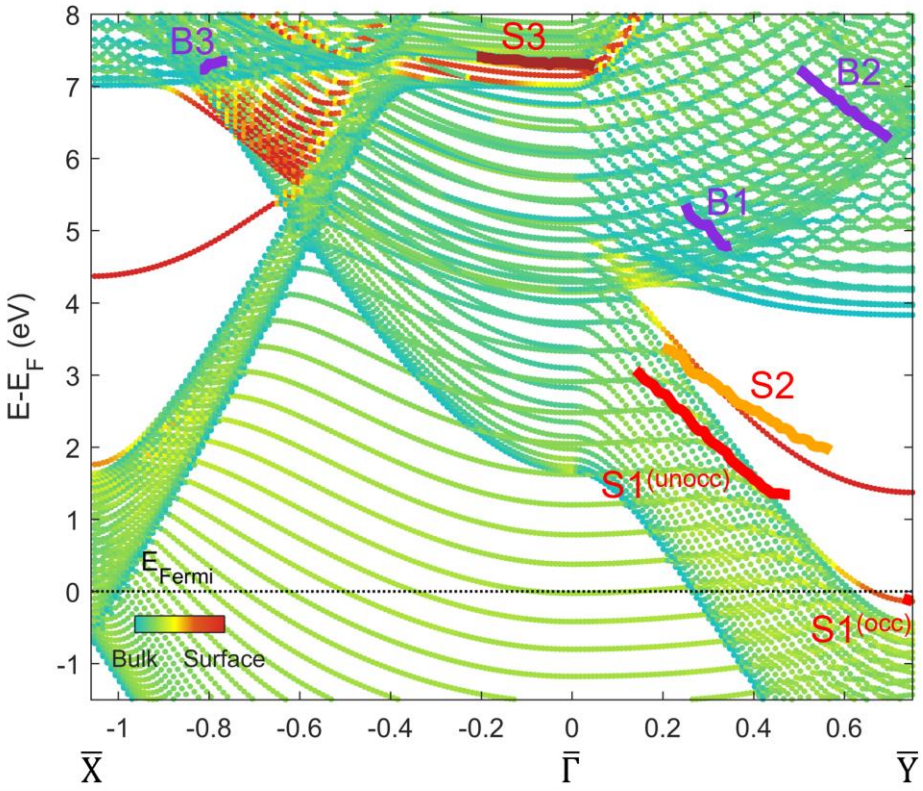

Figure 3.9 Summary of the experimental results and comparison to the calculated surface and bulk band structures of Ag(110) in the $\overline{\Gamma X}$ [1$\bar{1}$0] and $\overline{\Gamma Y}$ [001] directions. The color scale shows their bulk/surface character determined by the atomic-projection method which uses atomic orbitals to project the bands to determine their bulk or surface characters. State dispersions (S1-S3, B1-B3) are extracted from momentum microscope data in Figure 3.1.

First, I have employed photon energies ranging from infrared to ultraviolet to excite electrons above the work function, and in some cases even above threshold, in the non-linear orders of *m*=2, 3, and 4. Depending on the photon energy, my measurements are distinctively sensitive to different dipole transitions in the photoexcitation process. This is most evident in my ability to detect the IP states prominently in 3PP, whereas they are dark in 2PP even though the bulk *sp*-bands must act as initial states for their population in either case. I surmise that this happens

because of distinct resonances that potentially enhance the photoexcitation process, but such interpretation requires further scrutiny. Thus, to obtain a more comprehensive band mapping of a complex electronic structure I propose that it can indeed be helpful to investigate the electronic bands of a solid in multiple nonlinear orders in the perturbative regime.

As for the second point, I note that my results showcase the strength of two-photon momentum microscopy experiments. This has already been established in several selected examples [101-103], particularly for investigation of exciton structure and dynamics in 2D materials [104, 105]. My data however, notably make it evident that this approach is especially well suited for anisotropic surfaces. The full anisotropic electronic band structure and all the (non-)linear optical transitions that occur within it can be accessed simultaneously without concern on how light's incidence affects its interaction with a solid. In the case of Ag(110) surface, this is especially advantageous, because it is not necessary to consider how the measurements depend on the relative electric field polarization through the field polarization and sample orientation dependence of dipole matrix elements. Such effects play a significant role in photoemission involving the S2←S1$^{(occ)}$ resonance on Ag(110) [28, 55, 79]. One can also envision that because momentum microscope measurements provide information on the real space distribution of the electronic wave functions [12, 15, 106] and their electron dynamics [16], one may be able to achieve similar real space resolved imaging of electronic bands and their dynamics.

Compared with momentum microscope which can measure photoelectron information in 3D, ARPES can only measure signals in 2D but has a more restricted energy-momentum window which is especially suited for higher order photoemission experiments, e.g., ATP [88]. I can selectively define the energy range of interest, which is very important in measuring higher order signals because mPP signal intensity is usually ~1000 times stronger than that of (m+1)PP. To

measure the (m+1)PP signal, I need to block the lower order signal to avoid saturating the detector. Moreover, a more restricted energy-momentum window can also enhance the spectral resolution.

4.0 Plasmonic Photoemission Response of Low Index Silver Surfaces

Photons can excite single-particle and collective excitations in metals. Previous chapter introduces how I analyze the photoemission spectra to trace the origin of different mPP features where most of them can be classified as Einsteinian photoemission in single particle picture. By studying the spectra of three low index silver surfaces [Ag(111), Ag(100), Ag(110)], I found signatures which involve excitation of the bulk plasmon mode of silver, which decays in an unconventional way to excite non-Einsteinian photoemission. Thus, in this chapter, I will introduce this novel non-Einsteinian photoemission excitation channel where photoelectrons are excited by the secondary plasmon field, instead of the external photon field. The content in this chapter is based on publications in Physical Review Letters and ACS Photonics [36, 93].

4.1 Introduction to Plasmons

The collective plasmonic excitations are of broad interest in physics, chemistry, optics, and nanotechnology because they enhance coupling of the electromagnetic energy and can drive nonlinear processes in electronic materials [10, 17, 107-120]. For example, the collective response of Ag can be defined by morphology-derived surface plasmon polariton and Mie plasmon modes. Such modes are intensely studied for possible applications ranging from quantum computing to energy and medicine [10, 108, 119]. However, the intrinsic bulk plasmon responses of crystalline Ag has hardly been explored by electronic, photoemission, or nonlinear-optical spectroscopy, which motivates this work [91]. Moreover, the collective plasmon-mediated excitations have large cross sections for

harvesting optical energy and transferring it to hot electron excitations, which are considered to be key intermediates of energy transduction in optically induced chemical and physical processes at metal surfaces [17, 121-136]. But how energy flows from the optical, to the collective plasmon, and eventually to the hot electron excitations is unclear. Instead of the common belief in the plasmonics community that plasmon decay produces a hot electron and hole distribution defined by their joint DOSs spanning energies between $-\hbar\omega_p$ and $+\hbar\omega_p$ with respect to the Fermi level E_F (ω_p: bulk plasmon frequency), I found that the bulk plasmon decay preferentially excites photoelectrons from E_F, leading to a high plasmon-to-hot electron energy transduction efficiency.

The complex dielectric response function, $\varepsilon(\omega_l)$, encodes the electronic response to optical excitation among transmission, reflection, or absorption [25, 137-140]. An example of silver dielectric function is shown in Figure 4.1. The classical Drude dielectric function, $\varepsilon(\omega_l) = \varepsilon_0\left[1 - \left(\frac{\omega_p^2}{\omega_l(\omega_l + i/\tau)}\right)\right]$, is defined by the longitudinal plasmon frequency $\omega_p = \sqrt{\frac{4\pi ne^2}{\varepsilon_0 m_e}}$ (n: electron density), and its dephasing time τ [51]. The epsilon near zero (ENZ; $\mathrm{Re}[\varepsilon(\omega_l)]=0$) condition defines the bulk plasmon frequency, ω_p, and designates a frequency region where the reflectivity drops to a minimum and the dielectric response at surfaces is nonlocal [2, 141-143], and dominantly nonlinear [91, 144-146]. Below ENZ ($\mathrm{Re}[\varepsilon(\omega_l)]<0$), free electron plasmas responds collectively intensifying the surface field opposing (screening) the optical one's penetration by reflection, but above, the response becomes retarded and nonlocal allowing the optical penetration in form of a longitudinal charge density wave [49-51, 99]. This collective oscillation of electron plasmas at the frequency of ω_p is the bulk plasmon mode.

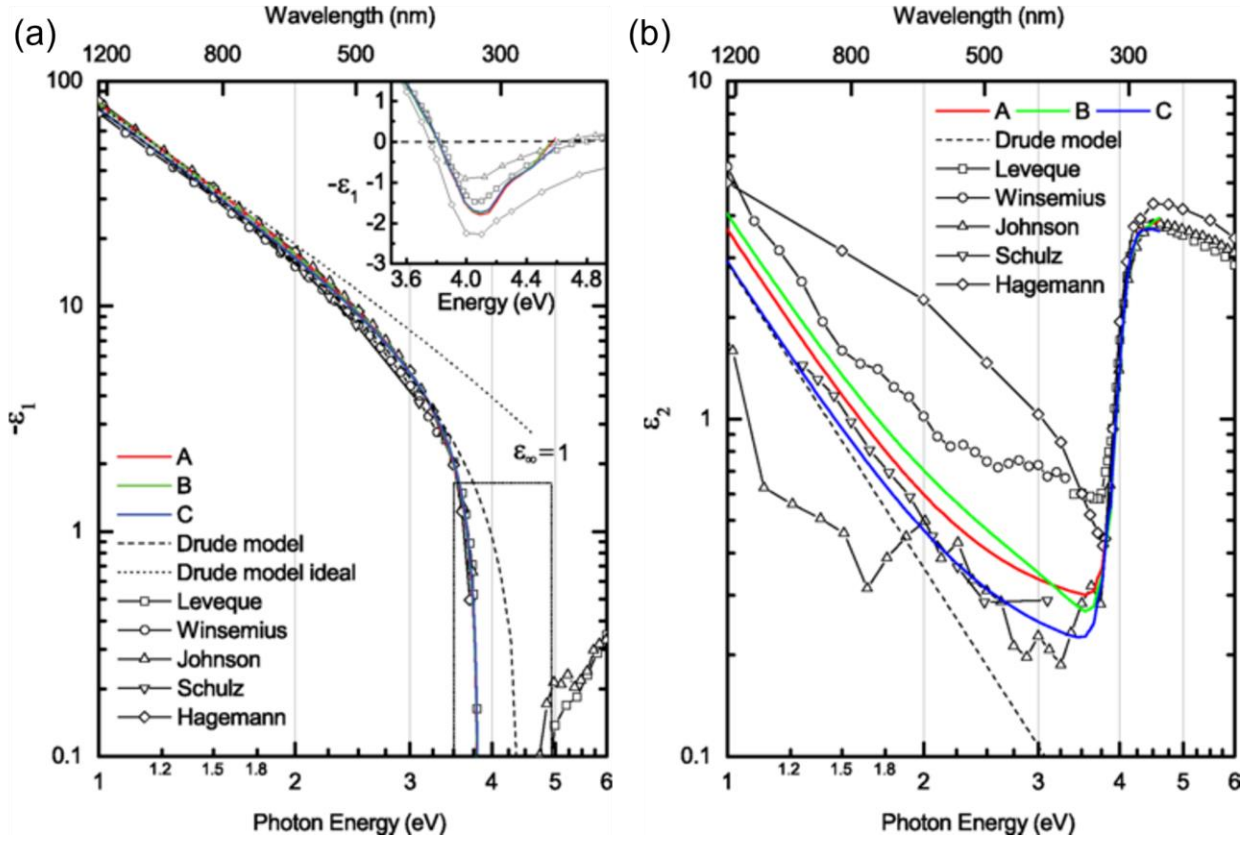

Figure 4.1 (a) The negative real part and (b) the imaginary part of dielectric function of Ag. A (red), B (green), and C (blue) are data measured from three different samples. Other data is from different literature for comparison. Inset in (a): the negative real part of dielectric function of Ag near 3.8 eV shown in linear scale, where $\varepsilon(\omega_l)$ transitions from positive to negative values due to the interband transition. Figures are reused from Ref. 147 under permission. URL, http://dx.doi.org/10.1103/PhysRevB.91.235137.

In alkali metals and free electron metals like Al and Be, the modulation of spectral intensities when $\hbar\omega_l$ is scanned through the ENZ region reveals the plasmonic participation in 1PP [96, 148-155]. For pure alkali atoms films, it has been established that their bulk plasmon decay preferentially excites photoelectrons from the E_F [148-150, 154]. Such preferential excitation of electrons from E_F by decay of plasmons was explained by Hopfield as a consequence of dynamical screening [156]. However, for Ag, a widely investigated plasmonic material, its work function of

Φ~4.5 eV exceeds its $\hbar\omega_p$=3.7-3.9 eV, thus blocking observation of such a response. Berglund and Spicer were first to show that when Φ of Ag films is reduced by Ba chemisorption to below ENZ, linear photoemission spectrum is peaked at E_F indicating that the energy of a full plasmon quantum is transferred to single electrons preferentially at the top of the Fermi surface [153]. Later, Horn and coworkers, investigated photoemission spectra of single crystalline Ag films with Φ reduced by alkali atom chemisorption [157, 158], to establish definitively that the decay of the longitudinal bulk plasmon mode of silver preferentially excites single electrons at E_F. The significance and implications from these studies of evidence for plasmonic photoemission in metals to the transduction of optical energy into hot electron excitations, however, has been overlooked.

Here, instead of depositing adsorbates to lower the Φ, we use the nonlinear 2PP spectroscopy to circumvent the work function impediment. Scanning of the excitation light through the ENZ region enables the nonlinearly excited electrons to overcome the work function and communicate information on their plasmonic origin. We analyze the 2PP spectra of three low-index silver single crystal surfaces [Ag(111), Ag(100), and Ag(110)] and discuss the plasmonic photoemission channels shown below [36, 37, 93].

4.2 Plasmonic Photoemission Pathways on Ag(111) and Ag(100) Surfaces

4.2.1 Multipole Plasmon Enhancement in Ag(111) Spectra

Figure 4.2 and Figure 4.3 show photoelectron energy- and $k_{||}$-momentum-resolved 2PP spectra for different $\hbar\omega_l$ and line profiles for normal emission ($k_{||}$ = 0 Å^{-1}) extracted from them, respectively. Figure 4.4 plots the final state energy E_f and intensities vs. $\hbar\omega_l$ for the detected

spectral features. The $E_f(k_{||})$ resolved 2PP spectra below [Figure 4.2(a, b)] and above [Figure 4.2(c, d)] ENZ are dramatically different. For $\hbar\omega_l<\hbar\omega_p$, as discussed in Chapter 1, the main feature in the spectra is the two-photon resonant $U_{sp}\leftarrow L_{sp}$ bulk inter-*sp*-band transition which appears with far higher intensity than that of the nonresonant two-photon excitation of the SS state. Increasing $\hbar\omega_l$ to above $\hbar\omega_p$, however, causes the bulk *sp*-transition to disappear, even though it dominates the linear 1PP spectra [92]. The SS and the IP1 states remain and pass through resonance at ~3.9 eV, and above $\hbar\omega_p$, the surface states dominate the 2PP spectra [Figure 4.2(c), Figure 4.3(b)]. The E_f vs. $\hbar\omega_l$ values of the SS and IP1 peaks vary with a slope of 2.1 and 1.1, respectively [Figure 4.4 (a)], as expected for the initial and intermediate states in 2PP spectra [39]. The slope of the bulk $U_{sp}\leftarrow L_{sp}$ transition on Ag(111) is intermediate between 1 and 2, because as $\hbar\omega_l$ is varied, its E_f follows the two-photon resonance condition at different $k_\perp$ [61, 93]. The pronounced intensity variation of the bulk *sp*-transition and appearance of a new spectral feature at $E_f\approx$ 7.75 eV, however, herald plasmonic responses of the Ag(111) surface.

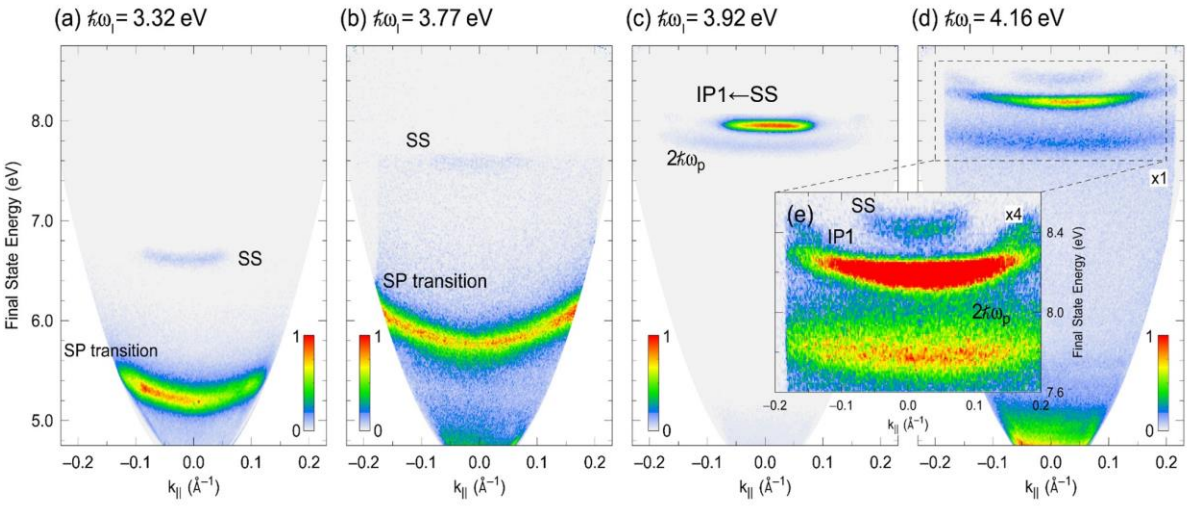

Figure 4.2 Energy and $k_{||}$-momentum resolved 2PP spectra of Ag(111) for increasing excitation energies $\hbar\omega_l$. (a, b) For $\hbar\omega_l<\hbar\omega_p$, the *sp*-transition intensity dominates that of the SS state. (c, d) For $\hbar\omega_l\geq\hbar\omega_p$, the SS and

the IP1 states dominate the spectra, but the *sp*-transition vanishes. An additional feature appears at $E_f = 2\hbar\omega_p \approx 7.75$ eV. (e) Enlarged $E_f(k_{||})$-spectra from the dashed box in (d) showing the $2\hbar\omega_p$ feature, as well as the IP1 and SS states (the color-scale is expanded four times).

We first consider the nonlinear coupling of the bulk *sp*-bands of Ag, which can be excited by a two-photon transition in the entire investigated $\hbar\omega_l$ range. The *sp*-transition is the dominant spectroscopic feature in 2PP spectra for $\hbar\omega_l < \hbar\omega_p$ with a maximum for $\hbar\omega_l \approx 3.4\text{-}3.5$ eV, it is drastically suppressed at $\hbar\omega_p$ and vanishes above it [Figure 4.4(b)]. This drastic intensity variation cannot be attributed to transition moments, because in linear 1PP spectra for $\hbar\omega_l = 6\text{-}10$ eV, the *sp*-transition varies by only ~50% with respect to the SS photoemission [92]. Instead, we attribute its dramatic intensity variation to screening of the surface fields, to which 2PP, being proportional to the fourth power of electric field strength, is exceptionally sensitive. The near surface field in a metal below $\hbar\omega_p$ is defined by the external field and the multipole plasmon (MP) nonlocal screening response [151, 155, 159, 160]. The MP resonance of Ag(111) has been reported at $\hbar\omega_{MP} = 3.74$ eV in electron energy loss spectroscopy (EELS) by Rocca and coworkers [161], but it is expected to enhance the near-surface fields over a broad frequency range [99, 160, 162]. Our finding of the strong *sp*-transition intensity modulation is consistent with the near-surface field enhancement by the MP screening below $\hbar\omega_p$.

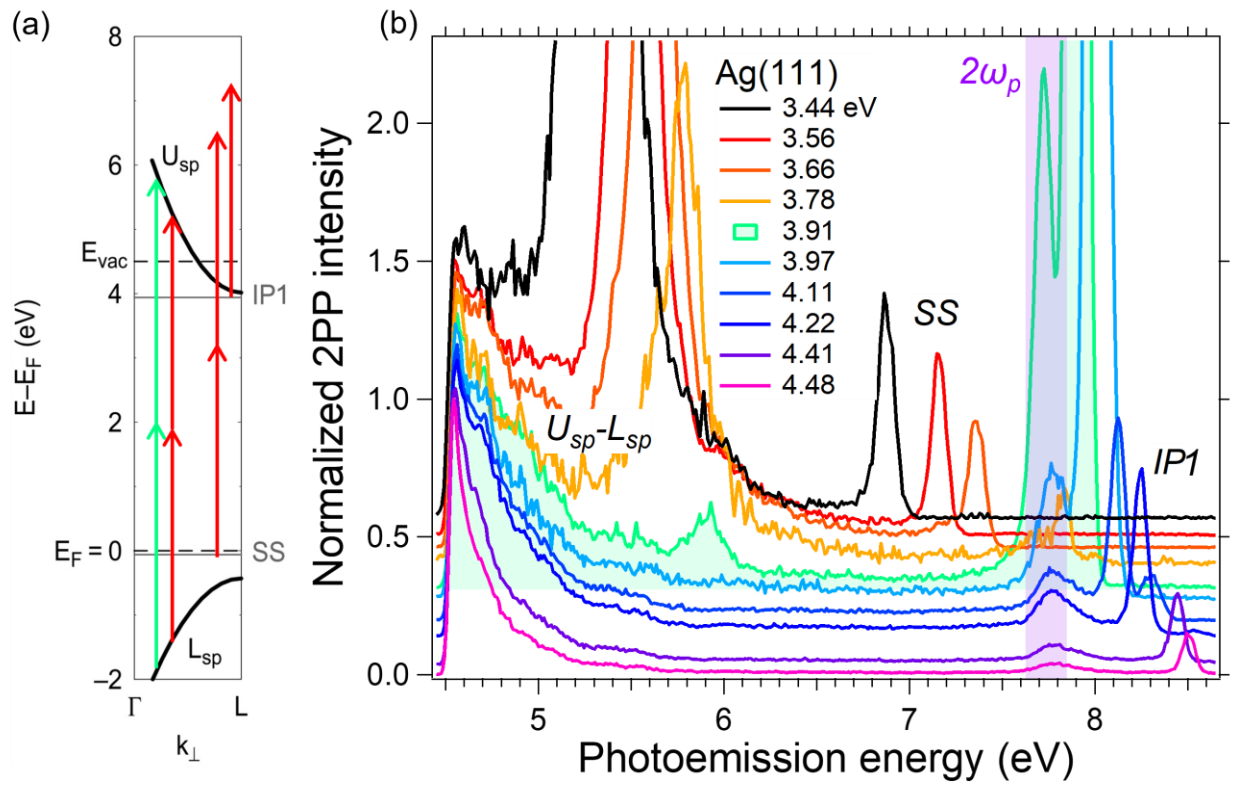

Figure 4.3 2PP spectra and photoexcitation pathways in the 3.4 to 4.5 eV energy range for Ag(111) surface. (a) The single-particle band structure of Ag along the Γ-L ($k_\perp$) direction; the indicated optical transitions connect the free-electron like L_{sp} and U_{sp}, *sp*-bands as well as surface states (SS, IP1). (b) 2PP spectra obtained by tuning $\hbar\omega_l$ through the ENZ range. The spectral $k_{||} = 0$ Å^{-1} profiles from data like in Figure 4.2 are normalized at the work function edge and shifted vertically according their $\hbar\omega_l$ (indicated in the legends). The green shading in (b) highlight the ENZ excitation, where the $2\hbar\omega_p$ peak intensity is maximum. The purple shading emphasizes the $2\hbar\omega_p$ peak.

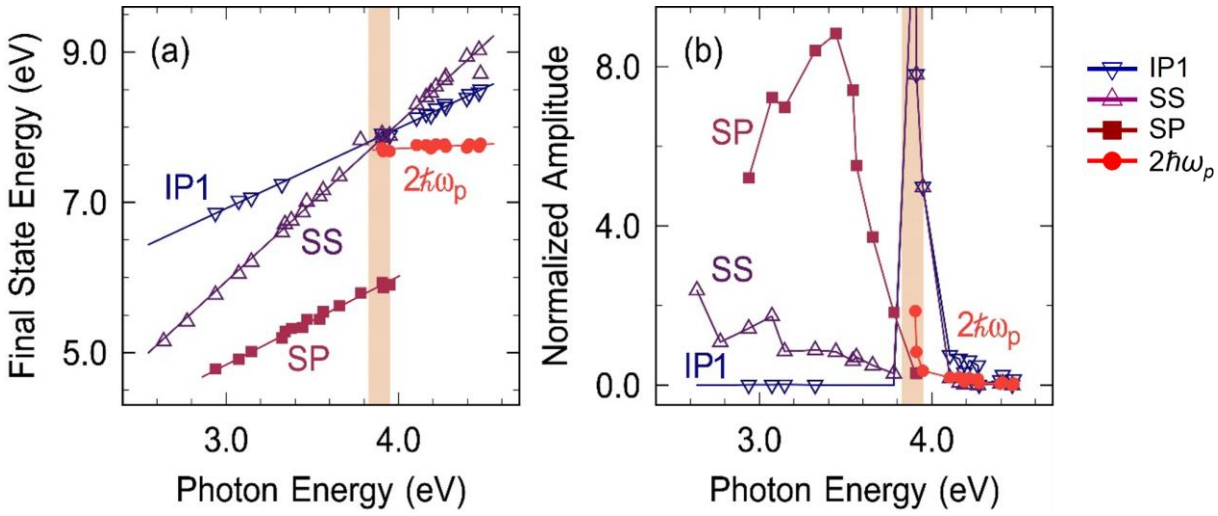

Figure 4.4 Quantitative evaluation of 2PP spectra of Ag(111) from Figure 4.3 for 2.6< $\hbar\omega_l$ <4.5 eV ($k_{||}$=0 Å^{-1}); the brown shading highlights the ENZ region. (a) E_f vs. $\hbar\omega_l$ and (b) peak intensities vs. $\hbar\omega_l$ for the major spectroscopic features: the $2\hbar\omega_p$ feature is only observed at and above $\hbar\omega_l$≈3.9 eV and its E_f vs. $\hbar\omega_l$ shifts with a slope of 0.08.

The MP field enhancement can also be confirmed by comparing 2PP spectra of Cu(111) and Ag(111) surfaces; both metals have very similar band structures, electron escape depths, etc., except for their plasmonic responses, which is at a higher frequency and less well defined for Cu [163]. Because Cu(111) experiences less pronounced MP response than Ag(111), its *sp*-transition is barely detected in Figure 4.5 and Ref. 164.

The MP response is known to enhance 1PP yields from surface states of free electron metals over a broad energy range ($\Delta\hbar\omega_l$≈5 eV) [152, 155, 165]. Whether it also affects the 2PP from SS of Ag(111) is not clear, because our measurements cover a limited range ($\Delta\hbar\omega_l$<2 eV), where its intensity is affected by resonance with the IP1 state, in near-coincidence with ENZ.

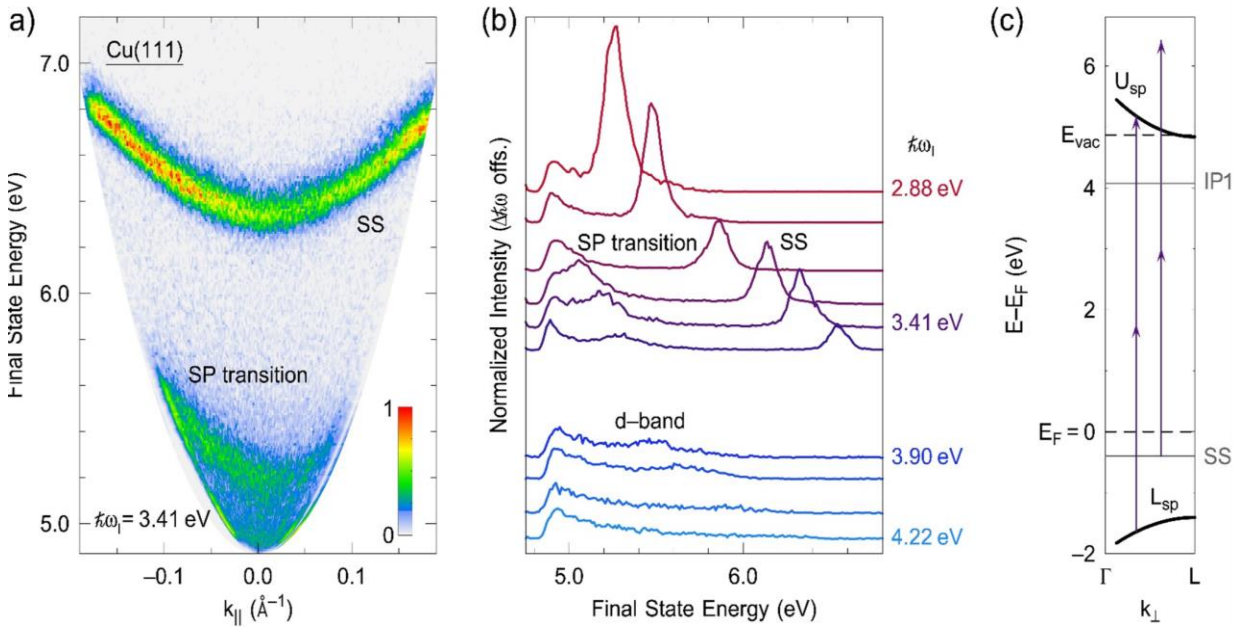

Figure 4.5 2PP spectra of Cu(111). (a) $E_f(k_{||})$-distribution of Cu(111) as excited with 3.41 eV photons, the spectrum is composed of the coherent non-resonant 2-photon SS state excitation and the resonant *sp*-transition [the excitation diagram as a function of $k_\perp$ is given in (c)]. (b) Line profiles taken at $k_{||}$ = 0 Å^{-1} in a photon energy range between 2.88 and 4.22 eV. The spectra are normalized at the work function edge and shifted on the vertical axis by $\Delta\hbar\omega_l$.

4.2.2 Bulk Plasmon Excitation in Ag(111) Spectra

The characteristics of the spectral feature at $E_f \approx 7.75$ eV$\approx 2\hbar\omega_p$ are that it appears only for $\hbar\omega_l \geq 3.9$ eV with gradually decreasing intensity [Figure 4.3(b), Figure 4.4], its line shape is skewed [Figure 4.2(c, d)], and it disperses over the accessible $k_{||}$-range. Most significantly, the E_f vs. $\hbar\omega_l$ of the $2\hbar\omega_p$ feature increases with a slope of 0.08. Giesen *et al*. reported the same feature in one-color 2PP spectra of Ag(111) excited with a tunable nanosecond laser [39]. A 2PP peak that is nearly independent of $\hbar\omega_l$ is exceptional; it could signify a two-photon excitation to a final state at a fixed E_f, or a process where excitation at $\hbar\omega_l$ creates a field at $\hbar\omega_p$. The only final state at $E_f \approx 7.75$ eV is

the three-dimensional U_{sp}, band, but there is no reason for photoemission from U_{sp} to localize at this E_f [cf. band-diagram in Figure 4.3(a) and Ref. 58, 92, 157]. Instead, Giesen *et al*. attributed the $E_f \approx$ 7.75 eV peak to an Auger process where a pair of electrons populating the IP1 state scatter deactivating one and causing the other to be photoemitted at approximately their combined energy. Because our laser pulse duration is comparable to the IP1 state lifetime [41], and six orders-of-magnitude shorter than that of Giesen *et al.*, the putative Auger process, which should depend quadratically on the IP1 state population, is inconsistent with it appearing in both experiments with comparable intensity relative to the IP1 state. Moreover, in Figure 4.6, we can also exclude the Auger process by depositing organic molecules onto Ag(111) surface, which quenches the SS and IP1 state signals differently from the $2\hbar\omega_p$ feature, indicating that they are unrelated resonances at the Ag(111) surface [166]. Instead, we attribute the $2\hbar\omega_p$-feature to decay of two bulk plasmon quanta, which can be excited for $\hbar\omega_l \cong \hbar\omega_p$ and must excite single photoelectrons from E_F to $E_f \approx 2\hbar\omega_p$. In EELS spectral of Ag(111) with >70 eV electrons, a $2\hbar\omega_p$ loss peak has also been reported at 7.6 eV [167, 168], approximately where we detect the $2\hbar\omega_p$ decay.

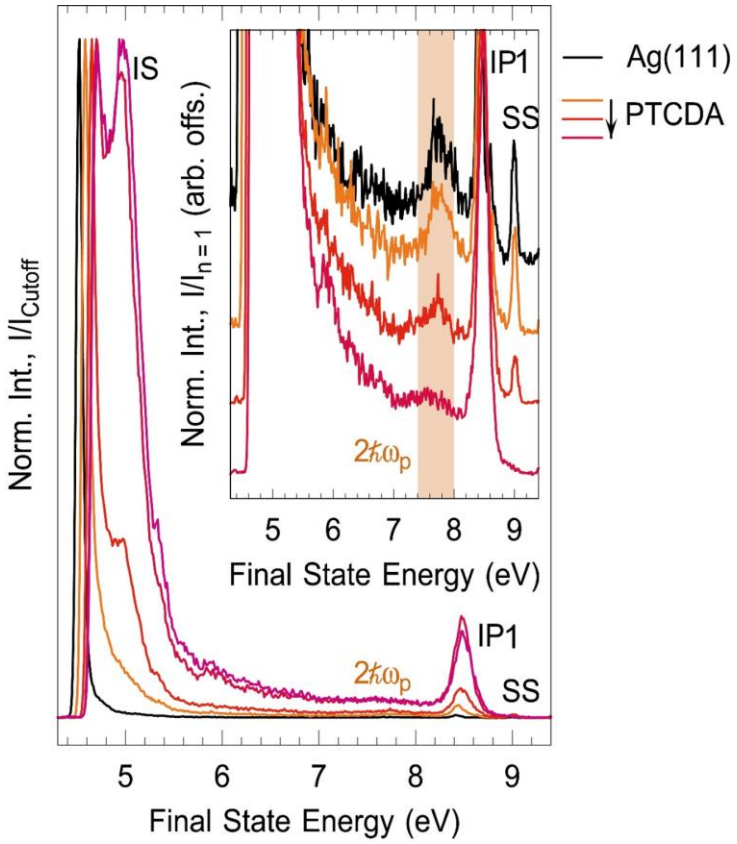

Figure 4.6 2PP spectra for different PTCDA molecule coverages on Ag(111) ($\hbar\omega_l$ = 4.58 eV, $k_{||}$ = 0 Å^{-1}, 300 K). The spectra are normalized at the work function edge. In the inset, the signal is normalized on the IP1 state intensity and offset by an arbitrary amount on the vertical axis. With increasing PTCDA coverage, the initially occupied SS state disappears and the unoccupied Shockley-type metal-organic interface state (IS) is formed. The SS state intensity drops significantly faster than the $2\hbar\omega_p$-feature. The IP1 and $2\hbar\omega_p$ intensities appear uncorrelated, contrary to expectation if the Auger decay of IP1 is the source of $2\hbar\omega_p$.

Why the $2\hbar\omega_p$-feature appears at twice the bulk plasmon frequency needs to be addressed. Screening of the transverse *p*-polarized optical field by the nonlocal dielectric response induces a surface charge density, including the longitudinal bulk plasmon, to be excited at the Ag surface. This response has been calculated to decrease above $\hbar\omega_p$ because the longitudinal plasmon cannot respond sufficiently fast as $\hbar\omega_l$ is scanned in energy [2, 143], as is observed in our experiment. The

bulk plasmon is a polarization field at ω_p that can act as a secondary excitation to excite additional *e-h* pairs. The decay of plasmons into single particle excitations is thought to excite electrons from E_F-$\hbar\omega_p$ up to E_F, to final states from E_F up to E_F+$\hbar\omega_p$, with only the density-of-states determining the hot electron energy distribution [169]. In the 2PP experiment, however, we measure the peak at $E_f = 2\times\hbar\omega_p$ where plasmon-excited electrons must have been preferentially excited from initial states near E_F. Such photoemission scenario is unconventional, in the sense that it does not follow theoretical predictions of plasmonically generated hot electron distributions [134], but has precedent in photoemission spectra of alkali atom covered thin Ag films as discussed in Chapter 4.1 [157]. We note that single-particle 2PP from E_F at $k_{\|}$ = 0 Å^{-1} is not possible as a direct photoexcitation, because the band gap of Ag(111) extends from E-E_F=-0.4 to 3.9 eV [26]. The SS state just below E_F is also unlikely as the initial state, because (i) its $k_{\|}$-dispersion and occupation range does not match the $2\hbar\omega_p$-feature [Figure 4.2(e)]; and (ii) it is quenched more rapidly by molecular adsorption (Figure 4.6). In a many-body process, however, electrons from E_F can be photoemitted at $k_{\|}$ = 0 Å^{-1}, if multiple particles scattering conserves momentum. The bulk plasmon response involves electron charge-density fluctuations at E_F, and thus it may induce photoemission of the same population. Moreover, the preferential excitation of electrons from E_F by decay of plasmons was explained by Hopfield for alkali atoms as a consequence of dynamical screening [156]. He further posited that the same process might occur in Ag, based on the photoemission spectra of Berglund and Spicer and their interpretation by Phillips [153, 170, 171].

To test our hypotheses, and confirm that in the linear response, ω_p decay excites electrons to $E_f \approx 1\hbar\omega_p$, as has been reported for Na/Ag(100) films [157], we lower the work function of Ag(111) by sub-monolayer chemisorption of Rb, which only modifies the surface electronic structure of Ag [172]. Indeed, 1PP spectra of Rb/Ag(111) with Hg-lamp excitation ($\hbar\omega_l \approx$ 4.86 eV; Figure 4.7)

reveal that besides the single particle features of Ag(111), a broad peak appears at $E_f \approx 3.7$ eV consistent with the bulk plasmon decay exciting electrons from E_F to $E_f \approx 1\hbar\omega_p$. Thus, the $2\hbar\omega_p$-feature of Ag surfaces [39, 173] is a robust nonlinear counterpart where two $\hbar\omega_p$ quanta excite single electrons from E_F, which is consistent with the previous 1PP spectra of Ag films [157]. A theoretical model that explains this bulk plasmon decay process has been proposed by Gumhalter *et al.* [37].

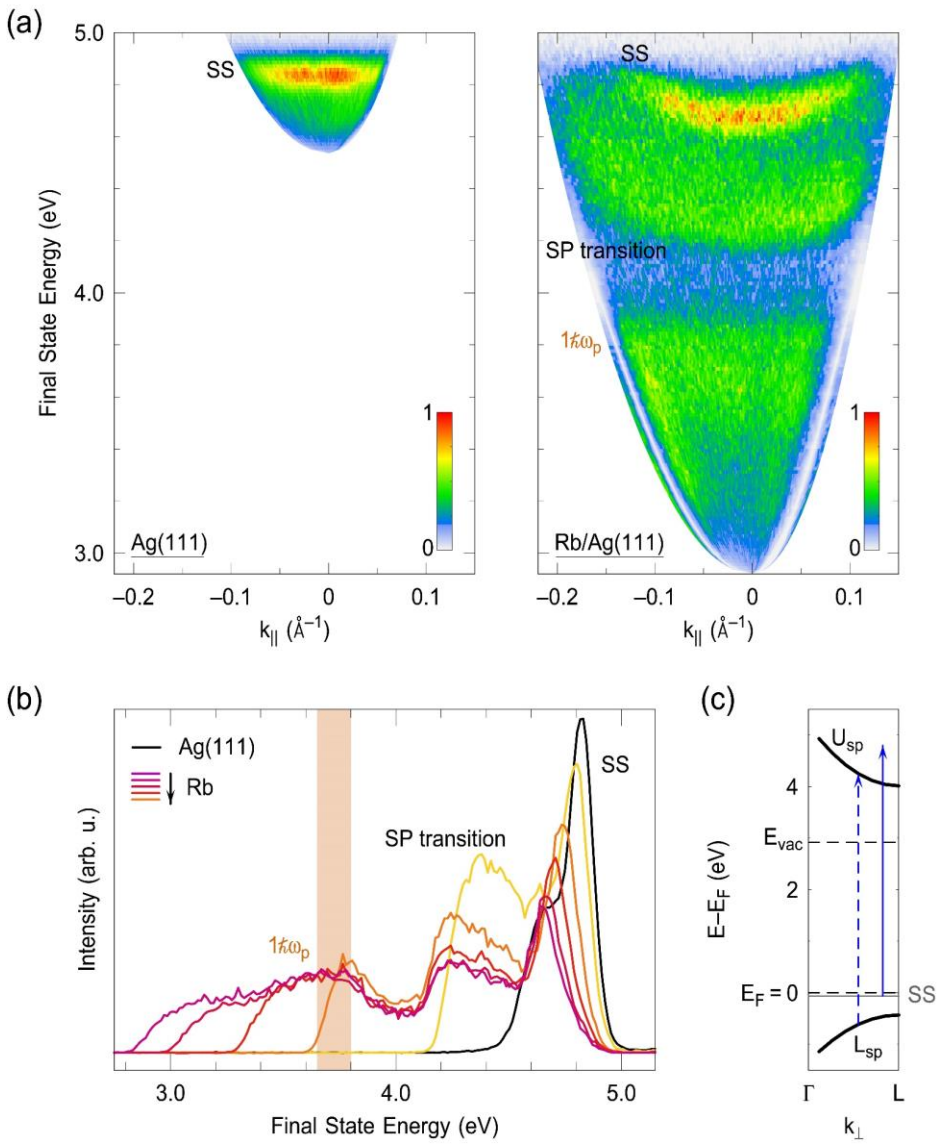

Figure 4.7 Photoemission spectra for different Rb coverages on Ag(111). (a) $E_f(k_{||})$-distributions as excited with a Hg-lamp ($\hbar\omega_I$ = 4.86 eV) of the pristine Ag(111) (left) and the Rb/Ag(111) (right) surface. (b) Energy-resolved 1PP spectra of Rb/Ag(111) for $k_{||}$ = 0 Å^{-1}; the Rb coverage is increased progressively to lower the work function. For the pristine Ag(111) surface (black spectrum), only the SS state is recorded. As the work function decreases from ≈ 4.5 eV (clean surface, black spectrum) to ≈ 3.1 eV (purple spectrum), the resonant 1-photon transition between L_{sp}, and U_{sp} becomes apparent at a final state energy of E_f ≈ 4.2 eV. At a final state energy of E_f ≈ 3.7 eV = 1$\hbar\omega_p$, electrons emitted from E_F by the decay of one bulk plasmon are detected. The 1$\hbar\omega_p$–features has a broad line shape in energy and momentum space. (c) $k_\perp$-resolved band structure in

the Γ-L direction indicates the 1-photon *sp*-transition (dashed line) and SS state excitation (solid line) ($E_{vac} \approx$ 3.1 eV).

4.2.3 Comparison with Ag(100) Spectra

As discussed in Chapter 1, for Ag(100), projected band gaps of the bulk band structure exist at the $\bar{\Gamma}$-point from 1.6 to 6.6 eV and SS state appears as broad surface resonance at 1.3 eV above E_F. The IP1 state still lies in the band gap of Ag(100), similar with that of Ag(111).

Figure 4.8 shows the corresponding 2PP spectra of the Ag(100) surface for excitation through ENZ. For $\hbar\omega_l < \hbar\omega_p$, the main feature of the spectrum is the E_F signal which is a two-photon excitation from the Fermi level and the intermediate SS resonance signal which must be excited from the bulk L_{sp} band. Like the $U_{sp} \leftarrow L_{sp}$ transition of Ag(111) which diminishes above ENZ, the intensity of SS resonance on Ag(100) is substantially suppressed above ENZ, where the plasmonic response no longer intensifies the surface fields. Moreover, the IP1 state remains for both surfaces.

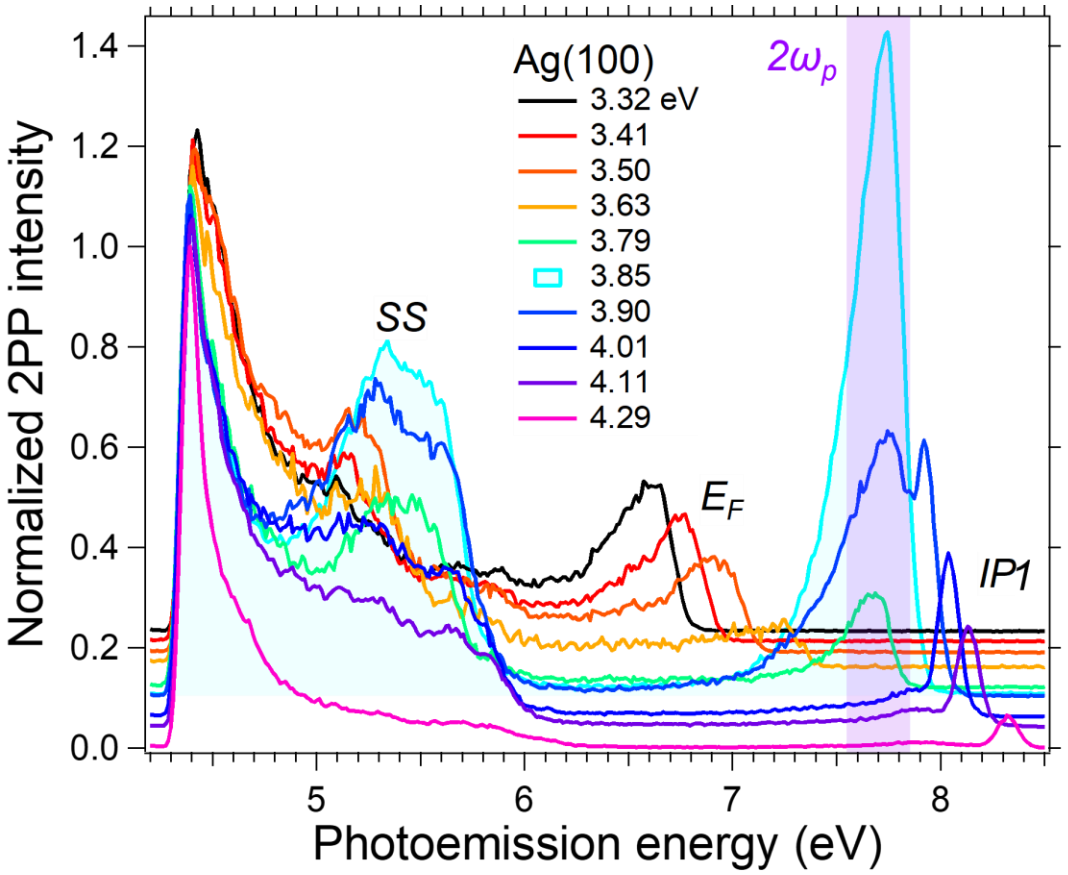

Figure 4.8 2PP spectral profiles of Ag(100) surfaces at $k_{||}$=0 Å^{-1} with different $\hbar\omega_l$ through the ENZ region. The spectra are normalized at their work function edges, and offset vertically according their $\hbar\omega_l$ (indicated in the legends). The blue shading highlight the ENZ excitation, where the $2\hbar\omega_p$ peak intensity is maximum. The purple shading emphasizes the $2\hbar\omega_p$ peak, and how its energy shifts modestly while its intensity decreases as $\hbar\omega_l$ tunes above ENZ.

Except for the bulk bands, similar with Ag(111) surfaces, tuning the $\hbar\omega_l$ through ENZ on the Ag(100) surface also marks the sudden onset of the $2\hbar\omega_p$ peak of the plasmonic origin at the E_F edge (high energy limit in Figure 4.8 highlighted by purple shading). Above ENZ, the $2\hbar\omega_p$ peak persists with diminishing intensity; moreover, it modestly shifts to higher energy, which is much less than an integer factor of $\hbar\omega_l$, which portends its non-Einsteinian character. The observation of the $2\hbar\omega_p$ peak on both surfaces is striking, as especially the surface projected band

structure is significantly different. The $2\hbar\omega_p$ peak is resolved, irrespective of the disposition of SS with respect to the surface projected band gap, or the IP1 state populations, indicating that it is independent of the surface electronic structure, as originally proposed in Ref. 39. This is next further substantiated for the Ag(110) surface, for which the $2\hbar\omega_p$ peak is prominent, but the IP1 state, which is expected to be a broad resonance at the $\bar{\Gamma}$ point [45], is not observed.

4.3 Atomic Structure Mediated Plasmonic Photoemission on Ag(110) Surfaces

As discussed in Chapter 3, the spectroscopic feature of the S3 state in Ag(110) 2PP spectra has been attributed to its participation as the final state in the non-Einsteinian plasmonic photoemission [36]. In the remaining sections of this chapter, I will address its plasmonic excitation mechanism.

4.3.1 Plasmonic Photoemission on Ag(110) Surfaces

In Figure 4.9, I present 2PP spectra at the $\bar{\Gamma}$ point of the Ag(110) surface for excitation geometry where the sample [001] or [$1\bar{1}0$] crystalline axes lie in the optical plane, respectively, with *p*- and *s*-polarized excitation in the $\hbar\omega_l$=3.41-4.15 eV range. The 2PP spectra peak at the work function edge and decrease in intensity towards the E_F edge, mirroring the Drude and secondary electron contributions of the (111) and (100) spectra [47, 62, 90, 174, 175]. On top of this unstructured signal, the only sharp feature is the $2\hbar\omega_p$ peak because the Ag(110) surface has no interband bulk transitions or unoccupied surface states at the $\bar{\Gamma}$ point, as discussed in Chapter 1. This 2PP signal response in Figure 4.9 causes the E_F edge of the spectra to persistently be elevated for excitation

below ENZ, but for $\hbar\omega_l$>3.7 eV, it develops into a peak-like feature that localizes at 7.5-7.6 eV. This change suggests that for $\hbar\omega_l$<3.7 eV longitudinal bulk plasmon responds nonresonantly, and only develops into a $2\hbar\omega_p$ peak when on-the-energy-shell excitation becomes possible for $\hbar\omega_l \geqq$ 3.7 eV. Alternatively, this elevated signal could also arise from the multipole plasmon screening response of Ag [162], which could become apparent on Ag(110) surface, which lacks pronounced transitions at the $\bar{\Gamma}$-point. The superposition of the plasmonic signal on top of the Drude background in Figure 4.9 is remarkably similar to that calculated in Figure 1 of Ref. 156 by Hopfield, for the plasmonic excitation of electrons from E_F through ENZ.

The fact that the $2\hbar\omega_p$ peak appears with both *p*-and *s*-polarizations, respectively, for the [001] or [1$\bar{1}$0] crystalline orientations is a manifestation of the dielectric anisotropy of the (110) surface, which is significantly different from the isotropic Ag(111) and Ag(100) surfaces and will be rationalized in the next two sections.

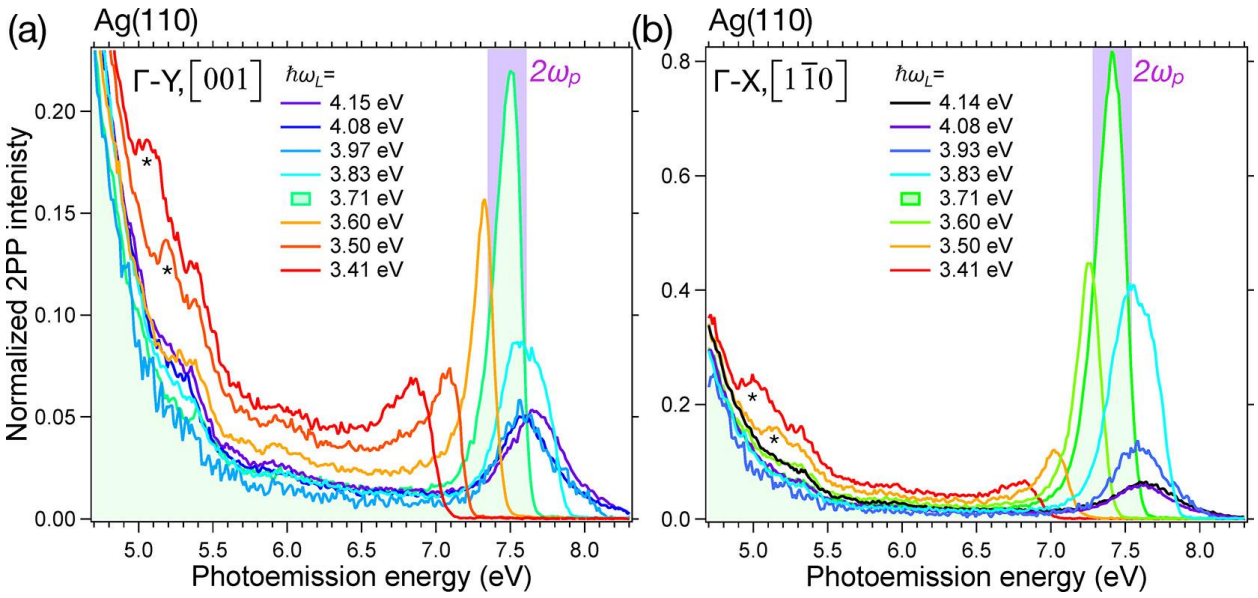

Figure 4.9 The $k_{\parallel}$=0 Å^{-1} profiles of 2PP spectra of Ag(110) surface recorded for $\hbar\omega_l$ =3.41-4.15 eV with (a) *p*-polarized light and sample oriented with its [001] crystalline axis in the optical plane, and (b) with *s*-

polarized light and the $[1\bar{1}0]$ axis in the optical plane. The spectra are normalized at the work function edges (not shown). The green shadings highlight the ENZ excitation, where the $2\hbar\omega_p$ peak intensity is maximum. The purple shading emphasizes the $2\hbar\omega_p$ peak.

4.3.2 Effect of the Final State Dispersion on the Plasmon Peak

In the 2D 2PP spectra for excitation at ENZ in Figure 4.10, the $2\hbar\omega_p$ photoemission appears as $k_{||}$ dependent bands for the two orientations of Ag(110) with energy minima $E_f \approx E_F+2\hbar\omega_p$ at $k_{||}$=0 Å^{-1}, similar with the momentum microscope data in Chapter 3. The significant difference in $k_{||}$ ranges for the two crystal orientations is attributed to a plasmonic excitation of electrons by ~$2\hbar\omega_p$ from E_F into a surface state at ~7.6 eV, which is referred to as S3 state in Chapter 3; it is calculated to exist at 7.14 eV in a minigap within the bulk *sp*-bands [Figure 1.3(b)]. As discussed in Chapter 3.2.3, the observed $2\hbar\omega_p$ peak dispersion with $k_{||}$ in the $[1\bar{1}0]$ crystal orientation is similar to that recorded for the (111) surface [93], and appears to follow the calculated band mass of 1.75 m_e for the S3 state. By contrast, for the $[001]$ orientation, the $2\hbar\omega_p$ peak signal is limited to a narrow $k_{||}$ range, which may also be defined by the S3 state. According to the band structure in Figure 1.3(b), the S3 state is strongly dispersive in the $[001]$ direction with a band mass of 0.11 m_e, which appears to limit its contribution to a high DOS region at the band minimum. Because the $2\hbar\omega_p$ peak on the (110) surface is modestly below those of the (111) and (100) surfaces, and its energy and momentum distributions appear to be defined by the S3 state, we reason that two-plasmon transitions terminates in it, and photoemission occurs from there.

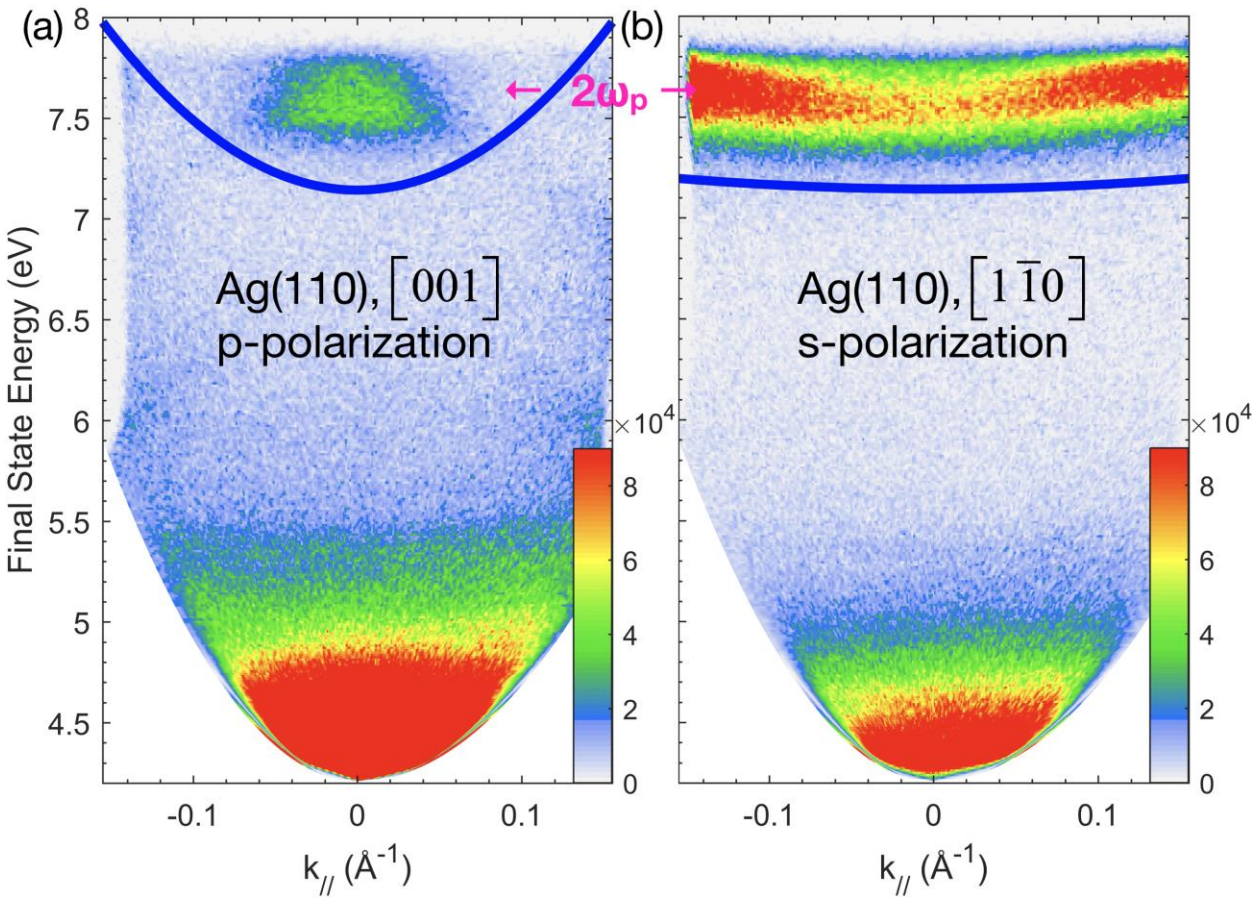

Figure 4.10 2D $E_f(k_{||})$ spectra recorded for the Ag(110) surface showing 2PP signal for $\hbar\omega_l$ =3.83 eV where Drude absorption provides a featureless background starting from above E_{vac} (~4.25 eV), on top of which sits the $2\hbar\omega_p$ peak near $E_f = 2\hbar\omega_l + E_F$ (~7.6 eV). (a) When the sample [001] crystalline axis in the optical plane, *p*-polarized excitation excites the $2\hbar\omega_p$ peak such that its dispersion is truncated within a $|k_{||}|$=0.05 Å^{-1} range. (b) When the sample [1$\bar{1}$0] crystalline axis is in the optical plane, however, *s*-polarized light excites the $2\hbar\omega_p$ peak such that it disperses through the entire detected region. The blue curves show the energy and dispersions of the S3 state from a DFT calculated band structure of Ag(110).

4.3.3 Polarization Dependence of the Plasmon Excitation

The second noteworthy aspect of the $2\hbar\omega_p$ plasmonic response of the Ag(110) surface is its dependence on polarization of the excitation light. In Figure 4.11 we plot cross sections at $k_{||}$=0

Å^{-1} through the 2D data, such as in Figure 4.10, as the polarization is rotated from *p* to *s*. The 2PP spectra for the [001] crystal orientation in Figure 4.11(a) show that both the Drude absorption, and the $2\hbar\omega_p$ peak are maximized for the *p*- and minimized for the *s*-polarization, just as for the (111) and (100) surfaces (not shown), and is consistent with screening of surface parallel fields. Surprisingly, however, in the $[1\bar{1}0]$ crystal orientation of the Ag(110) surface [Figure 4.11(b)], whereas the Drude signal varies in the same manner as for the [001] orientation, the $2\hbar\omega_p$ feature, by contrast, is minimized for the *p*- and maximized for the *s*-polarization. Ergo, Figure 4.9(b) reports the $\hbar\omega_l$ dependence of the $2\hbar\omega_p$ peak for the *s*-polarized excitation. Thus, *s*-polarized light directed against the surface corrugation excites photoelectrons that disperse along the atomic rows orthogonal to it, and *p*-polarized light propagating against to the surface corrugation excites photoelectrons that are confined to a narrow $k_{\|}$ range orthogonal to the corrugation.

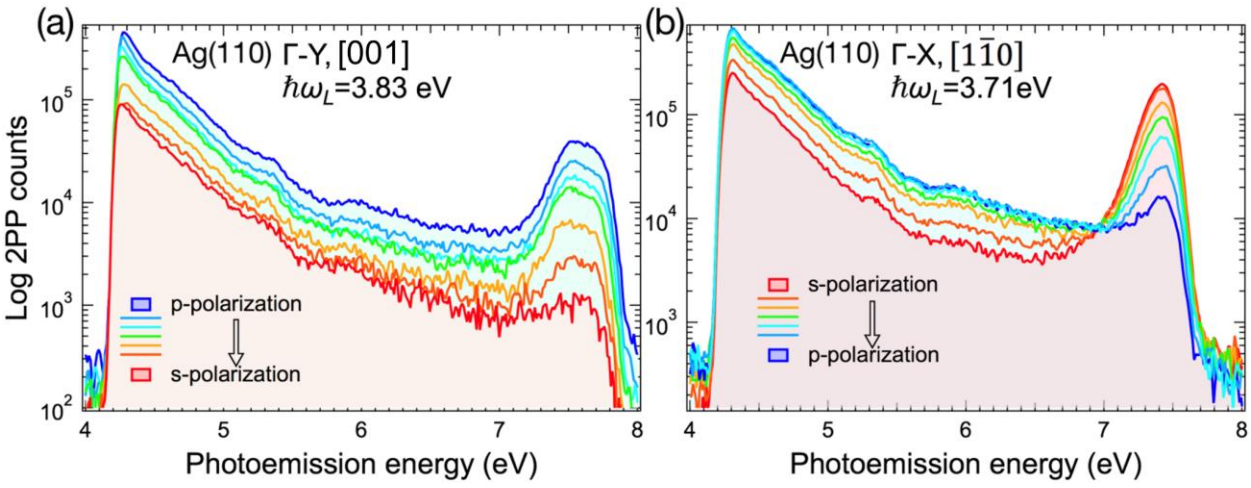

Figure 4.11 The polarization dependence of the 2PP spectra of Ag(110). $2\hbar\omega_p$ peak sits near $E_f=2\hbar\omega_l+E_F$ (~7.4 eV) and Drude absorption signal is maximum at E_{vac}. The 2PP intensity is shown on a logarithmic scale. (a) For the [001] crystalline orientation, the $2\hbar\omega_p$ peak at $E_f=2\hbar\omega_l+E_F$ is maximum for *p*-polarization (blue shading) and minimum for *s*-polarization (pink shading), just like the underlying Drude signal. (b) For the

[$1\bar{1}0$] crystalline orientation, the $2\hbar\omega_p$ feature signal is *minimum* for *p*-polarization and *maximum* for *s*-polarization, *opposite* to the Drude signal.

Such polarization dependence is exceptional because the boundary conditions for a jellium metal model demand that the surface parallel fields add up to zero [2]. The dominant excitation of a plasmonic mode by *s*-polarized light repudiates the canon that *p*-polarized light preferentially induces photoemission [2, 49, 138, 176, 177], but is not unprecedented. A pertinent antecedent is an interband two-photon transition from the *d*-band that terminates in the counterpart of the U_{sp}-surface band of Cu(110), which also appears only for the *s*-polarized transitions [178]. For the Ag(110) surface, however, excitation to the S3 state has a plasmonic origin, because its *d*-bands are too deep to play a role in the observed 2PP spectra.

A possibly related optical response of Ag(110) is the enhanced transition from S1 to S2 state by the surface parallel field which has a component in the [001] direction, as discussed in Chapter 1. Since the S1 state is localized in the atomic troughs, and the S2 state is elevated onto the ridges, such surface parallel fields at the Ag(110) surface couple the laterally displaced S1 and S2 bands and contribute to the enhanced transition signal [48]. However, in this plasmonic photoemission case, the conundrum that remains is how a surface tangential field of *s*-polarized light can excite the longitudinal plasmon mode. This is clearly an aspect of the anisotropic dielectric response of the Ag(110) surface, because on the Ag(111) and (100) surface the $2\hbar\omega_p$ peak is dominantly excited with *p*-polarization. Such coupling of the optical and the local surface fields is not possible within Feibelman's model for the nonlocal dielectric response of a jellium metallic surface, that does not consider the crystal structure to vectorial electromagnetic fields [2]. The atomic scale anisotropy of the (110) surface provides insight into how the free electron response may drive the longitudinal response. We conjecture that the atomic scale corrugation of

the Ag(110) surface enables the unexpected excitation of the longitudinal plasmonic response by the surface tangential field. Note, that for Ag(110) surface, the $2\hbar\omega_p$ peak is the strongest when the excitation field has a component that is orthogonal to the surface corrugation in the [001] direction, and it is minimized when the field is parallel to it in the $[1\bar{1}0]$ direction. We conjecture that a [001] directed field can drive charge from the occupied S1 to the unoccupied S2 state, or from the grove to the ridge, enabling the tangential optical field to drive a normal polarization component. The 2PP spectra suggest that the atomic scale surface polarization by the tangential field is more effective than the surface normal field in driving the longitudinal plasmon excitation. Such vectorial coupling of [001] directed surface fields can explain the nonlinear optical response of Ag(110) [55, 93], as well as is supported by Rasing *et al.*'s conclusion that for the Ag(110) surface, the excited in-plane response can occur in different directions than the driving field [51]. Thus, the plasmonic photoemission at ENZ reflects the atomic scale anisotropy of the (110) surface.

An alternative interpretation of the S3 feature that is under current consideration, is that it is a nodal line that is generated from *sp*-bands of two proximate (111) crystalline directions, which intersect at the (110) surface. The nondispersive character of S3 $[1\bar{1}0]$ direction and the strongly dispersive character in the [001] direction is consistent with this interpretation [179]. If this is the case, it implies that any material could possess nodal lines far from E_F, which in the case of Ag(110) surface, has remarkable properties that refute some expectations for optical excitation of what have been derived for the (111) and (100) surfaces. This line of thinking is worthwhile to explore, because any solid will acquire properties from intersections of electronic bands. Moreover, nodal lines at the Fermi level are of significant interest for their topological properties and as harbors of electron correlation [180, 181]. Thus, being able to access such electronic structures may advance our understanding of topology and electron correlation.

Figure 4.12 summarizes the nonlinear plasmonic photoemission from the low index surfaces of Ag; in addition to the known single particle interband and intraband excitations, the four spectra for the three low index surfaces show robust evidence for plasmonic photoemission, where at and above ENZ the optical field interacting with the surfaces induces excitation of the bulk longitudinal plasmon, which decays by selectively nonlinearly exciting electrons dominantly from E_F. Observation of the $2\hbar\omega_p$-feature on different crystalline planes of Ag is consistent with the bulk plasmon excitation, which is the only electronic response to the applied optical field that could depend weakly on the crystal orientation. By tuning $\hbar\omega_l$ through the ENZ region we can conclude that the $2\hbar\omega_p$ peak is an on-the-energy-shell response, which turns on and is maximum at ENZ, suggesting that there is an intensification of surface fields causing electrons at E_F to be promoted in energy by $\hbar\omega_p$ plasmon quanta. As $\hbar\omega_l$ is tuned by more than 0.5 eV above ENZ, the plasmonic nonlinear response appears to be defined by $\hbar\omega_p$ rather than $\hbar\omega_l$, suggesting that the external $\hbar\omega_l$ field generates the internal $\hbar\omega_p$ field, which drives the nonlinear photoemission, and the energy difference between them must be taken up by additional electron-hole pair excitations.

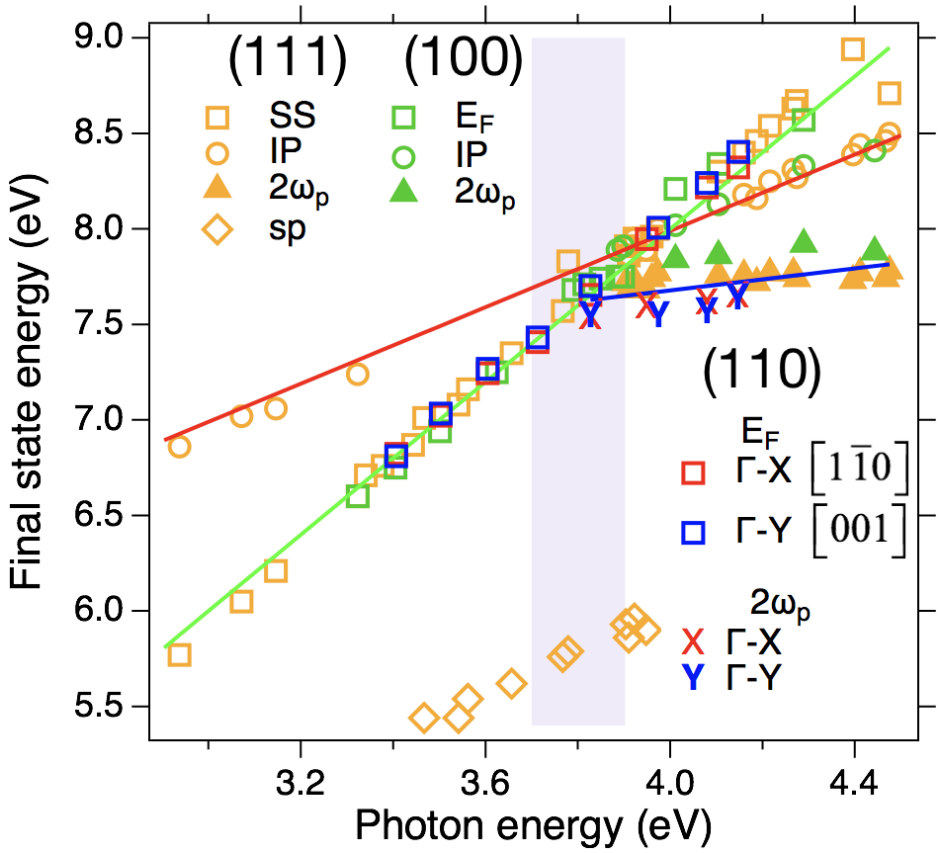

Figure 4.12 Dependence of the final state energy $E_f(k_{\|}=0^{-1}$ Å) of the single particle and collective spectroscopic features on $\hbar\omega_l$. The E_f values from 3 low-index silver surfaces are plotted together to enable their comparison. Einsteinian, single particle photoemission follows the red and green lines representing one and two photon processes. The onset of the $2\hbar\omega_p$ peak is $\hbar\omega_l$=3.7-3.9 eV (purple shading) coinciding with the Re[$\varepsilon(\omega_l)$]~0], i.e., the ENZ condition. For $\hbar\omega_l$>3.7-3.9 eV, the $2\hbar\omega_p$ peak tunes with a slope of 0.29 (blue), consistent with a non-Einsteinain, collective, process where the external field excites an internal field, which drives the 2PP process.

5.0 Coherent Non-Resonant Excitation Dynamics on Ag(111) Surfaces

I have discussed the spectroscopy part of my research in the previous two chapters. Starting from this chapter, I will discuss the coherent dynamics of several nonlinear excitation processes measured by the ITR-mPP method. In this chapter, I will establish the principles of nonlinear coherent excitation dynamics by exploring the non-resonant excitation from SS state on Ag(111), which is well known in 2PP spectroscopy but little is known from the perspective of mPP dynamics. I will first examine this excitation using 2PP OBE simulation, and subsequently, address the related coherent excitation dynamics in higher-order 3PP, 4PP, and even ATP (5PP) excitation schemes. A correlation was found between the polarization field excited in the sample and the final photoelectron distribution. This confirms our understanding of ATP as a one-step coherent mPP process instead of a two-step sequential process, as it is described in literature with scant evidence [71-74]. At the end of this chapter, I will also discuss the polarization beating pattern that can be observed in inter-*sp*-band excitation on Ag(111). The content in this chapter is based on a publication in Physical Review X [43] and preliminary results at the current stage of analysis.

5.1 Fourier Analysis of Non-Resonant 2PP SS State Excitation Dynamics

The energy- and $k_{\parallel}$-resolved 2PP spectrum of Ag(111) excited with $\hbar\omega_l$ =3.32 eV photons, which has served as an example in Chapter 1, is shown again in Figure 5.1(a). The main 2PP spectral features involve the non-resonant excitation from SS state and resonant two-photon transition from *sp*-band. In this section, I will demonstrate the coherent dynamics of the SS state

excitation by an OBE simulation instead of experimental data, because the OBE approach has proven useful to analyze ITR-mPP data and depicts the key spectroscopic features [6, 68, 69, 82, 83, 182]. In ITR-mPP data, 2PP signal is obtained as delay τ is varied interferometrically between identical pump and probe pulses [Figure 5.2(a)]. The calculation is based on a 3-level system as shown in Figure 5.1(c), which qualitatively depicts the 2PP excitation pathway of SS state in Figure 5.1(a) and (b). The surface and bulk states appear independently in the mPP spectra, and hence we do not model the U_{sp}←L_{sp} transition, whose spectra have been modeled in published literature [62, 63]. These prior studies, however, justify the approach taken here.

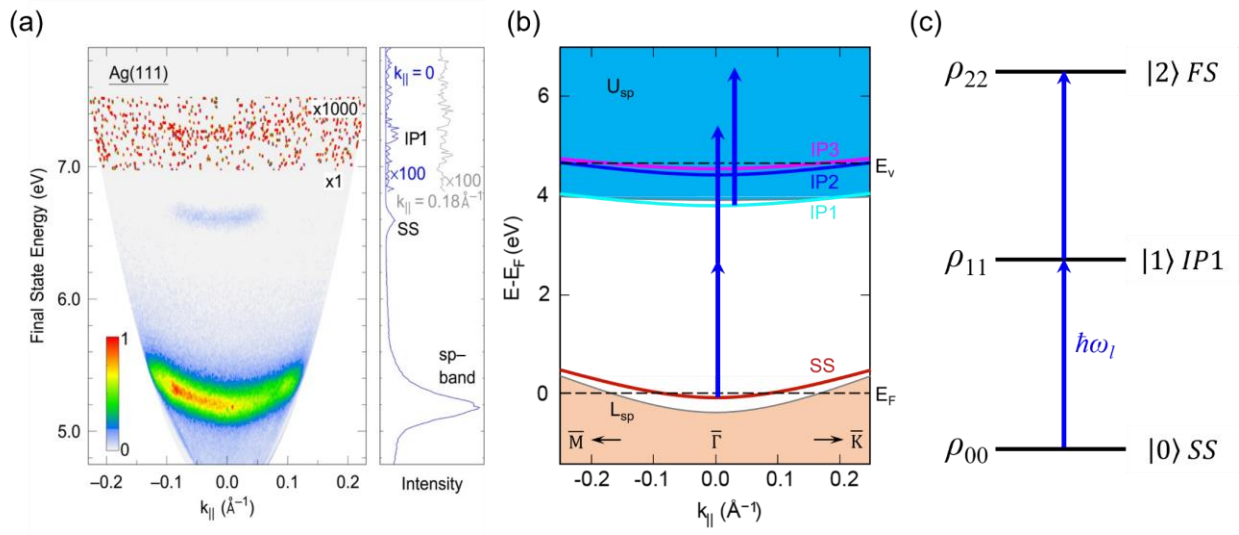

Figure 5.1 2PP spectra and excitation model of Ag(111). (a) Energy- and $k_{||}$-resolved 2PP spectra of Ag(111) for excitation with $\hbar\omega_l$ = 3.32 eV; the spectral elements are identified in the line profile (right panel) taken at $k_{||}$ = 0 Å^{-1}. The color-scale above 7 eV is amplified by a factor 1000 to show the weak contribution of the IP1 state signal. (b) Surface projected band structure of Ag(111) with the corresponding excitation diagram of SS and IP1 state [19]. (c) Diagram of a canonical 3-level system used in OBE simulations applied to modelling of 2PP excitations in (a) and (b), which consists of the occupied initial state SS, the unoccupied intermediate state IP1, and the final state FS in the photoemission continuum.

In the OBE calculation, the SS state is excited into the final state continuum by coherent two-photon absorption in near resonance with the IP1 state [Figure 5.2(b)]. As the interaction commences, the photoexcited bandwidth is wide and will encompass the IP1←SS transition. As it evolves in time, it narrows through destructive interferences in its wings and constructive interference at the driving frequency [183]. Dephasing of the IP1-SS coherence can retain some population in the IP1 state, as is observed in the 2PP spectrum of Figure 5.1(a). Thus, the final state signal includes both the coherent two-photon absorption from SS state as well as photoemission of the dephased population that is retained in the IP1 state. The photon energy is set to separate the spectral features of the IP1 state from the SS state. For nonresonant excitation, quantum interference caused by final state excitation through two different pathways is negligible [69]. Thus, the calculated 2PP signal predominantly reproduces the photoelectron current generated by rectification of the two-photon coherence for excitation from the occupied SS state.

In Figure 5.2(a) (right), we show line profiles at constant energy [interferometric two-pulse correlations (I2PCs)] through the calculated two-pulse E_f vs. τ interferogram, for the final state energies of the SS and IP1 states; similar correlation traces oscillating at the driving laser frequency and its second harmonic were observed in the original ITR-2PP study of the SS state on Cu(111) [68], but the present measurements on Ag(111) are recorded with 2D $E_f(k_{||})$ spectroscopic data acquisition. The I2PC signal of the IP1 state has a slow component due to its incoherent population decay of ~30 fs, as is measured in two-color 2PP [41]. The inset of Figure 5.2(a) shows expanded SS component of the ITR-2PP data for time delays that are comparable or longer than the laser pulse. It is evident that the signal is composed of dominant coherent oscillations at the driving laser frequency ($1\omega_l$) and subordinate ones at its second-harmonic ($2\omega_l$) [6, 68]. The $2\omega_l$ interferences are particularly evident in the signal from SS, because its hole dephasing time is slow, and electron is

excited to the vacuum continuum [56, 68]. In addition to these oscillations following external field, the signal is also affected by the coherent polarization field, which is reflected by the tilt of interference fringes towards τ = 0 fs with increasing final state energy [inset of Figure 5.2(a)] , which we will show is the *prima facie* evidence for coherence in a 2PP process . We stress that OBE simulations reproduce the energy- and phase-resolved mPP measurements of the coherent electron dynamics in Ag(111), as will be evident in experimental results for higher order processes.

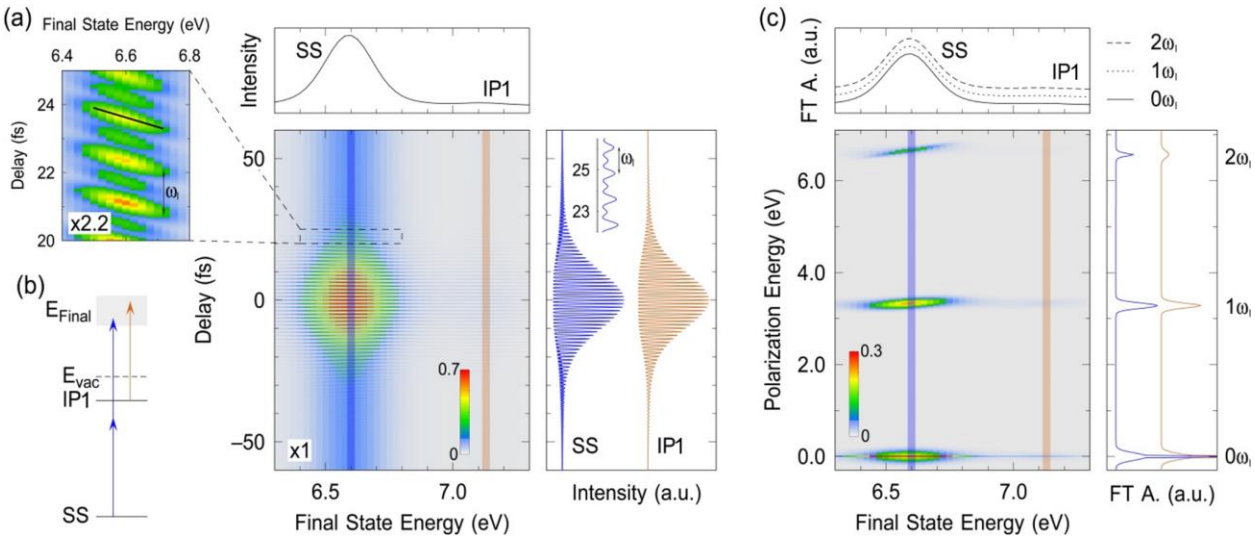

Figure 5.2 OBE simulation of ITR-2PP spectroscopy. (a) OBE simulation of an energy- and phase-resolved ITR-2PP interferogram for the nonresonant 3-level system shown in (b). The center plot in (a) shows the calculated ITR-2PP interferogram, specifically population of the final state (color-coded) as a function of E_f and τ. Top: The final state energy spectrum consisting of the SS and IP1 states is a profile through the calculated ITR-2PP data at τ=0 fs. Right: I2PC traces are profiles through the calculated ITR-2PP data at energies of SS and IP1 states. The color-coded expanded inset of ITR-2PP shows oscillations at $1\omega_l$ and $2\omega_l$, and interference fringes tilting towards τ = 0 fs with increasing final state energy (highlighted by the black line at ~24 fs). (c) 2D-FT photoelectron spectra obtained by Fourier transformation of the delay axis in (a). The polarization energies (the Fourier axis) induced in the sample at $0\omega_l$, $1\omega_l$ and $2\omega_l$ are correlated with the

final state energies. Top: Normalized Fourier filtered 2PP spectra at $0\omega_l$, $1\omega_l$ and $2\omega_l$ (bottom to top). Right: line profiles taken at the SS and IP1 state energies showing FT amplitudes of the $0\omega_l$, $1\omega_l$ and $2\omega_l$ oscillations.

To further analyze the calculated ITR-2PP data, we Fourier transform (FT) the delay axis to generate 2D-FT photoelectron spectra, which correlate the polarization energies that are excited in the sample, and appear as coherent oscillations, with final state energies where the 2PP process terminates [Figure 5.2(c)]. Local FT features of the 2D-FT spectra occur at the $0\omega_l$, $1\omega_l$, and $2\omega_l$ energies where the $1\omega_l$, and $2\omega_l$ represent the linear and second-order nonlinear polarization of surface electrons driven by external field. For a three-level system, $1\omega_l$ and $2\omega_l$ coherences have dominant contributions between the nearest neighboring $\rho_{m(m+1)}$ and next-nearest neighboring $\rho_{m(m+2)}$ states, respectively. The $0\omega_l$, however, represents the envelope function of the interferogram, including the relatively slow incoherent population dynamics of the intermediate state, which is integrated over time in recording the coherent and incoherent contributions to 2PP signal [6, 182, 184].

Figure 5.3(a) shows enlarged elements of the 2D-FT photoelectron spectra of the SS state in Figure 5.2(c). The polarizations that oscillate at the $1\omega_l$ and $2\omega_l$ frequencies are rectified to produce the final states in the 2PP process. The polarization ranges cover widths of the driving frequency ω_l and its harmonics. The FT amplitudes of the linear ($1\omega_l$) and the second-order non-linear ($2\omega_l$) polarizations tilt up with increasing final state energy. This tilt is caused by the coherent excitation from a discrete initial state by an ultrafast laser pulse with a broad frequency spectrum, which induces primarily linear polarization oscillations over a broad frequency range (~0.1 eV) centered on ω_l. Likewise, the nonlinear polarizations are also excited and oscillate at $2\omega_l$ and a perturbative series of higher-order harmonics. As sketched in Figure 5.3(b), the spectral

frequency components of polarizations at $1\omega_l$ or $2\omega_l$ correlate with specific final states, satisfying energy conservation and energy-time uncertainty. Thus, in a coherent *m*-photon excitation process of a discrete state, slopes of the 2D spectral features are given by *n/m*, where *m* is the order of photoemission (e.g., *m* = 2, 3, 4, …) and *n* is the order of polarization ($n\omega_l$; *n* = 1, 2, …, $n \leq m$) contributing to the signal. For example, for the coherent 2PP process of the SS state of Ag(111), the slopes of the $1\omega_l$ and $2\omega_l$ FT amplitudes are *n/m* = 1/2 and 2/2, respectively [Figure 5.3(a)].

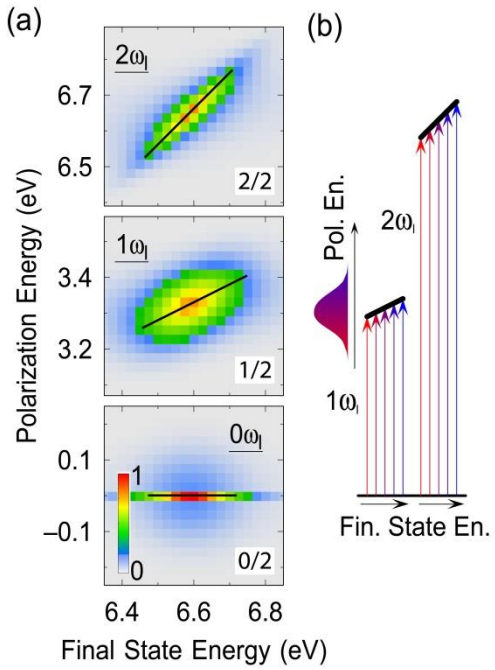

Figure 5.3 Expanded 2D-FT spectra and polarization excitation schematic. (a) Expanded components of the OBE calculated 2D-FT spectra corresponding to the SS state signal from Figure 5.2(c). The color table of each polarization order ($0\omega_l$, $1\omega_l$, $2\omega_l$) is scaled separately. The 2D spectra for the zero-order component $0\omega_l$ is horizontal; the 2D spectra at the driving laser frequency $1\omega_l$ and its second-harmonic $2\omega_l$ tilt with the final state energy; the slopes for a coherent process are indicated by black lines and quantified by the ratios in the white boxes. (b) Schematic illustration of how the induced polarizations produce the tilted FT amplitudes in the 2D spectra: Each frequency component within the spectral range of the laser pulse terminates at a specific final state energy; left: linear polarizations, right: second-order polarizations.

The energy tilting of components of 2D-FT photoelectron spectra is an FT manifestation of the tilting of interference fringes in the time-domain spectra. Specifically, the tilted interference fringes in the inset of Figure 5.2(a) signify that each frequency component of the broadband excitation pulse causes the induced polarization to oscillate at its frequency. Thus, if each frequency component correlates with a specific final state energy, the plot of the final state energy vs. the delay time will have tilted interference fringes since different final state energy components will have different oscillation periods, resulting in maximum signal of each energy component appearing at different delay time. The tilt of the fringes gives insight into optical coherences induced by the laser field in the sample [82]. Similar fringe tilting is also observed in optical spectroscopies that involve interferometric scanning, frequency resolved optical spectroscopic detection of coherent responses, such as frequency-resolved optical gating or second harmonic generation, and coherent attosecond spectroscopic studies [185-188].

In photoemission spectroscopy, however, it is possible that the correlation between the polarization frequency and the final state energy is erased. This happens when the inhomogeneous broadening is large, because populations at different energies oscillating at different frequencies can be excited to the same final state. This is observed in the experimental ITR-mPP and 2D-FT data from polycrystalline Ta (sample holder; Figure 5.4). Likewise, if dephasing is very fast, the polarization frequencies are poorly defined through energy-time uncertainty, which broadens the FT spectral components. In such cases, the signal oscillates with amplitude of the total electric field, rather than its frequency components, because final state energies do not correlate with specific coherences excited in the sample. Consequently, the ITR-mPP fringes do not tilt as is observed, for example, in inhomogeneously broadened polycrystalline samples [135, 189].

Coherent spectroscopies often consider the loss of coherence due to inhomogeneous broadening. In this thesis, however, for measurements on single crystal metal surfaces, this is not necessary, because the spectroscopic features are primarily broadened by homogeneous processes that cause phase and population decay through processes such as electron-electron and electron-phonon scattering. Inhomogeneous broadening would become important if the intrinsic electronic structure of a solid surface were modified by the presence of defects or impurities, or if surfaces were polycrystalline.

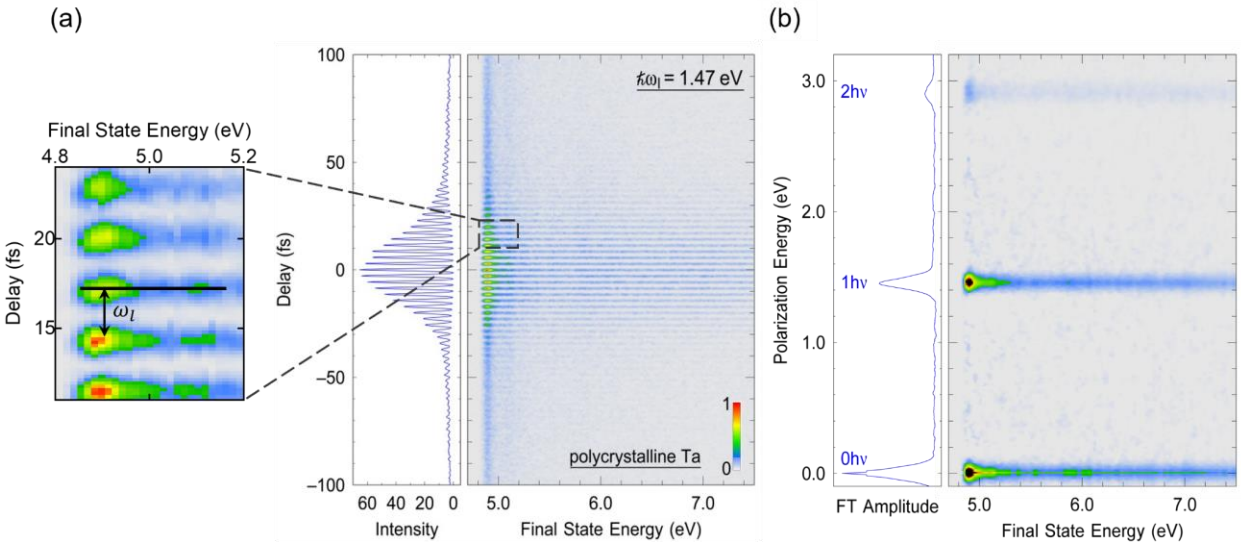

Figure 5.4 Exemplary (a) ITR-4PP and (b) 2D-FT spectra measurement from the sample holder (polycrystalline Ta) , which serves as a fourth order autocorrelation of the laser pulse at $\hbar\omega_l$ = 1.47 eV. The interference fringes oscillate at the center frequency of the laser pulse and are *not* tilted with respect to final state energy and delay. This indicates that the excitation is incoherent. The color-coded expanded inset shows flat interference fringes compared with Figure 5.2 (highlighted by the black line at ~17 fs). The FT amplitude in (b) is flat and shows *no* correlation between the polarization and final state energies.

Next, I extend my discussion to experimentally observed and OBE simulated coherences in the ITR-mPP (m = 3, 4, 5) measurements including their ATP components, and evaluate them based on the insights from the calculated ITR-2PP data in this section.

5.2 SS State Excitation Dynamics in mPP

We measure 3PP and 4PP spectra of Ag(111) for photon energies of $\hbar\omega_l$ = 1.40 and 1.60 eV (Figure 5.5). In both cases, the SS state is prominent though it is excited non-resonantly. In this excitation energy range, the dielectric function and the band structure of Ag shows no onset of inter-*sp*-band transitions which greatly modify its response [140, 147]; the excitation energy dependent electronic responses of SS states can thus be exclusively attributed to non-resonant photoemission order m. Note that although Ag absorbs light weakly in this spectral region through Drude absorption, this is a second-order process involving intraband carrier acceleration and scattering to conserve momentum [190], and thus it cannot contribute to the coherent response that we discuss. The spectra are dominated by coherent multiphoton excitation.

For $\hbar\omega_l$ = 1.60 eV [Figure 5.5(a)], photoelectrons are excited from the SS state by a coherent three-photon process. At one photon higher energy (1.60 eV) above the SS peak in 3PP, its replica with the same $k_{\|}$-dispersion range, but with >100 times weaker intensity, is also observed. We assign this structure to 4PP, or ATP, of the SS state. In addition, we observe similarly weak 4PP signals from the IP1 state and bulk excitation between the L_{sp} and U_{sp}. The energies and $k_{\|}$-dispersions of the surface states are consistent with the 3PP and 4PP processes, as well as with the 2PP data in Figure 5.1(a) and related 2PP literature [19, 39, 41, 63, 64]. Note that highly nonlinear processes like 4PP are especially sensitive to electric field strength. By tuning the focal point of

optical lens on the UHV chamber, I can excite these highly nonlinear processes in the sample with different laser fluences. It will be shown in Chapter 6 that at higher laser fluence, the light field can even modify the electronic structure of the sample, instead of simply interrogating its band structure, like what I am discussing in this chapter.

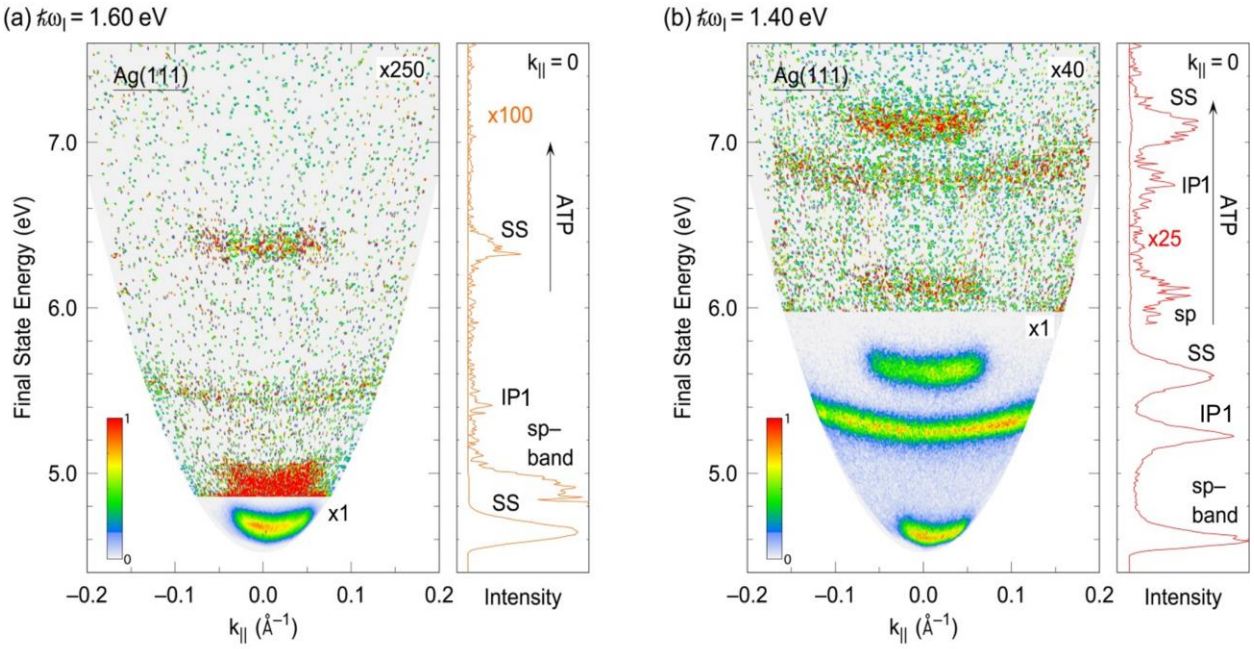

Figure 5.5 Energy- and $k_{||}$-resolved mPP spectra of Ag(111) taken with (a) $\hbar\omega_l$ = 1.60 eV and (b) $\hbar\omega_l$ = 1.40 eV. Photon energies are chosen such that nonresonant excitation of the SS state is detected by (a) 3PP and (b) 4PP; spectral features are labelled in the line profiles taken at $k_{||}$ = 0 Å^{-1}. ATP contributions show replicas of states observed in 3PP and 4PP, but translated upward by one photon energy.

For $\hbar\omega_l$ = 1.40 eV [Figure 5.5(b)], four-photon absorption is necessary to observe spectra (4PP) of the SS and IP1 states, as well as the bulk excitation between L_{sp} and U_{sp}. Again, their replicas which have comparable dispersions as the 4PP processes are detected at 1.4 eV higher energy, which is also attributed to ATP, i.e. 5PP spectra of the respective states. Significantly, the

intensity ratios of the SS and IP1 states are reversed between the 4PP and 5PP-ATP processes. This implies that in ATP, the highly non-linear 5-photon absorption process from the SS state is more efficient than the (3+2)-photon process via the transiently occupied intermediate IP1 state. Note that the IP1 state needs to be populated nonresonantly to undergo photoemission, while SS is photoemitted directly by *m*-photon absorption.

Therefore, the non-resonant excitation of the SS state of Ag(111) using near-infrared photons provides a simple system to systematically study the high-order, perturbative, coherent ultrafast electron dynamics for different orders of mPP (m = 3, 4). In the following, I will describe the experimental results for m = 4 in detail and support my conclusions with results for m = 3.

In Figure 5.6(a), I show the experimental ITR-4PP data taken with the same experimental conditions used for the 4PP spectrum in Figure 5.5(b) ($\hbar\omega_l$ = 1.40 eV, $k_{\|}$ = 0 Å^{-1}). The large peak-to-baseline ratios in the I2PC scans at the SS and IP1 state maxima result from the high nonlinearity of the excitation process. As in the calculated ITR-2PP data in Figure 5.2(a), tilting of the interference fringes towards τ = 0 fs with increasing final state energy is also observed in 4PP [inset of Figure 5.6(a)]. The tilt angles of the interference fringes similarly correlate the induced polarization energy with the detected final state energy.

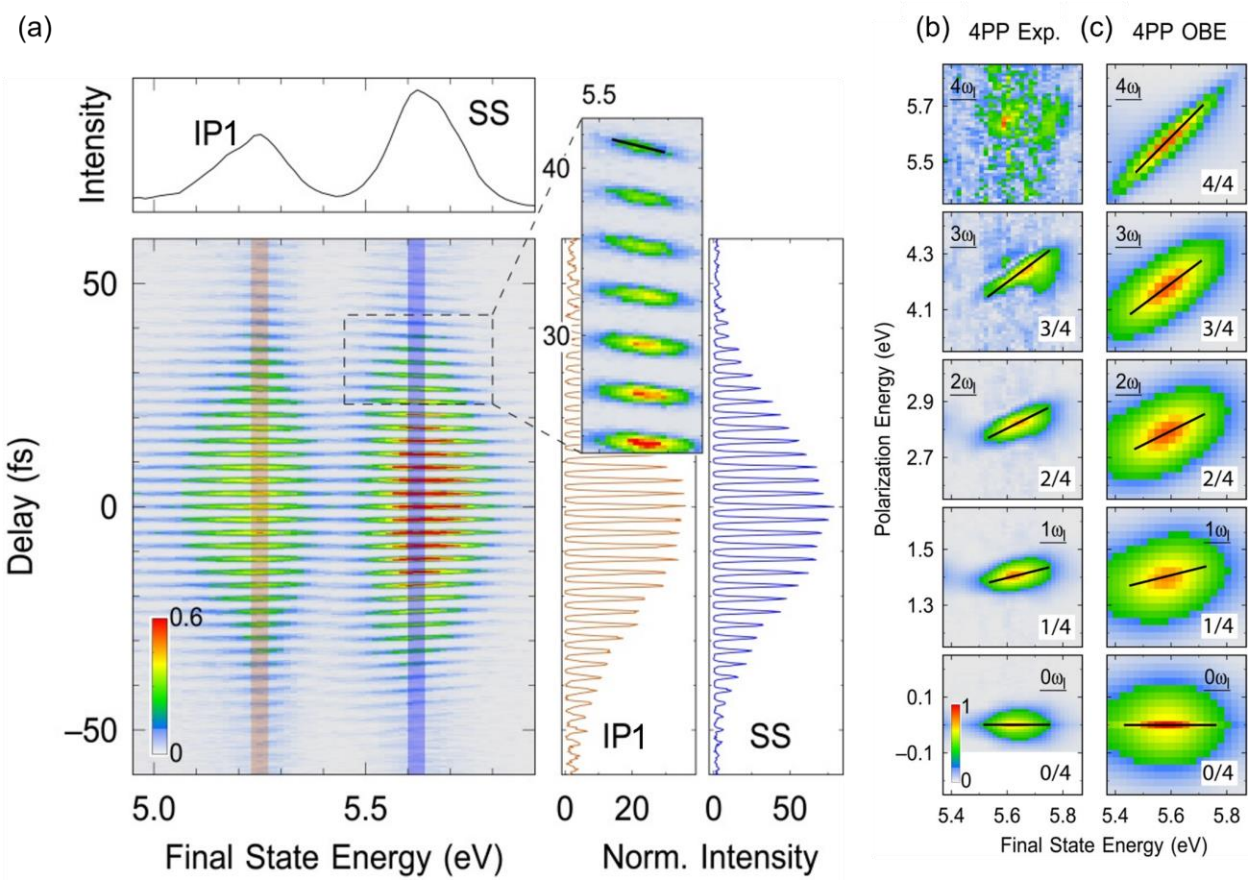

Figure 5.6 ITR-4PP experiment on Ag(111) at a photon energy of $\hbar\omega_l$ = 1.40 eV ($k_{||}$ = 0 Å^{-1}). (a) Left bottom: Color-coded photoelectron interferogram; top: energy profile taken at τ = 0 fs. Right: I2PC cross sections at the IP1 and SS final state energies. Inset: The enlarged interference fringes of the SS state; the tilt angle is marked by the black line at ~42 fs. (b, c) 2D-FT photoelectron spectral components showing the SS state signal generated by Fourier analysis of (b) the ITR-4PP experiment and (c) a 5-level OBE simulation. The color-range of each 2D spectrum is scaled independently. FT amplitudes tilt is highlighted by black lines and their slopes are quantified within the white boxes.

To analyze the coherent dynamics in more detail, Figure 5.6(b) plots the SS state components of the 2D-FT photoelectron spectra obtained from the data in Figure 5.6(a). The FT amplitudes for the $0\omega_l$ - $4\omega_l$ components again tilt, respectively, with slopes of 0, 1/4, 2/4 and 3/4 ($4\omega_l$ signal is too weak to evaluate). By applying the same arguments as for the 2PP OBE

simulation, we explain the slopes with the ratio *n/m* where now the order of the photoemission process is $m = 4$ and of the polarization is an integer multiple of the excitation frequency ($n = 0, 1, 2, 3$). In other words, to achieve 4PP from the SS state, the coherent signal is driven at harmonics of the driving frequency (numerator n), and different frequency components of the photoelectron energy correlate with the order of the multi-photon process (denominator m). To further test this interpretation, I performed an OBE simulation of the 4PP process for a 5-level system, which gives comparable 2D-FT spectral components as the experiment [Figure 5.6(c)]. The larger widths of the simulated 2D-FT spectra, as compared with the experiment, reflect faster dephasing $1/T^*_{mn}$ parameters used in the simulation.

To address the effect of the order m in mPP, we show 2D-FT data for ITR-3PP detection of the SS state in Figure 5.7(a) for $\hbar\omega_l = 1.60$ eV and $k_{||} = 0$ Å^{-1} [3PP spectrum in Figure 5.5(a)]. The ITR-3PP experiments as well as the corresponding 4-level OBE simulation [Figure 5.7(b)] confirm again the *n/m* dependence of tilting of the 2D-FT spectra in a non-resonant, coherent process, where now, $m = 3$ and $n = 0, 1, 2, 3$. The 2D-FT photoelectron spectra of the SS state thus systematically depend on the induced polarization signal ($n \leq m$) and order of the multi-photon excitation process ($m = 3, 4$).

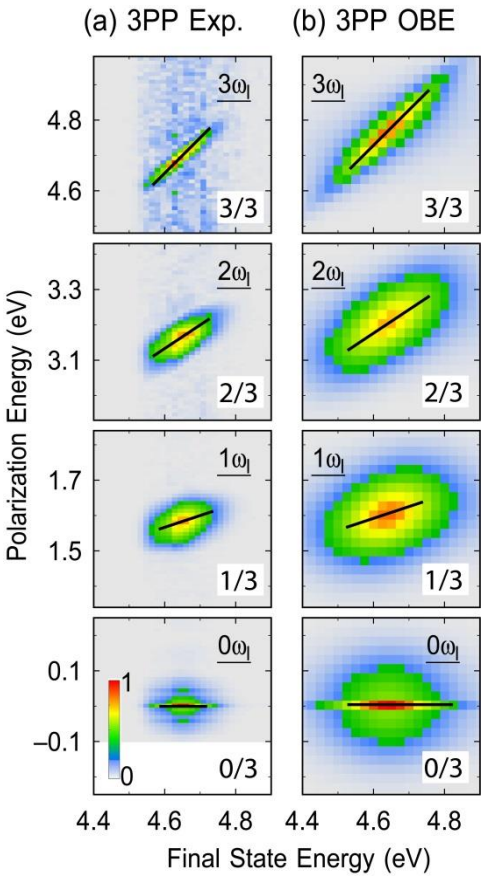

Figure 5.7 2D-FT photoelectron spectral components showing the 3PP SS signal generated by Fourier analysis of (a) the ITR-3PP experiment based on Figure 5.5(a) ($\hbar\omega_l$ = 1.60 eV, $k_{||}$ = 0 Å^{-1}) and (b) a 4-level OBE simulation. The color-range of each 2D spectrum is scaled independently. FT amplitudes tilt is highlighted by black lines and their slopes are quantified within the white boxes.

5.3 SS State Excitation Dynamics in ATP

The spectra in Figure 5.5 show clear contributions of non-resonant photoemission from the SS state following *m*- and (*m*+1)-photon photoexcitation that produce the mPP and ATP signals, respectively. The two signal components are recorded simultaneously in an ITR-mPP scan and thus can be compared, even though they differ by a factor of >100 in intensity. Here, we present

the first time-resolved measurement of ATP in a solid-state system; the coherent measurement allows us to discuss how it occurs. We first focus on the (4+1)PP ATP process [$\hbar\omega_l$ = 1.40 eV, Figure 5.8(a, b)], and subsequently generalize our observations to the (3+1)PP ATP process [$\hbar\omega_l$ = 1.60 eV, Figure 5.8(c)]. In Figure 5.8(a), we show the ITR-mPP data for the ATP processes from both the IP1 and SS states; the I2PC scan at the SS maximum shows a large peak-to-baseline ratio (larger than the IP1 state) as expected for a fifth order non-linear process. Again, we highlight coherence in the mPP process of the SS state by showing in the inset in Figure 5.8(a) that the interference fringes tilt towards τ = 0 fs with increasing final state energy. The time-domain experiment thus shows that the 5-photon excitation of ATP starting from the SS state is a coherent process.

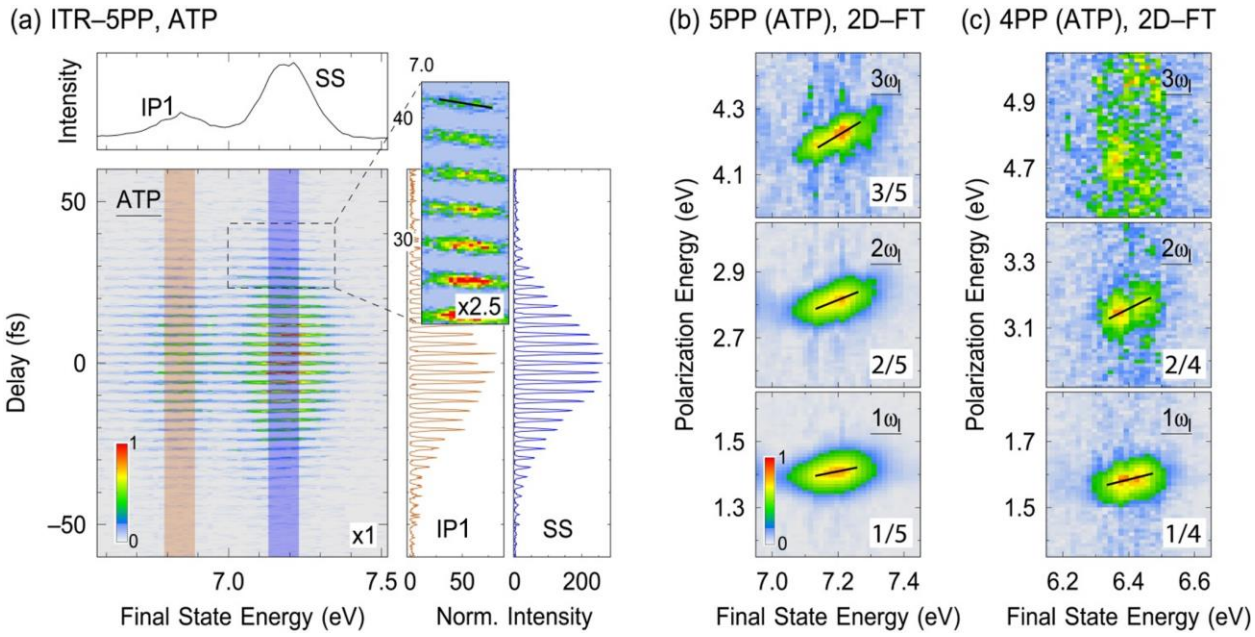

Figure 5.8 ITR-mPP experiment for the ATP component of the IP1 and SS states that are excited in a *m* = (4+1)-photon process ($\hbar\omega_l$ = 1.40 eV, $k_{||}$ = 0 Å^{-1}). (a) Left bottom: Color-coded interferogram. Top: energy profile taken for τ = 0 fs. Right: The I2PC cross sections of the SS and IP1 states. Inset: tilting of the fringes is highlighted by the black line at ~ 41 fs. (b) Components of 2D-FT photoelectron spectra of the SS state excited

in m = (4+1)-photon ATP process [FT of the data in (a)]. FT amplitude is observed for $1\omega_l$, $2\omega_l$ and $3\omega_l$; the slopes are marked with black lines and quantified within the white boxes. (c) Components of 2D-FT photoelectron spectra of the SS state excited in the m = (3+1)-photon ATP process ($\hbar\omega_l$ = 1.60 eV, $k_{||}$ = 0 Å^{-1}); tilted FT amplitude is evident for $1\omega_l$ and $2\omega_l$ as marked with black lines and quantified within the white boxes. The color-range of each 2D spectra is scaled separately.

To characterize this coherence, we generate 2D-FT photoelectron spectra of the ATP component [Figure 5.8(b)]. FT amplitudes are well structured for $0\omega_l$ (not shown) to $3\omega_l$, but higher-order components have insufficient statistics for analysis. The FT amplitudes show characteristic tilting, which in analogy we analyze in Figure 5.8(b) with the slope n/m, where m = (4+1) = 5, and n = 1, 2, and 3 for the $1\omega_l$, $2\omega_l$ and $3\omega_l$ components.

As a confirmation, we evaluate the 2D-FT data of ATP from the SS state in the m = (3+1) experiment [Figure 5.8(c), $\hbar\omega_l$ = 1.60 eV, $k_{||}$ = 0 Å^{-1}]: FT amplitudes are well resolved for $0\omega_l$ (not shown), $1\omega_l$, and $2\omega_l$, and the slopes are described with n/m, where the order of photoemission is m = (3+1) = 4 and n = 1, and 2; the FT amplitude of the $3\omega_l$ component is too weak to be evaluated. The analysis of the 2D-FT spectra of ATP in fourth- and fifth-order photoemission are thus consistent and establish the coherent nature of ATP.

The ITR-mPP data show tilted interference fringes and FT amplitudes in the time- and frequency-domains, where it is evident that the dominant mPP and the accompanying (m+1)-ATP processes arise from the same physics, but in different orders of nonlinearity. Although ATP is usually described as occurring by a sequential process involving first generation of a photoelectron through mPP, followed by it absorbing one or more photons before escaping from the surface [71-74, 98, 191], our measurements show no evidence of such sequential processes. We confirm this conclusion by performing OBE simulations that explicitly distinguish coherent and sequential

ATP shown in Figure 5.9. For coherent ATP, in agreement with the previous results, tilted FT distribution is detected while a horizontal (flat) FT distribution would result for all orders of polarization ($0\omega_l$, $1\omega_l$, $2\omega_l$, …) if ATP is a sequential (incoherent) process.

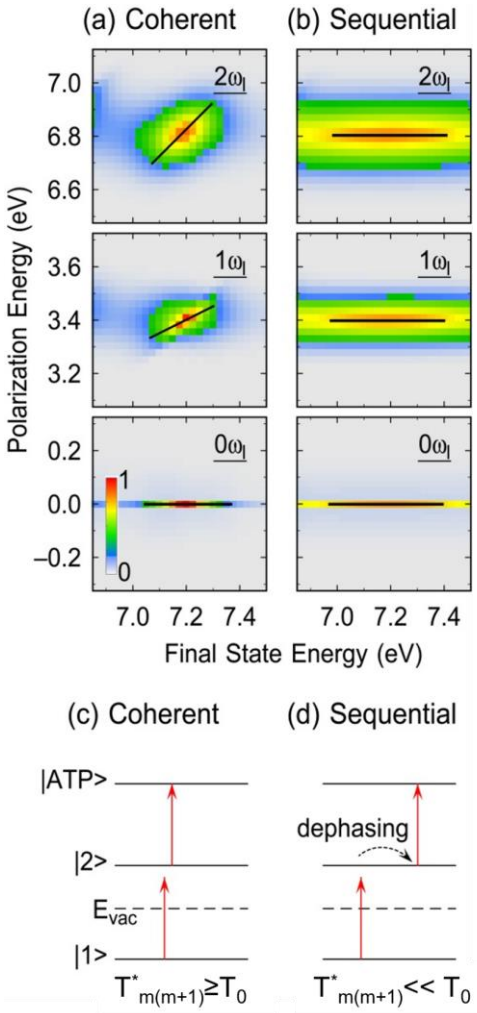

Figure 5.9 2D-FT spectra generated by OBE simulation of (a) coherent and (b) sequential (incoherent) ATP as modelled by a 3-level systems shown in (c)/(d). The *m*-photon process exciting population above the vacuum level, E_{vac}, is simplified to a non-resonant 1-photon transition from |1> to |2>; ATP is modelled by the 1-photon transition from |2> to |ATP>. (a,c) In coherent ATP, the dephasing time between the neighboring states *i* and (*i*+1) exceeds the duration of the excitation laser pulse T_0, *i.e.* $T^*_{i(i+1)} \geq T_0$. The 2D photoelectron spectra show tilted FT amplitude, similar to that observed before. (b,d) In the sequential (incoherent) ATP,

the polarization between the neighboring states dephases significantly faster than the excitation process from |2> to |ATP>, *i.e.* $T^*_{i(i+1)} \ll T_0$; for this process, a horizontal (flat) FT amplitude is observed in the 2D photoelectron spectra for all orders. Parameters used in the simulation: $E_{|1>} = -0.1$ eV, $E_{|2>} = 3.8$ eV, $E_{|ATP>} = 7.2$ eV, $\hbar\omega_l = 3.40$ eV, $T_0 = 20$ fs, $T_{|1>} = T_{|2>} = T_{|ATP>} \gg 1$ fs, $T^*_{|1>|ATP>} = 15$ fs. The pure dephasing times of next neighboring states are chosen in (a) and (b) as $T^*_{|1>|2>} = T^*_{|2>|ATP>} = 20$ fs and $T^*_{|1>|2>} = T^*_{|2>|ATP>} = 1$ fs, respectively. The width of the FT amplitude on the final state energy axis in (b) is significantly broadened compared to (a) because of the shorter dephasing times.

In the perturbative regime, the optical field thus drives SS state electrons to oscillate nonlinearly at $m\omega_l$, $(m+1)\omega_l$ and a perturbative series of higher frequencies. These coherent polarizations can produce coherent light emission at the m and $(m+1)$ harmonics of the driving field [192], as has been observed from Cu(111) for $m=2$ at lower fluences [193]. The mPP and $(m+1)$PP ATP signals can be produced by rectification of components of the induced polarization into photoelectron currents at the m and $(m+1)$ final state energies. They can also be thought of as a consequence of the same Floquet engineering process [194], where the applied $\hbar\omega_l$ field generates a Floquet ladder of quasi energy states (to be discussed in Chapter 6), which project SS electrons to $m\hbar\omega_l+E_{SS}$ and $(m+1)\hbar\omega_l+E_{SS}$ energies, where E_{SS} is the SS state binding energy. In a nonresonant process, these states must decay nearly instantaneously, unless they are able to undergo dipole transitions or scatter from the virtual Floquet state into a real state, through a process that ultimately conserves energy and momentum. The Floquet states at the $m\hbar\omega_l+E_{SS}$ and $(m+1)\hbar\omega_l+E_{SS}$ energies which are resonant with the photoemission continuum can decay into free electron vacuum states, where they are detected as mPP or ATP emission [43, 88].

My data show that the $(m+1)$PP ATP signals being the rectification of $(m+1)\omega_l$ coherent polarization field is a more probable scenario than the m-photon final state absorbing an additional

photon before departing from the surface. Of course, in a 5-photon process there are many other excitation pathways to reach the final state, but only the rectification of the (m+1) polarization would produce the observed FT amplitude slopes n/5 in Figure 5.8(b). That the ATP photoelectron is generated preferentially by rectification of (m+1) polarization can explain why the intensities of SS and IP1 state are reversed between the mPP and ATP orders in Figure 5.5(b). Whereas the ATP signal from the SS state results from rectification of the (m+1) polarization, that for the IP1 state first populates the intermediate state by the rectification of the $3\omega_l$ polarization followed by rectification of the $2\omega_l$ polarization to generate the ATP signal. Because susceptibilities are time-dependent [192], photoemitting an electron of the same order is probably less efficient by a cascaded process of lower order coherent responses than the direct higher order process. Although both are driven by an intense electric field, the ATP processes reported here should be contrasted with the nonperturbative regime, where it involves the field-induced re-collision of electrons with their atomic cores [195, 196]. We again emphasize that under our experimental conditions, we observe no spectroscopic evidence of field-induced nonperturbative dynamics.

5.4 Parametric Polarization Beating in *sp*-Band Excitation Dynamics

I have discussed the coherent 2PP-4PP and ATP excitation dynamics of the SS state from Ag(111) surfaces. In this section, I will discuss the excitation dynamics of the other prominent feature in the spectra, the U_{sp}←L_{sp} bulk-band transition. This transition has been mentioned in Chapter 4 and previous sections in this chapter and is summarized in Figure 5.10.

Figure 5.10 shows energy and $k_{\|}$-momentum resolved 2PP and 4PP spectra as excited with 3.07 eV and 1.52 eV photons, respectively. The corresponding $k_{\perp}$-resolved excitation diagram in

ΓL direction is shown in Figure 5.10(d). The photon energies differ approximately by a factor of two, so the photoemission spectral features can be expected at the same final state energy, however being excited by either 2- or 4-photons. Specifically, the 2PP spectrum has contributions from the resonant 2-photon U_{sp}←L_{sp} *sp*-band transition, and the non-resonant 2PP of the SS state. The Rydberg-like series of IP states is not prominent in 2PP, as the photon energy is far off-resonant from the IP1←SS resonance and thus IP1 state population is negligible. In 4PP, the SS state is observed at approximately the same final state energy with the same $k_{||}$-dispersion as in 2PP. In addition, the IP1 and IP2 states are detected in 4PP with $\hbar\omega_l$ = 1.52 eV excitation. The IP2 is excited near-resonantly by three photons from SS state leading to its intensity enhancement for the occupied $k_{||}$-range of the SS, which can be rationalized with its origin from the occupied part of the SS state. The nonresonantly excited IP1 state, however, is much broader than the occupied $k_{||}$-range of the SS state, suggesting that either energy conserving processes cause its population to produce a broad $k_{||}$ distribution, or it is populated by the L_{sp} band, where the three-photon transition from L_{sp} to IP1 is feasible above $\hbar\omega_l$ ~1.4 eV from the perspective of their energy positions in the band structure.

The appearance in 2- and 4-photon photoexcitation of the *sp*-transition is drastically different. In 2PP, the *sp*-transition spans the complete $k_{||}$-range, whereas in 4PP, it is strongly limited in $k_{||}$. In addition, the final state energy is slightly different in 2- and 4-photon photoexcitation ($\Delta E_f \approx 0.1$ eV). Note that this 0.1 eV energy difference is significant if we compare it with the energy positions of SS state in 2PP and 4PP which are almost the same. Having established (but no explained) these differences in energy and momentum space in 2PP and 4PP, I study the coherent dynamics of the *sp*-transition using ITR-4PP and find unexpected polarization

beating dynamics in the time- and frequency-domains. Note that the 4PP spectrum has a large secondary electron background signal just above the E_{vac}.

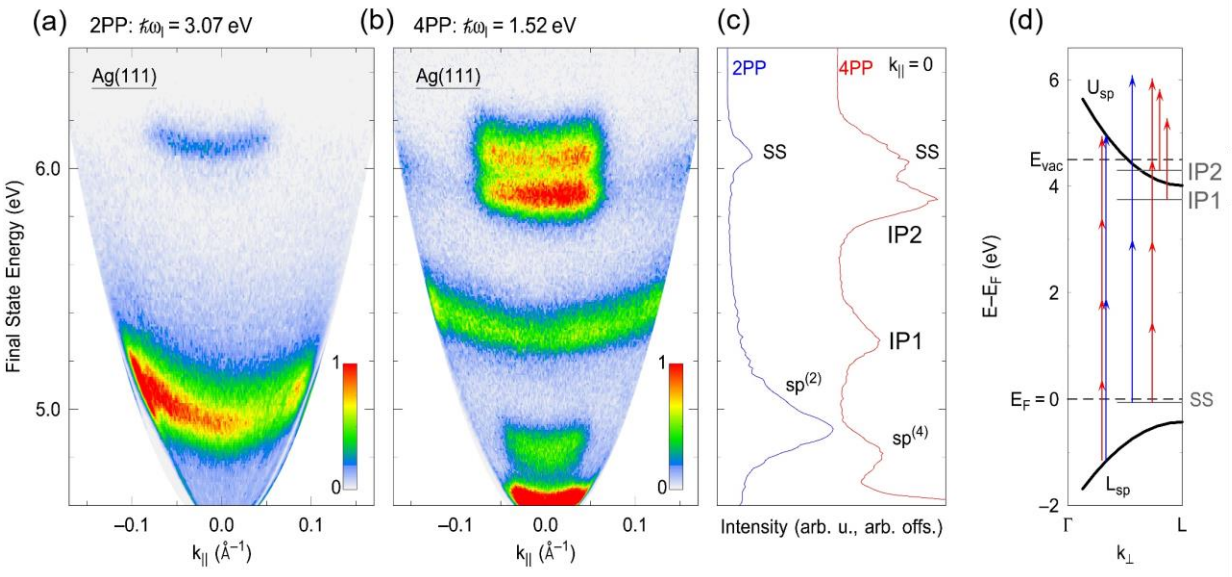

Figure 5.10 Energy- and $k_{||}$-resolved 2PP and 4PP spectra of Ag(111) at (a) $\hbar\omega_l$ = 3.07 eV and (b) $\hbar\omega_l$ = 1.52 eV, respectively; spectral elements are labelled in the line profiles taken through the spectra at $k_{||}$ = 0 Å^{-1} and shown in (c). Excitation diagram of SS, IP states and *sp*-band is drawn in (d), with blue arrows representing 3.07 eV photons and red arrows representing 1.52 eV photons.

The ITR-mPP scan of the pristine Ag(111) surface shown in Figure 5.11 is excited with $\hbar\omega_l$ = 1.56 eV. The spectrum is composed of the SS and IP1 state as well as the *sp*-transition excited in 4PP, $sp^{(4)}$, and 5PP, $sp^{(5)}$. Here, we use the I2PC of the SS state as an approximation of the fourth-order autocorrelation of the laser pulses [Figure 5.11(b)]. Compared with the I2PC of the SS state, in 4PP, as well as in 5PP, a complex beating structure is superposed on the Gaussian shape signal induced by external fields that modulates the I2PC of the *sp*-transition. Interference fringes are suppressed and enhanced with a sub-periods of 13 fs [$sp^{(4)}$] and 16.5 fs [$sp^{(5)}$]. By inspection of the ITR-mPP fringes of Figure 5.11(a) and the corresponding 2D-FT spectrum in

Figure 5.12, tilted interference fringes can be identified in the complex structures, which indicate coherence of the excitation process [43]. Thus, a coherent polarization beating of the *sp*-transition is observed. The polarization of the charge carriers is modulated by beating of frequency components on a time scale, which is faster than the autocorrelation of the laser pulses, thus seemingly violating the energy-time uncertainty.

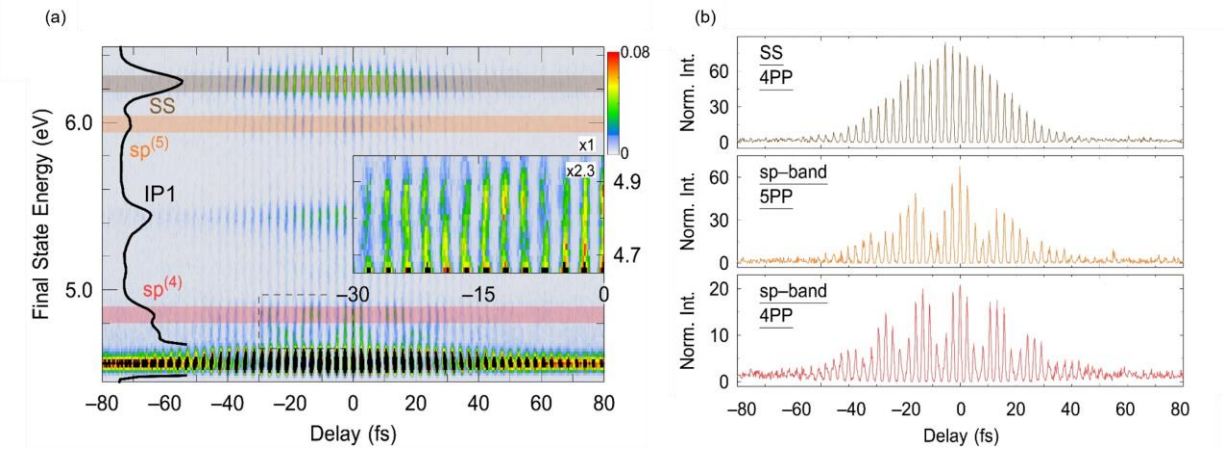

Figure 5.11 ITR-mPP interferogram of the pristine Ag(111) surface excited with $\hbar\omega_l$ = 1.56 eV is shown in (a). Spectral elements are labelled in the line profile cut at τ=0 fs as black solid lines. The enlarged inset shows the *sp*$^{(4)}$ transition in 4.65-4.95 eV range. (b) I2PC cross sections at final state energies of SS state, *sp*$^{(5)}$ transition, and *sp*$^{(4)}$ transition shaded in the interferogram.

To clarify the origin of the polarization beating, we again Fourier transform the ITR-mPP data to generate 2D-FT photoelectron spectra shown in Figure 5.12. As I have discussed, FT amplitude is expected at the driving laser frequency $1\omega_l$ and its harmonics ($n\omega_l$, $n \leq m$), which is clearly observed for the SS and IP1 states, *sp*$^{(4)}$ and *sp*$^{(5)}$ transitions in Figure 5.12(a). However, for both *sp*-transitions, we find satellite peaks below, $n\omega_l^-$, and above, $n\omega_l^+$, the harmonics of the driving laser frequency $n\omega_l$ [cf. line profiles in Figure 5.12(a)]. These additional frequencies cause

the polarization beating in the time domain. Most remarkably, the FT amplitudes detected at the $n\omega_l^-$ and $n\omega_l^+$ frequencies lie outside the spectral width of the broadband femtosecond laser pulses, and thus, these coherent polarization responses cannot be excited within the bandwidth of the excitation pulse. Therefore, these responses cannot be excited directly by the optical field, but rather have to be generated in a nonlinear light-matter interaction process. The underlying process is coherent, as shown by the tilted interference fringes in the time-domain, and more clearly, by the tilted FT amplitude in Figure 5.12(b). The responses outside of the laser bandwidth cannot build up from noise, because they would not maintain the phase correlation for every pump-probe pulse pair.

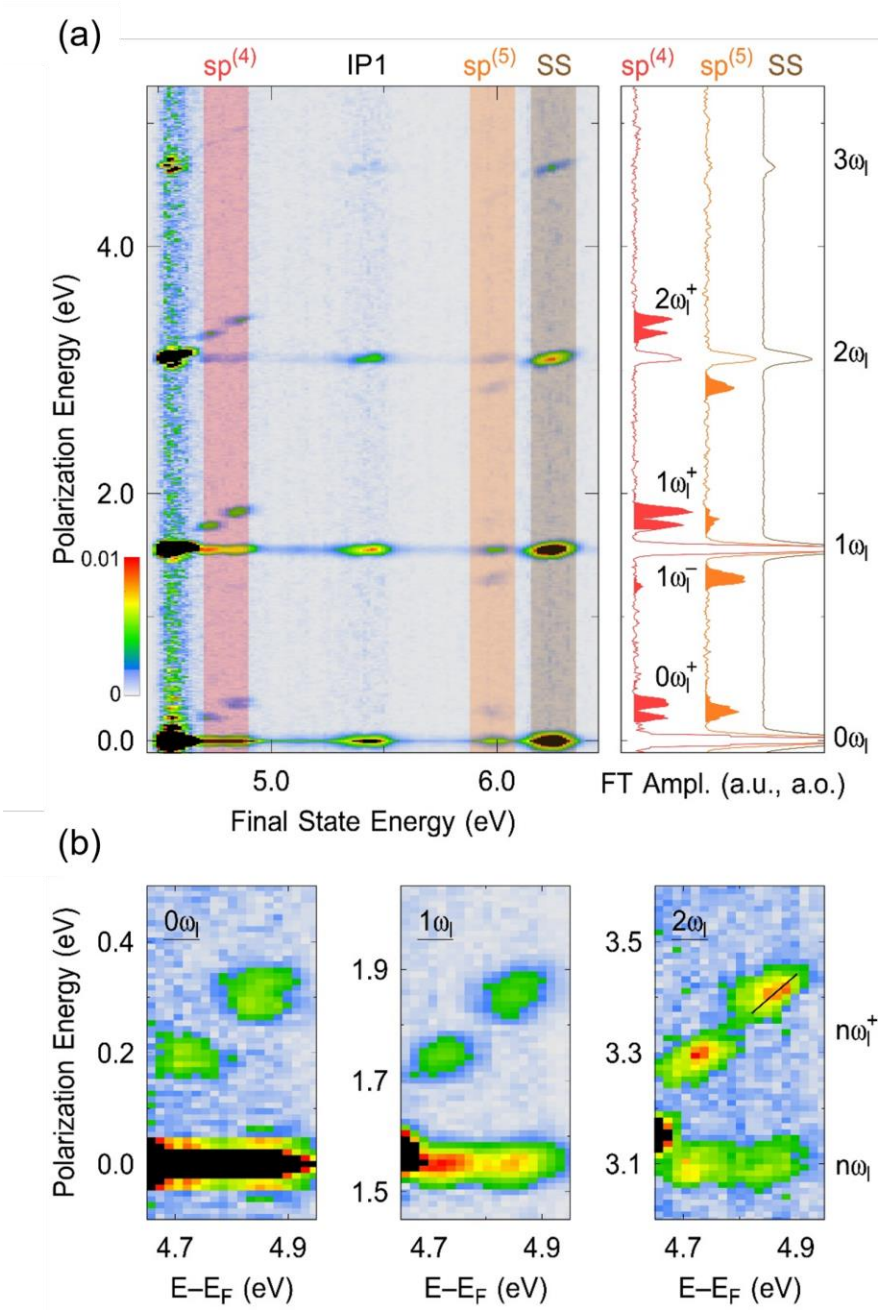

Figure 5.12 2D-FT photoelectron spectra showing the FT signal of the data in Figure 5.11 are plotted in (a). Cross sections at final state energies of $sp^{(4)}$ transition, $sp^{(5)}$ transition, and SS state (color shaded) are plotted in the right panel. (b) Enlarged 2D-FT photoelectron spectra components $0\omega_I$, $1\omega_I$, and $2\omega_I$ for $sp^{(4)}$ transition. Tilting of both the main harmonics peaks $n\omega_I$ and the plus satellite peaks $n\omega_I^+$ indicates these processes being coherent.

I performed photon energy dependent ITR-mPP experiments in the $\hbar\omega_l$ =1.40-1.60 eV range, which is limited by the laser power on the lower end (1.40 eV) and by the onset of strong 3PP SS state signal around the work function on the higher end (1.60 eV). Figure 5.13(a) shows cross sections through the 2D-FT photoelectron spectra taken at the final state energy of the IP1 state and the $sp^{(4)}$-transition. For IP1 state, linear dependence of the $n\omega_l$-harmonic polarization energy on the photon energy is expected [Figure 5.13(a) left panel], and in accordance, a slope of n is extracted for the $n\omega_l$-harmonic. For the $sp^{(4)}$-transition shown in Figure 5.13(a) right panel, the harmonic frequencies behave analogously to the case of IP1 state. However, the satellite frequencies shift with respect to the harmonic frequencies, thus, if the $n\omega_l$-harmonic shifts with the slope of n, the $n\omega_l^+$- and $n\omega^-$-harmonics shift with slopes of (n-1) and (n+1), respectively [Figure 5.13(b)]. Based on this analysis, three major observations can be made: (i) Independent on photon energy, the $sp^{(4)}$-transition is always polarized at the nearly constant frequency of the $1\omega_l^+$-feature with $1\hbar\omega_l^+ \approx 1.9$ eV. (ii) The linear regressions of the satellite and the harmonic frequencies will intersect for $\hbar\omega_l \approx 1.9$ eV ($\hbar\omega_l = 1\hbar\omega_l^{\pm}$). We note that, as discussed in Chapter 3.3, 1.9 eV is a special frequency for silver where transient exciton features emerge before the formation of IP1 state in a two-photon IP1←SS resonance [19]. Increased non-linear response of Ag(111) is also reported exactly for $\hbar\omega_l = 1.9$ eV [91], as the bulk plasmon frequency, $\hbar\omega_p \approx 3.8$ eV, is effectively excited in a second-order non-linear process. (iii) The satellite polarization frequencies sum up to two times of the driving polarization frequency, i.e., $n\hbar\omega_l^+ + n\hbar\omega_l^- = 2\times n\hbar\omega_l$.

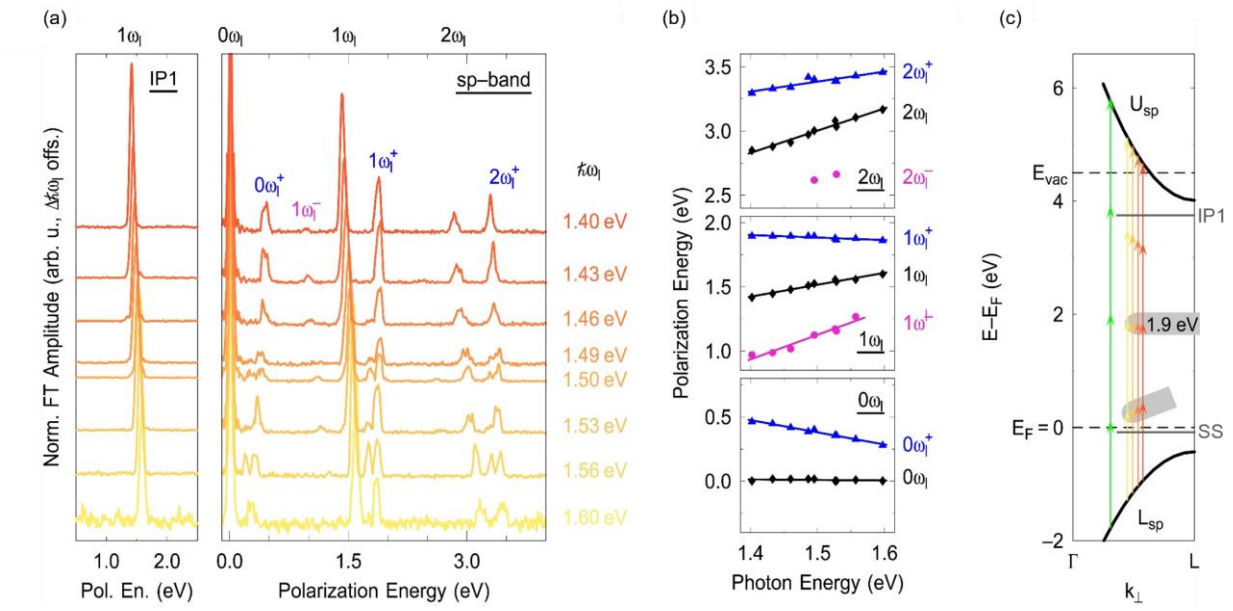

Figure 5.13 Photon energy dependent analysis of the $sp^{(4)}$ transition in 2D-FT spectra. (a) Line profiles of Figure 5.12(a) cut at specific final state energies in a series of photon energy dependent 2D-FT photoelectron spectra ($\hbar\omega_l$ =1.40-1.60 eV). Cross sections are taken at IP1 state (left; only show the $1\omega_l$ harmnoic peak) and $sp^{(4)}$ band final state energies (right). (b) Photon energy dependent FT peak positions for the main harmonic peaks $n\omega_l$ and the satellite polarization peaks $n\omega_l^{\pm}$. (c) Schematic excitation diagram of the 4PP *sp*-transitions in the single-particle band structure of Ag along the ΓL ($k_\perp$) direction ($k_\parallel$ = 0 Å^{-1}). The green arrows indicate photon energy of 1.9 eV, where one photon excitation form L_{sp} terminates at E_F. Arrows with yellow to orange colors indicate seleted photon energies in (a). E-E_F (1-photon) energy decreases with increasing of photon energy for 1-photon absorption from L_{sp} (tilted grey box), but 2-photon absorption excites electrons, independent of the photon energy, to E-E_F ≈ 1.9 eV (grey box).

In Figure 5.13 (c), we try to correlate the satellite frequencies to the single-particle band structure of Ag(111) by plotting the $k_\perp$-resolved excitation diagram in ΓL direction at $k_\parallel$ = 0 Å^{-1} [93]; the $sp^{(4)}$-transition is indicated for several photon energies by arrows (orange to yellow). In a vertical ($k_\perp$-conversing) resonant $sp^{(4)}$-transition, 2-photon absorption excites electrons, independent of the photon energy, to a constant energy E-E_F ≈ 1.9 eV [grey box in Figure 5.13

(c)]. By contrast, the energy position E-E_F for 1-photon interaction decreases with increasing photon energy [tilted grey box in Figure 5.13 (c)]. Remarkably, if the experiment were to be done with $\hbar\omega_l$ = 1.9 eV photons (green arrows), i.e., for $\hbar\omega_l = 1\hbar\omega_l^{\pm}$, 1-photon absorption would lift L_{sp} electrons to E_F. Actually, for a given $\hbar\omega_l$ in a $k_\perp$-conserving process excited from L_{sp}, E_F is the benchmark energy, which defines the polarization energies of the satellites. Specifically, as $1\hbar\omega_l^-$ describes the difference between the occupied L_{sp}-band and E_F, $1\hbar\omega_l^+$ defines the energy of E_{Lsp}+ $2\hbar\omega_l$ = 1.9 eV above E_F, where E_{Lsp} is the binding energy of L_{sp}. I thus surmise that E_F and E_{Lsp}+ $2\hbar\omega_l$ =1.9 eV are crucial for the beating mechanism of the $sp^{(4)}$-transition.

I emphasize, that the relaxation/excitation process to E_F has to be a complex many-body process, as in the single-particle band structure of silver, no states are expected at E_F for $k_\parallel$ = 0 Å^{-1} [26, 58], but, presumably similar as in the case of single-particle electron emission by the decay of bulk plasmon fields [36, 37, 93], electrons may relax in a multi-electron energy- and momentum-conserving process. I strengthen this argument, by highlighting that bulk plasmons, which are effectively excited with $\hbar\omega_l$ = 1.9 eV [91], most likely contribute to this excitation process. Thus, the $n\hbar\omega_l^+$-satellites might be understood as local fields created when charge-carriers excited by the pump-field decay to E_F under emission of the field. The $n\hbar\omega_l^-$-satellites, in contrast, might be seen as charge carriers excited from the L_{sp} band to E_F, but without firm reasoning.

I also need to stress the possible involvement of the SS state in this process. As mentioned before, in 2PP, the *sp*-transition spans the complete $k_\parallel$-range, while in 4PP, it is strongly limited in $k_\parallel$, which is comparable to that of the SS state. In addition, its final state energy is ~0.1 eV lower in 4PP than in 2PP, and considering that SS state of Ag(111) lies 0.063 eV below E_F, it could be that the SS state is somehow coupled to this polarization transition and 'shift' the final state energy. Since SS state is the only discrete surface state near the E_F, it can also serve as a benchmark state

to carry on single-particle transitions and compensate for the fact that there are no states at E_F at $k_{\|} = 0$ Å^{-1} to enable single-particle transitions. Moreover, this $sp^{(4)}$-transition strongly depends on dispersion of the laser pulse and can only be resolved with the shortest pulse with broadest bandwidth. Deviation from the best dispersion will 'shift' the energy position of the *sp*-band signal towards and 'merge' into the SS state signal, which we cannot explain at present. Regardless of various arguments, whether or how the SS state gets involved in and modulate the bulk $sp^{(4)}$-transition is still unknown and needs further reasoning.

Nevertheless, in the following, I try to propose a possible mechanism for 4PP of the $sp^{(4)}$ transition and the generation of the satellite frequencies $n\hbar\omega_l^{\pm}$. We base the mechanism on the concept of parametric amplification, which is a common second order nonlinear process in crystalline media [197]. As shown in Figure 5.14, we assume the initial 4-photon excitation to take place for $k_{\|} = 0$ Å^{-1} and $k_{\perp}$ is selected based on the photon energy used for resonant excitation of the $sp^{(4)}$ transition. The surface projected single-particle band structure is characterized by a band gap at $k_{\|} = 0$ Å^{-1} extending from the L_{sp}- to the U_{sp} -band [26], no electrons are expected at E_F because of the projected band gap. In an energy- and momentum-conserving process, electrons being excited by 2-photons can decay to E_F while electrons from the L_{sp}-band are excited to E_F. The SS state, close to the E_F, may participate in the transition. This process is similar to parametric amplification as observed in non-linear media, where in this picture, the $1\hbar\omega_l^+$ and $1\hbar\omega_l^-$ frequencies could be considered, in analogy, as signal and idler, respectively. We note again that this argumentation is incomplete and needs further consideration.

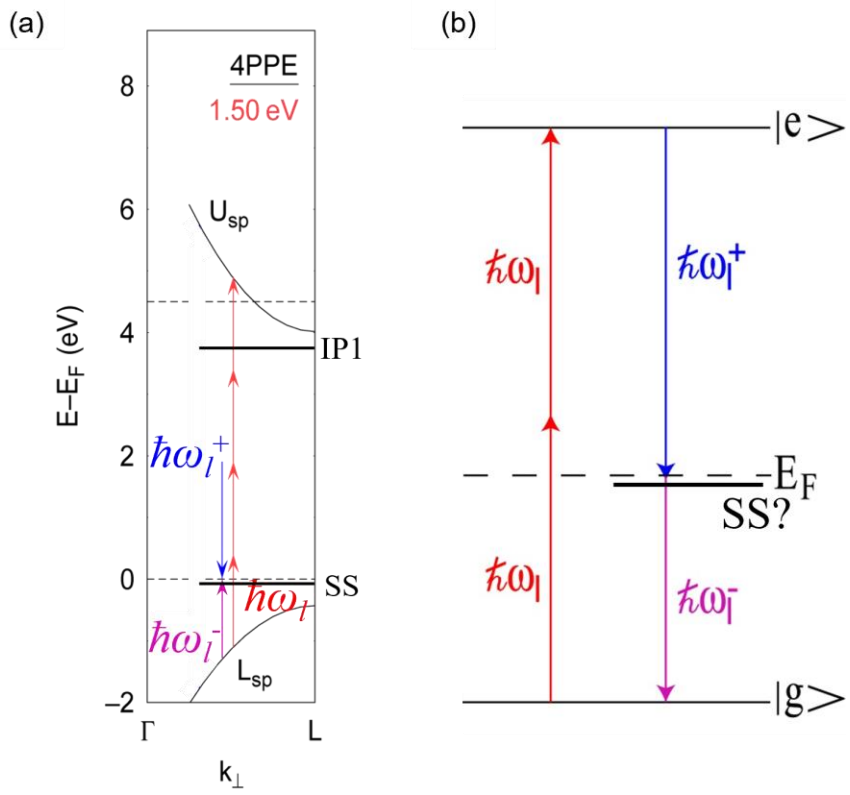

Figure 5.14 Proposed excitation mechanism of the $sp^{(4)}$ transition. (a) Excitation diagram for $sp^{(4)}$ transition in the single-particle band structure of Ag along the Γ-L ($k_\perp$) direction. (b) Proposed parametric amlication schematic for this transition.

6.0 Coherent Resonant Excitation Dynamics on Cu(111) Surfaces

After discussing the non-resonant mPP dynamics of SS states, in this chapter, I tune the photon energy to realize a 3-photon resonant transition between the SS and IP1 state to study how the optical fields affect the resonant excitation dynamics on Cu(111) surface. From the dependence of spectral shapes on the applied field strength, I found spectroscopic signatures of optical dressing of surface states. I attribute the dressing to the generation of Floquet replicas of surface states due to periodicity of the light field and Autler-Townes splitting (ATS) due to resonant excitation conditions. I demonstrate that, in a solid-state system, entanglement between optical fields and *k*-dispersions can modify and control the quasiparticle properties of material, such as the band energies and effective masses, and consequently, all electronic properties that depend on them, on the sub-optical cycle time scale. The content in this chapter is based on a publication in Nature Communications [198] and preliminary results at the current stage of analysis.

6.1 Introduction to Dressed States

Space-periodic arrangement of lattice ions in crystalline solids defines the *k*-momentum dispersion of electronic quasiparticle bands. Light can interrogate such bands by stimulating electric dipole transitions. When an optical field interaction with time periodicity exceeds all other perturbations, particularly at an electronic resonance, it can also modify the system eigenstates, causing a field dependent mixing, which is usually referred to as dressing [199-204]. Dressed states can be explained as a combination of the Floquet engineering and AC Stark effect, which causes

the ATS. ATS is a well-known concept in the atomic spectroscopy, but has not been much implemented in the solid state, and not in nonlinear photoemission spectroscopy. Optical dressing of the band gap of GaAs has been achieved by recording optical third harmonic generation with 5 fs laser pulse band gap excitation at ~10^9 V/m field strength [203, 205, 206]. Under such intensities, it is possible to induce carrier-wave Rabi flopping in solid state materials, as will be explained further.

To describe optical dressing in solid state, I consider a model system consisting of two eigenstates, the SS and IP1 [Figure 6.1(a)]. In analogy to the Bloch bands which has periodic *k*-momentum due to space periodic lattice potentials, time periodicity of the light field $H(t)=H(t+T)$ with electric field strength $\mathcal{E}$, and frequency $\omega_l=2\pi/T$ will generate a series of Floquet states, which form a ladder of states at energies given by integer multiples of the photon energy above and below the preexisting Bloch state $E=E\pm n\hbar\omega_l$ (*n*, integer), as shown in Figure 6.1(b) [194, 207]. While Floquet physics is usually applied to illumination with continuous monochromatic light, the same physics applies to ultrashort pulses, which consists of limited number of optical cycles [208]. Thus, the high peak intensity of ultrashort laser pulses can be used to investigate the Floquet physics-induced nonlinear interactions in solid state excitation [209]. To separate two limiting excitation regimes caused by the strong field strength, Keldysh parameter $\gamma = \sqrt{\frac{\Phi}{2U_p}}$ is introduced, where the ponderomotive energy $U_p = \frac{e^2\mathcal{E}^2}{4m_e\omega_l^2}$ [210]. The excitation is considered in the multiphoton regime when $\gamma \gg 1$ and in the tunnelling (or strong field) regime when $\gamma \ll 1$. For my data taken with the highest field strength (shown in Chapter 6.3), which is estimated to be on the order of 10^9 V/m, $\gamma\sim10$ is still >1, which indicates that my data is still in the perturbative regime but close to the limit.

Under perturbative conditions, light fields $\mathcal{E}(\tau)$ can excite multi-quantum transitions from dispersive Floquet-Bloch bands that are defined by the crystal structure, with their eigenstates specified by their momentum *k*. An intense $\mathcal{E}(\tau)$-field, however, can perturb the system by causing Rabi flopping to occur between the optically coupled bands at frequencies $\widetilde{\Omega}_R$ that can become comparable to that of the excitation field ω_l [203]. This is called Rabi flopping, because the state population is transferred between the ground and excited states on time scale of the optical cycle. For resonant or near resonant excitation, the Floquet replicas of unperturbed SS and IP1 states can become degenerate causing the Rabi oscillation to become pronounced, and the eigenstates of the system to be perturbed and experience mixing. The optical field will shift the eigenstates through the AC Stark effect, causing the band repulsion. The electronic bands are said to be dressed by this interaction [Figure 6.1(c)] [199, 207]. The optical dressing is thus marked by ATS of solid state bands into new eigenstates $E_{\pm}$ [211]. The band dressing is described by the Hamiltonian of the interacting system, where SS and IP1 states are the unperturbed Bloch eigenstates that are defined by the crystalline periodicity

$$H_0 = \begin{pmatrix} E_{SS}(k_{||}) & 0 \\ 0 & E_{IP1}(k_{||}) \end{pmatrix} \tag{6.1}$$

The eigenstates of this Hamiltonian are perturbed by the generalized Rabi frequency

$$H' = \hbar\widetilde{\Omega}_R(\tau, k) = \hbar\sqrt{\Omega_R^2(\tau) + \Delta^2(k)} \tag{6.2}$$

where $\hbar\Omega_R(\tau) = \mu_{\text{eff}}\mathcal{E}^n(\tau)$ is the Rabi frequency of an *n*-photon transition [212], and $\hbar\Delta(k)$ is the *k*-dependent detuning of Bloch bands. In the case of surface states, they disperse in the surface parallel plane such that *k* dispersion is $k_{||}$. Moreover, we assume the dipole moment, μ_{eff}, to be independent of *k* based on approximately symmetric 4PP intensity distributions (with respect to + and – parallel momentum, $k_{||}$), and $k_{||}$ independent linear photoemission spectra of SS [213]. Note,

that in an *n*-photon interaction, the perturbation depends on the *n*-th power of the applied optical field, and therefore in a nonlinear process is extremely sensitive to the relative phase between pump and probe optical fields.

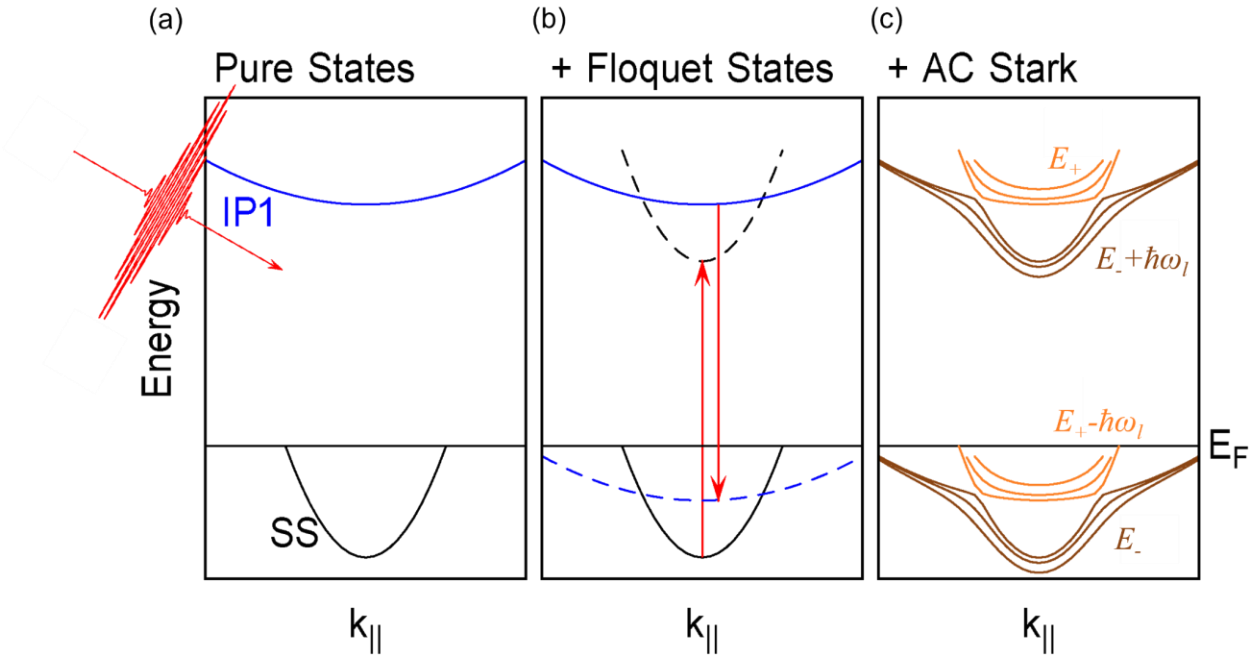

Figure 6.1 Schematics of formation of dressed electronic bands. A light pulse with time periodicity interacting with (a) a model two-level system consisting of SS and IP1 states generates (b) the Floquet replicas of these states (dashed lines) located at multiples of photon energy above/below energy positions of the unperturbed states. (c) When the Floquet replicas cross the unperturbed bands at certain $k_{||}$, ATS (or AC-Stark effect) happens and the avoided crossing of bands in (b) causes repulsion such that they form dressed bands (E_+, E_-; orange and brown lines). The splitting between dressed states depends on the light field strength, which varies through each optical cycle.

The ground and excited surface electronic bands of several metals, and in particular, the (111) surfaces of noble metal, exist in projected band gaps where they are decoupled from stronger bulk interactions [Figure 6.2(a)] [3]. This makes them inviting targets for probing their quantum

optics by ultrafast mPP spectroscopy and many-body theory [3, 43, 68, 70, 163, 214]. Contrary to the optical dressing of GaAs, the surface states are two dimensional, so one does not need to characterize the dressing of 3D bulk bands, where the surface normal dispersion would further complicate the measurement and simulation. Thus, I study the $k_{||}$-dispersion dependent optical dressing with ~20 fs infrared laser pulses by exciting a three-photon resonant transition between SS and IP1 states of Cu(111) surfaces. Further one photon absorption from the IP1 state (a total 4PP process) thus probes the coherent field interaction by projecting the dressed bands into the photoemission continuum. In an ITR-mPP measurement, advancing the delay (phase) between pump and probe pulses in $\Delta\tau$~100 as steps defines the total optical fields with attosecond precision. The schematic of the Floquet states and ATS is shown in Figure 6.2(a) and (b), respectively. In Figure 6.2(a), Floquet replicas of SS and IP1 states are generated at $k_{||}$=0 Å^{-1} by the laser field (dash-dotted lines), and they are detected in photoemission as Floquet states that are excited above the vacuum level. In Figure 6.2(b), due to the resonant excitation conditions at $k_{||}$=0 Å^{-1}, Floquet replicas modified by the AC Stark effect under intense laser fields are expected to show evidence of Rabi flopping and band dressing in photoelectron spectra. The splitting between dressed bands will increase with increasing optical field strength which is realized by tuning the focal distance of the laser from the sample. Higher order photoemission signal (5PP/ATP) can also be detected, just as in the nonresonant cases that are described in the previous chapters. Moreover, due to the different band dispersions of SS and IP1 which define their band masses (m_{SS}, m_{IP1}), the $k_{||}$-dependent detuning from resonance $\hbar\Delta(k_{||}) = \frac{\hbar^2}{2}(m_{\mathrm{SS}}^{-1} - m_{\mathrm{IP1}}^{-1})k_{||}^2$ will affect the dressing [Figure 6.2(a)] and be encoded in the data.

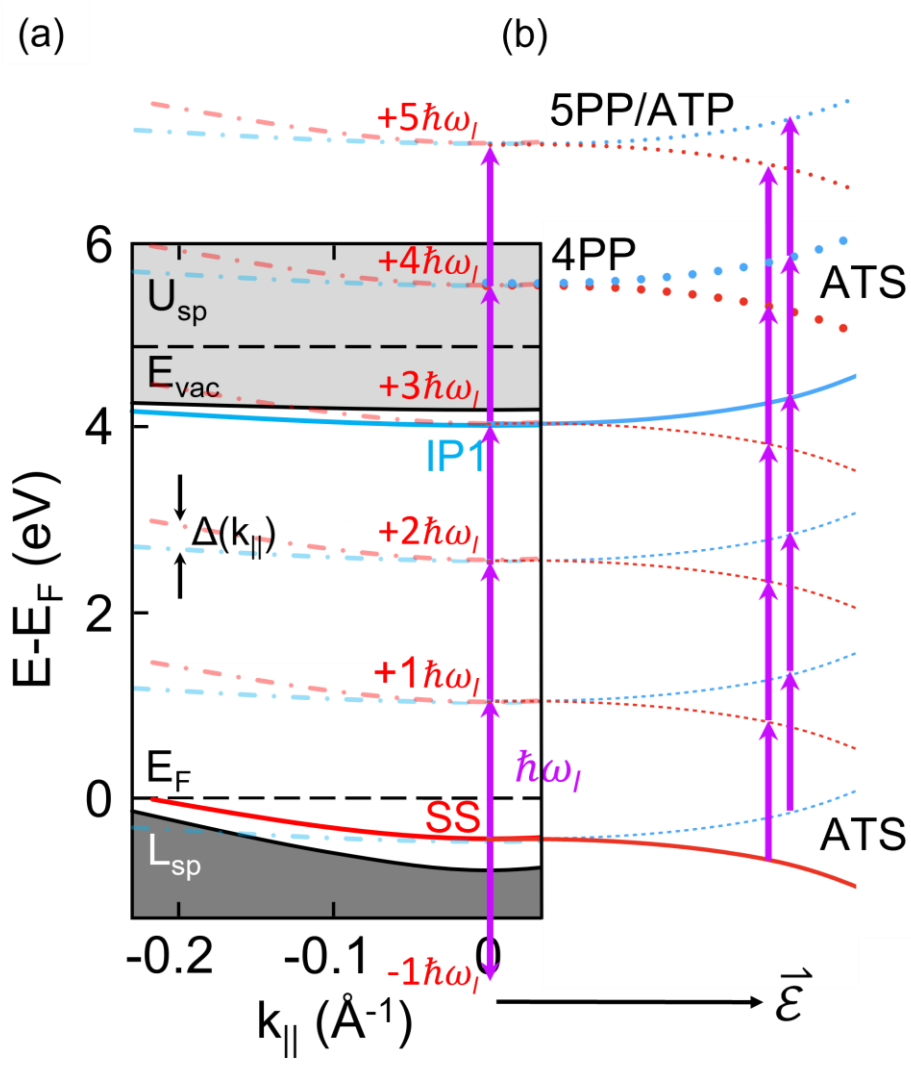

Figure 6.2 Schematics of the mPP dressed states on Cu(111) surfaces. (a) A series of Floquet replicas (dash-dotted red and blue lines) of the SS and IP1 state (solid red and blue lines) shown in the surface normal projected Cu(111) band structure. The SS and IP1 states exist in the surface projected band gap between the L_{sp} and U_{sp} bands (grey shading). Due to different effective masses of the two states, the photon energy which is a three-photon resonance of two states at $\bar{\Gamma}$ point becomes near-resonant excitation at large $k_{||}$, with $k_{||}$ dependent detuning $\Delta(k_{||})$. (b) Diagram of electric field strength dependent dressed states at $k_{||}$=0 Å^{-1}, where SS and IP1 are in a three-photon resonance. Due to ATS, the degenerate Floquet replicas of SS and IP1 (dashed red and blue lines) repel each other, and the splitting increases with increasing electric field strength. Photoemission from these dressed states shows signature of Autler-Townes doublet (AT doublet) structure plotted as dotted lines in 4PP.

6.2 Power Dependent Optical Dressing in Resonant IP1←SS Excitations

The ITR-mPP result is shown in Figure 6.3. The $\mathcal{E}(\tau)$ field with $\hbar\omega_l$=1.54 eV excites the three-photon resonant transition from the SS to IP1 band of Cu(111) at $k_{\|}$ = 0 Å^{-1} [Figure 6.3(b)]. The time-integrated 4PP spectrum in Figure 6.3(c) confirms the SS and IP1 resonance [70, 93]; such optical phase-integrated measurement, however, obscures their dressing, which is encoded in the phase resolved $E_f(k_{\|},\tau)$ data [Figure 6.3(a)]. The phase resolved data reports the response due to the optical field strength at a particular instant, rather than an integrated result over the interaction time. To reveal dressing, we first extract the $\mathcal{E}(\tau)$-dependent 4PP intensity for $k_{\|}$ = 0 Å^{-1} ($\hbar\Delta = 0$ eV) by plotting the 2D $E_f(\tau)$ interferogram, and its 1D I2PC showing the photoelectron counts vs. τ at E_f of the IP1←SS resonance [Figure 6.3(c)]. If the optical field $\mathcal{E}(\tau)$ with approximately a Gaussian time profile generated the 4PP signal by only exciting dipole transitions, the I2PC trace in Figure 6.3(c) would follow $\mathcal{E}^8(\tau)$ dependence, and therefore, be sharply peaked at τ=0 fs [19, 43], but instead, it has a local minimum and retarded maxima at $\tau \approx \pm 15$ fs, which portend the optical field dressing.

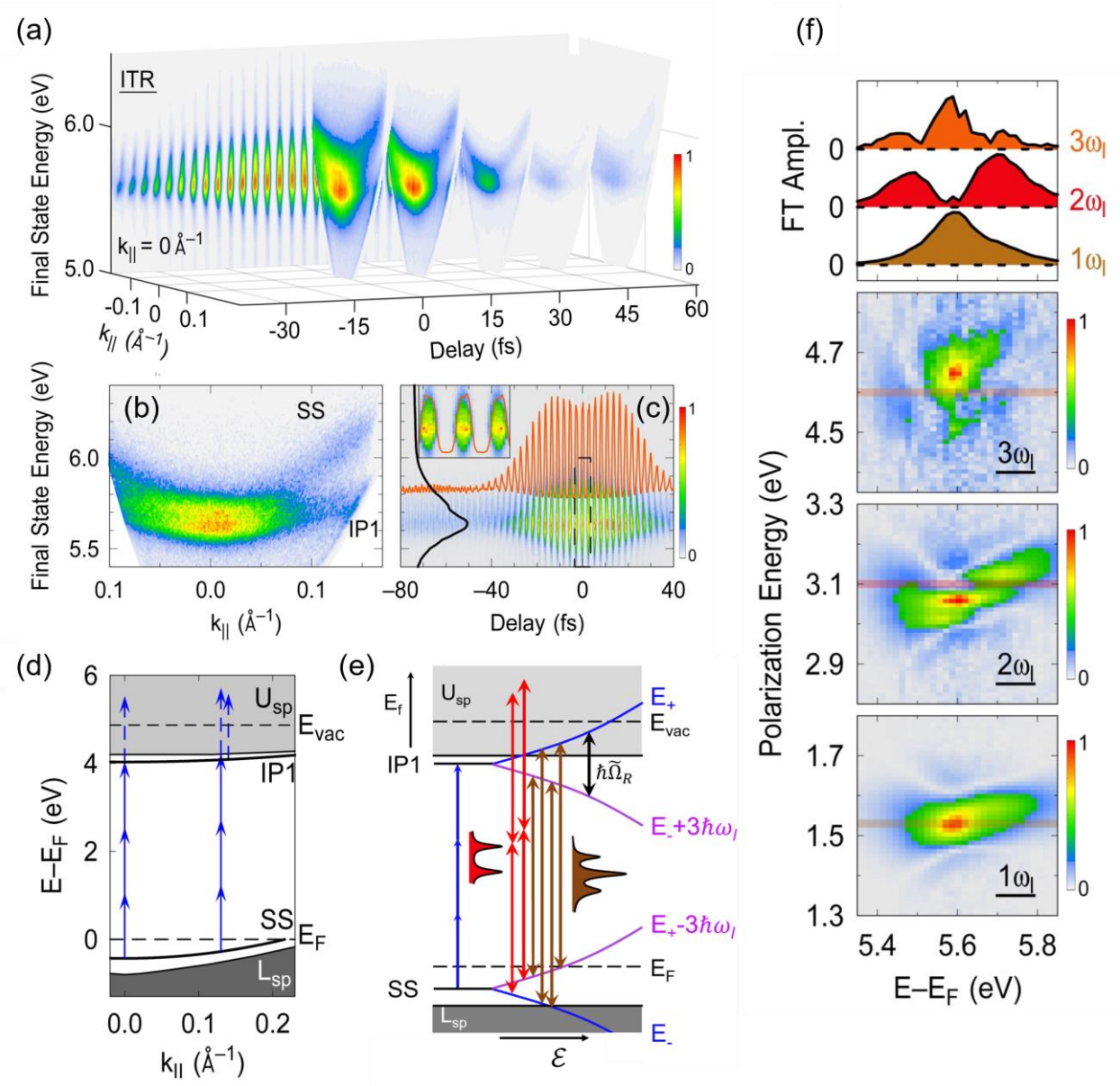

Figure 6.3 Coherent photoelectron spectroscopy of optical dressing. (a) 3D ITR-4PP data of the three-photon resonant IP1←SS transition ($\hbar\omega_l$=1.54 eV). Each frame records the photoelectron signal counts vs. E_f, and $k_{||}$ in ~100 as steps. Sample frames at different delays are shown in 15 fs intervals. The back panel shows a cross section through the data for $k_{||}$=0 Å^{-1}. (b) Time integrated 4PP spectrum showing the SS and IP1 bands for resonant excitation at $k_{||}$=0 Å^{-1}. The excitation becomes near-resonant at large $k_{||}$. (c) Selection of data from (a) for $k_{||}$=0 Å^{-1} showing an $E_f(\tau)$-interferogram; the profiles show I2PC trace for E_f=5.6 eV (orange) and a 4PP spectrum for τ=0 fs (black); the inset expands the $E_f(\tau)$-data around τ=0 fs (the dashed box). (d) The unperturbed surface projected band structure of Cu(111). SS and IP1 states are coupled by the three-photon

resonant laser field (blue); the fourth photon induces the photoemission (dashed blue). (e) The schematic of optical dressing of the SS and IP1 bands which generates two pair of states. The optical dressing is revealed in AT doublets in the nonresonant coherent polarizations at $2\omega_l$ (red arrows) , and Mollow-triplet (MT) structures in the resonant coherent polarizations at $3\omega_l$ (brown arrows). (f) 2D-FT photoelectron spectra in linear- to cubic-order polarization; at the top, the profile of Fourier filtered E_f-spectra are plotted for the marked polarization energies (color shading).

The $E_f(k_{||},\tau)$-data, therefore, incorporates both the $\mathcal{E}(\tau)$-dependent band dressing and quantum excitation pathways, which are revealed by its Fourier analysis. FT of the 2D time-domain data in Figure 6.3(c) is shown in Figure 6.3(f) and resolves the induced polarization fields in the sample that oscillate at $n\omega_l$ frequencies to produce the 4PP signal [43]. Compared with the already discussed different polarization components of a non-resonant SS excitation in Chapter 5 Figure 5.3(a), we can see clear deviation in $n\omega_l$-components shapes from the elliptical spectral shapes and multi-peak structures [Figure 6.3(f)]. In Figure 6.4, we further inverse Fourier transform (IFT) each polarization components and present the 2D-Fourier filtered time-domain spectra of coherent polarizations oscillating at $2\omega_l$- and $3\omega_l$-frequencies, which reveal the dominant pathways for how these coherences contribute to the 4PP signal, and thereby reveal the dressing.

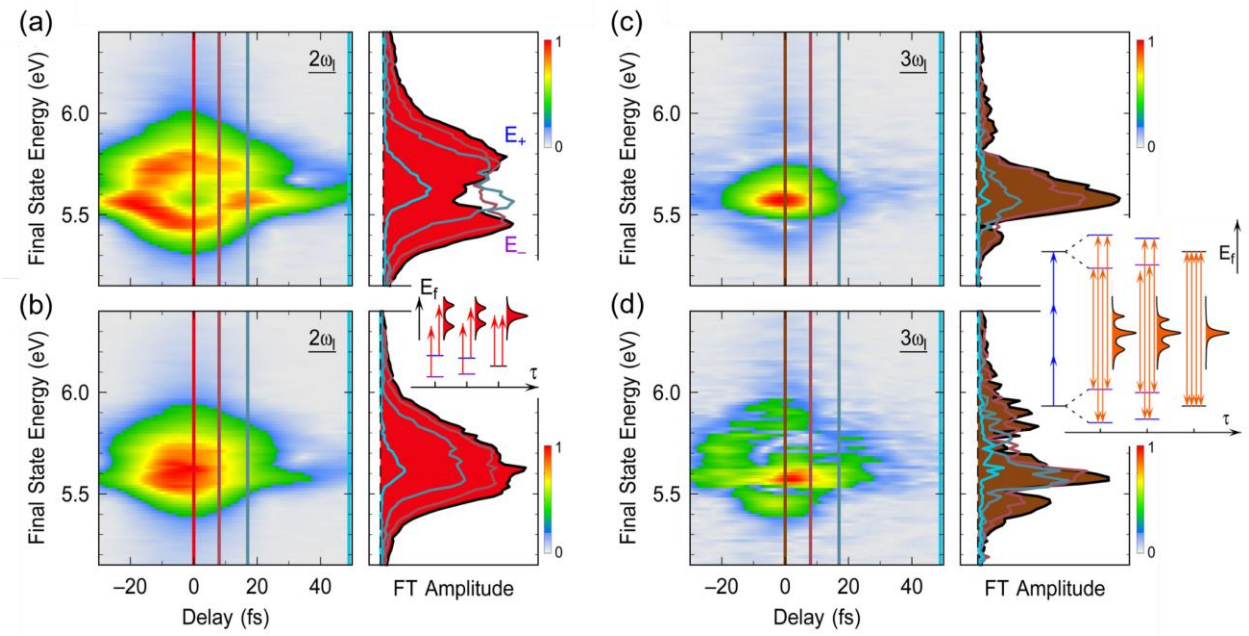

Figure 6.4 Femtosecond $\mathcal{E}(\tau)$ field dressing of the surface bands. IFT spectra of the (a, b) $2\omega_l$- and (c, d) $3\omega_l$-polarization responses at $k_{\parallel}$ = 0 Å^{-1} for excitation with high (top) and low (bottom) laser fluence. Laser fluence is tuned by changing the focal point distance of the laser beam with respect to the sample. At high fluence and τ=0 fs, in (a) and (c), the AT doublet and MT triplet structures are visible, respectively. As the instantaneous $\mathcal{E}(\tau)$ decreases with increasing τ, however, the dressed bands converge to undressed ones within ~15 fs (cf. inset). At low fluence, $\mathcal{E}(\tau)$ is sufficient to drive the 4PP process, but its dressing is minimal. Energy line profiles taken for selected delay points (color coded) are shown for each measurement in the right. The two insets show how the dressing depends on the instantaneous excitation fields as τ is increased.

The $2\omega_l$ and $3\omega_l$ IFT spectra show peak doubling and tripling, respectively, near τ=0 fs when the optical field amplitude is the largest (Figure 6.4). The $3\omega_l$-polarization represented by brown arrows in Figure 6.3(e) reports how the optical field dresses the resonant bands causing components at $3\omega_l$ and $3\omega_l \pm \widetilde{\Omega}_R$ frequencies to appear with ~1:2:1 intensity ratio. Such coherent polarizations produce MT structures in gas-phase optical spectra [211]. By contrast, the nonresonant $2\omega_l$-polarization, represented by red arrows in Figure 6.3(e), shows how the three-photon IP1⟵SS resonance dresses the interacting bands by revealing the AT doublet, when they are projected into

the E_f-continuum. The $2\omega_l$- and $3\omega_l$-spectra in Figure 6.4 thus reveal the coherent sub-femtosecond responses of the electronic bands to the dressing field. The $2\omega_l$-spectrum shows that when τ=0 fs and therefore, when $\mathcal{E}(\tau) = \mathcal{E}_{pump}(t) + \mathcal{E}_{probe}(t+\tau)$ is maximum, at resonance the AT doublet splitting is $\hbar\widetilde{\Omega}_R(\tau) \approx 0.3$ eV, but as $|\tau|$ increases to ~15 fs, the instantaneous $\mathcal{E}(\tau)$ field drops to recover the single undressed resonance. The dressing occurs within each optical cycle of 2.7 fs when constructive interference maximizes $\mathcal{E}(\tau)$. As expected for the AC Stark effect [Equation (6.2)], the AT doublet structure disappears when $\mathcal{E}(\tau)$ amplitude is reduced by defocusing [Figure 6.4(b)] or increasing τ. Thus, the dressing and undressing follows the instantaneous $\mathcal{E}(\tau)$ strength at the metal surface and is faster than the Cu(111) surface IP1 and SS bands dephasing, which occurs by carrier scattering [3] on ~20 fs time scale [68, 70]. Note, that the optical field experienced by SS electrons is the screened field, so one might anticipate the screening response to affect the dressing on the attosecond time scale [163].

A graphic feature that emerges from the ITR-4PP data on Cu(111) is that $k_{||}$-dispersion and optical dressing are entangled by the generalized Rabi frequency [Equation (6.2)], which depends on both $\mathcal{E}(\tau)$ and $\hbar\Delta(k_{||})$. The entanglement is directly evident in the $2\omega_l$-IFT-spectral component, which we extract from the data in Figure 6.3(a) and examine as a function of $k_{||}$ and τ in Figure 6.5. Figure 6.5 conveys how the $E_f(k_{||})$-dependent polarization spectra, change as τ is advanced in $\Delta\tau$~100 as steps to define the total $\mathcal{E}(\tau)$ field. The selected frames in Figure 6.5 (b-e) highlight how changing $\mathcal{E}(\tau)$ and $k_{||}$-dispersion affect the AT doublet dressing of the coupled bands. For τ=65 fs [Figure 6.5(e)], the pump and probe fields do not overlap, so the instantaneous $\mathcal{E}(\tau)$ is that of a single pulse and the spectra reproduce the undressed $k_{||}$-dispersions of the IP1 and SS bands (black lines). By contrast, for $|\tau| \leq 15$ fs [Figure 6.5(b-d)], the pump and probe fields add coherently, sufficiently increasing $\mathcal{E}(\tau)$ when in-phase to cause the $k_{||}$- and τ-dependent dressing,

and thereby modify the band dispersions. As $\hbar\Delta(k_{||})$ increases, however, the bands detune from resonance and therefore dressing diminishes causing them to converge to the undressed ones which is highlighted by the black solid lines in Figure 6.5(b-d). This entanglement of band dispersion and dressing causes the quasiparticle band masses to become τ-dependent. Thus, dressing can transform an electron into a hole band, potentially reversing the carrier transport in response to a femtosecond time-scale optical field [198].

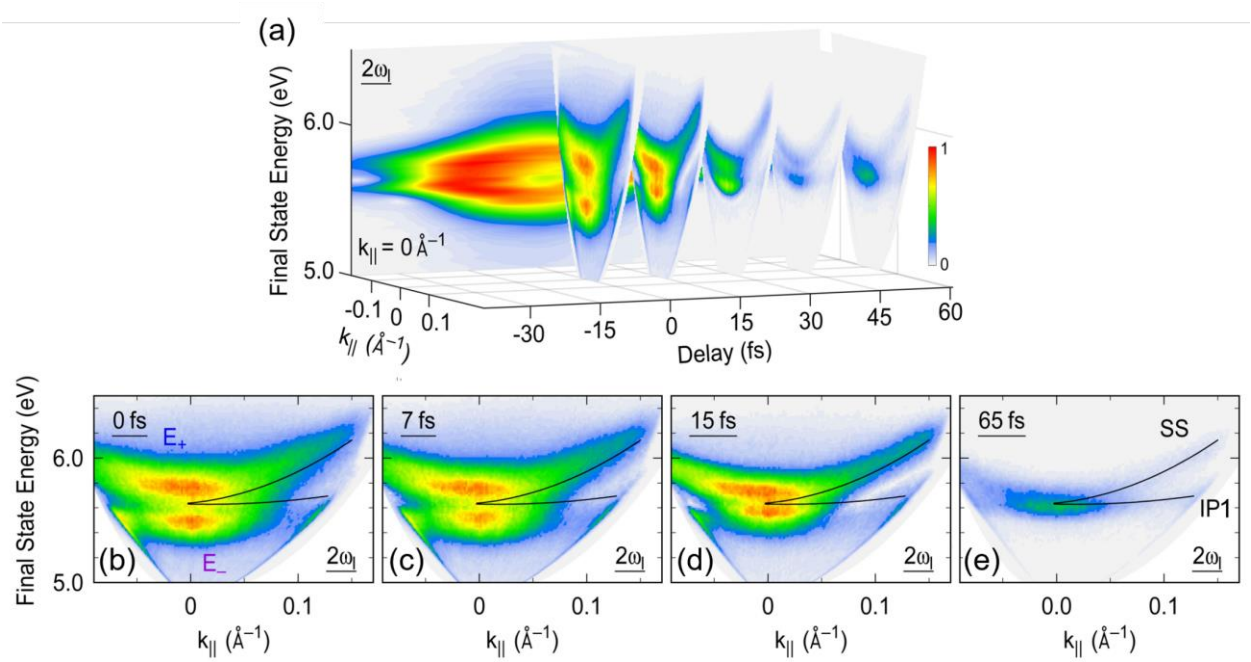

Figure 6.5 Real-time spectra of the $k_{||}$-dispersion-optical field entanglement. (a) IFT of the $2\omega_I$-polarization component of Figure 6.3(a) data provides a 3D presentation of the Fourier filtered $E_f(k_{||},\tau)$ data which resolves AT doublet frames (the individual frames show the $E_f(k_{||})$-spectra in 15 fs intervals). The back panel is the τ-dependence of the IFT $E_f(k_{||}=0\text{Å}^{-1})$ profile, such as in Figure 6.3(a). (b-e) $E_f(k_{||})$-resolved snapshots for τ=0, 7, 15, and 65 fs showing undressing as τ is increased. As a reference, the black lines indicate dispersions of the undressed SS and IP1 bands obtained at τ=100 fs from the unfiltered ITR-4PP data, where the dressing is undetectable.

Besides the dressing and $k_{\|}$-dispersion entanglement and dephasing, however, we must consider the dressing from a solid-state perspective. A quasiparticle in a solid is defined by its many-body interactions, specifically how a solid state plasma responds to its Coulomb fields on a sub-femtosecond screening time scale [2, 93]. The IP1 band is not pre-existing, and forms through the many-body screening response of a metal [19, 163], and therefore, the screening and dressing temporal responses must be interdependent on the attosecond time scale. To examine this, further theoretical and experimental scrutiny is needed. The experiments shown here, examine the field dependent response of metals, which is not constrained by energy-time uncertainty. Of course, energy-time uncertainty must be satisfied when a photon is absorbed, and the optically induced coherence has decayed, but this is typically considerably longer than the optical cycle period.

6.3 Dressing with Higher Laser Fluences

Following the preceding illustration of the electric field strength $\mathcal{E}$- and $k_{\|}$-dependent optical dressing on the Cu(111) surfaces, I will show next an examination of the electronic response to even higher optical fields, which requires further analysis. As discussed previously, the high field-strength excitation is still in the perturbative regime, because the Keldysh parameter $\gamma \sim 10$ is still >1 [210]. The two different field strength data shown before in Figure 6.4(a, b) are comparable to the laser fluences used in Figure 6.6(a, b). If I increase the laser fluence further, however, the response does not simply follow the same trend. The highest two fluences of IFT of the $E_f(\tau)$-$2\omega_l$-polarization component is shown in (c, d).

From Figure 6.6(e) which plots the line profile $E_f(\tau=0)$ at four different fluences, it is clear that in the 4PP region, the splitting between $E_{\pm}$ dressed states becomes increasingly larger as the

fluence is increased as expected. In addition, in between the $E_{\pm}$ states, where the original 3-photon resonance happens, a central peak emerges and grows in intensity with increasing fluence, but stays at a fixed energy. Further analysis in the right panel of Figure 6.6(c, d) shows that the $2\omega_l$-polarization oscillation field component of this new peak is π phase-shifted compared with the $E_{\pm}$ states (the red and blue colors represent opposite phase).

Also note that the AT doublet lines become skewed. This could arise from the incipient shifting of the vacuum level by the applied optical field. One consequence of such line shape skewing is that the IP1 state begins to be emitted at 3PP, without absorbing an additional photon. This is evident in line profiles of Figure 6.6(e), where the signal intensity at the work function edge rises relative to the 4PP AT doublet peaks. This is happening because the 3-photon excited IP1←SS transition is skewed so that its high energy tail projects above the vacuum level enabling 3PP signal to emerge. Note, that the measured vacuum level energy remains the same, but apparently the field is able to draw IP1 electrons into vacuum thereby to induce photoemission during the peak overlap between the pump and probe fields.

Another feature is the shifting of 5PP/ATP signal, which can be seen from two aspects. Firstly, the line profile in Figure 6.6(e) shows in a straightforward way the shifting of 5PP peaks towards higher energy positions with increasing fluence. Secondly, the 'triangle' shape of 5PP signal in Figure 6.6(b-d) also indicates the same behavior. Comparison between the 4PP and 5PP signal in the lowest fluence data [Figure 6.6(a)] shows symmetric peak shapes [red line in Figure 6.6(e)]. However, with increasing fluence, the $|\tau|\rightarrow 0$ part of 5PP signal 'protrudes' towards higher energies, forming into a triangle shape. That can also be explained by the 5PP signal shifting to higher energies at higher fluence because the electric field strength increases with $|\tau|\rightarrow 0$. Thus, the 5PP signal energy position is sensitive to the electric field strength, and its shape and phase

resembles that of the E_+ state in 4PP. This energy shifting of peak is not due to space charge effect because (i) the shifting of peaks in space charge effect happens to all spectral features and shifts towards the same direction, which is not the case here (cf. 4PP $E_\pm$ states energies); (ii) the center peak between dressed states $E_\pm$ in 4PP has a systematic phase shift from other signals, which will not be expected from space-charge effects.

The appearance of this central peak and the triangle shape of the 5PP signal may be related. At the highest intensity the 5PP signal is most intense. In the next order of nonlinearity we expect the five-photon Floquet band to gain Volkov side bands to form by upward and downward transitions from 5PP. This will remove some density from 5PP feature in a manner that needs consideration, and it will stimulate a signal to 4PP with the opposite phase from 4PP absorption signal.

Note, that if space-charge affected 5PP, the same effect should occur at 4PP. In fact, because 4PP electrons have lower kinetic energy from absorbing 4 photons, than 5PP electrons, the space charge effect should be more pronounced at 4PP. Likewise, if the optical field pulls down (and up) the vacuum level, the same thing should happen at 4PP. Note, that the dressing of the SS and IP1 state is not a simple two level system problem, as implied by the Bloch equation model, but the excitation is occurring in presence of the Fermi sea, and IP1 is dressed so that it becomes resonant with the U_{sp} band, and thereby becomes a resonance for about 1/2 of the dressing field cycle. For these reasons, we conclude that the differences arise from the dipole dressing of the eigenstates, as we have already shown at 4PP, but high fields introduce effects that are beyond the atomic AT dressing model, that requires further development of theory of dressing of solid state bands. These are the several significant features with high laser fluence excitation that need further consideration.

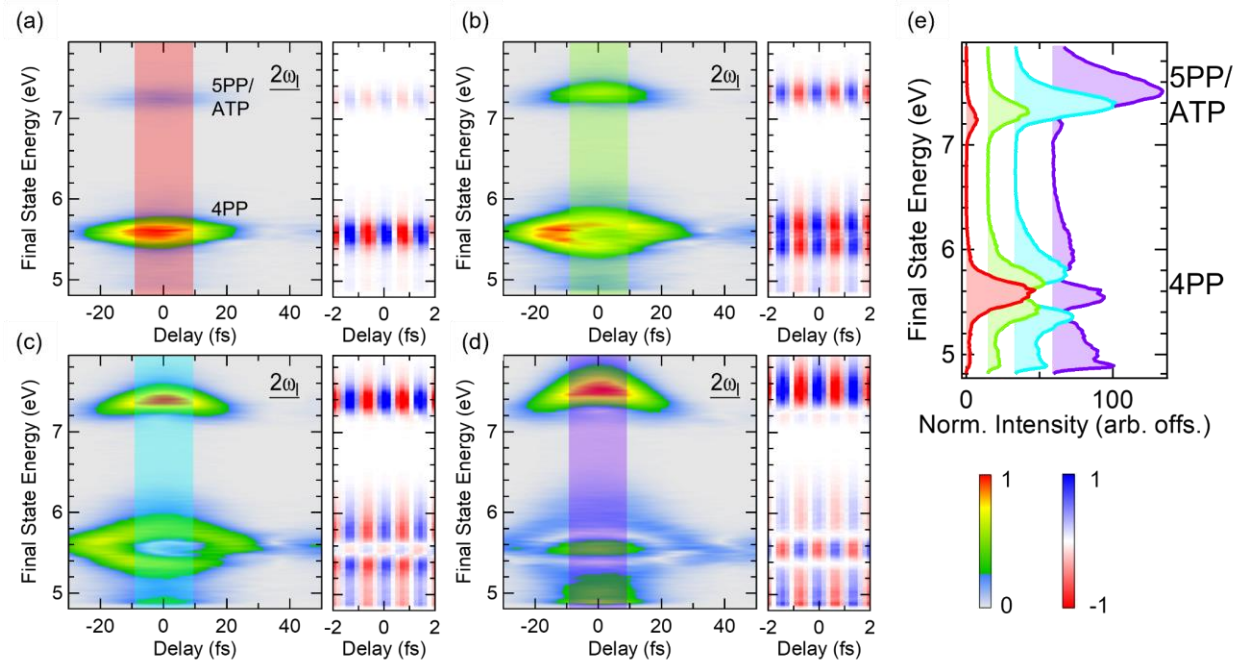

Figure 6.6 Femtosecond $\mathcal{E}(\tau)$ field dressing of the surface bands with increasing laser fluence. (a-d) IFT of the $2\omega_I$-polarization component with increasing fluence from (a) to (d). Right panel in each figure plots the $2\omega_I$-polarization oscillation component while the left panel plots its envelope. The positive (blue) and negative (red) fields represent the opposite phase between different peaks. (e) $E_f(\tau=0)$ line profiles (shaded area) taken at four different laser fluence in (a-d). Clear separation between dressed states appears in 4PP, while at the highest fluence a third peak emerges from the center. 5PP peaks shift to higher energies and become skewed with increasing laser fluences.

Nevertheless, my 3D coherent photoelectron data shows that electronic bands are no longer defined just by the lattice potential, but applying a time-periodic external field introduces new Floquet bands, and causes shifts of nonlinearly-excited resonant electronic bands through the AC Stark effect; specifically, breaking of the time-translation symmetry creates new nonequilibrium electronic structures within the solid-state, and opening of gaps between the time and space derived bands entangles the space ($k_{||}$) and time degrees of freedom, introducing frequency responses faster

than that of the driving field. Our multidimensional spectroscopy approach shows that optical dressing dynamics that may be obscured in time integrated light intensity-dependent spectra, can become conspicuous by probing the induced coherences in electric field-dependent measurements. Such responses can be measured and modified even for high electron density materials like metals, where electronic dephasing is fast. Moreover, the entanglement between dressing and band dispersions provides the means to optically control the physical properties that depend on the quasiparticle band mass on a few femtosecond time scale. Electron mass is no longer defined by the lattice potential and wavefunction overlap, but can respond nearly instantaneously to the applied optical fields.

7.0 Summary

To summarize, I have studied the coherent ultrafast excitations of noble metal surfaces with multiphoton photoemission techniques, and discovered novel phenomena in both the excitation spectra and excitation dynamics.

The energy and momentum-resolved 2-4PP spectra from the pristine Ag(110) surface are measured by multidimensional momentum microscopy and angle-resolved multiphoton photoemission spectroscopy. I identified the participation of two Shockley surface states centered at the $\overline{Y}$ point as the initial and intermediate states in mPP excitation processes that can be excited through different pathways in different order excitations. I have also identified a surface state within a mini-band gap, which is strongly anisotropic around the $\overline{\Gamma}$ point in the momentum space, and acts as a final state for the plasmonically induced emission in 2PP. Other states that can be effectively populated include the first and the second image potential states as well as several regions of the bulk *sp*-bands. This was the second study of (110) surface of a noble metal by nonlinear multiphoton photoemission. Together with the first study of Cu(110) by Sonoda [178], it is now clear that such surfaces reveal a wealth of spectroscopic features, which is significantly different from the well-known (111) and (100) surfaces, but nevertheless, offers new information on the optical properties of metals.

Moreover, the photon energy dependent spectra of three low-index silver single crystals reveal the plasmon excitation in silver. The two photon *sp*-band transition can be enhanced by the excitation of silver multiple surface plasmon field. By tuning the excitation frequency above the bulk plasmon frequency, the bulk plasmon mode of silver can be excited and the decay of this mode will preferentially excite electrons from the Fermi level. We also show that on Ag(110)

surfaces, the polarization field induced by the displacement of the charge distribution of two Shockley states may excite the bulk plasmon mode which usually cannot be excited by surface parallel field. This plasmonic excitation on Ag(110) surfaces terminates in the anisotropic surface state at the $\overline{\Gamma}$ point. These non-Einsteinian photoexcitation pathways may shine a light on our understanding of optical energy harvesting in electronic materials.

From the perspective of ultrafast dynamics, I first investigated the coherent excitation from the Shockley surface states on Ag(111) in 2-5PP processes by experiments and simulations. The non-resonant energy level climbing of SS electrons in the perturbative regime is dominantly caused by oscillations of the nonlinear polarization at high orders of the driving field, as recorded by ITR-mPP measurements and their Fourier analysis. This is direct evidence that the mPP signal can be thought of as a Floquet engineering process. The coherent nature of excitations is encoded in the tilting of 2D-Fourier spectra features, which shows a correlation of a specific final state with a specific frequency in the induced polarization field. This causes slopes of the Fourier amplitudes to tilt with a ratio of n/m , where n is the (non-)linear order of the polarization and m is the order of mPP process. I have also reported the first coherent spectroscopic investigation of perturbative ATP processes in solids, which shows that ATP involving nonresonant excitations can be understood as a one-step coherent process where electrons are excited by rectification of a higher nonlinear order signal than the main mPP signal, rather than the previously envisaged two-step process where a photoelectron is generated and absorbs another photon before escaping from the surface.

I further investigated the three-photon resonant transition dynamics from SS to IP1 state on Cu(111) surfaces. By Fourier filtering signals of different order polarization fields, I could reveal signatures of optical dressing of electronic bands in form of Autler-Townes doublet and

Mollow triplet structures which are obscured in the time-integrated data. This optical dressing of surface states is explained by the generation of Floquet states due to the time periodicity of external field, and the AC Stark effect caused by the shifting of nonlinearly excited resonant electronic bands. By probing the induced coherences in electric field-dependent measurements, dressing can be measured even within high electron density systems like metals, which are known to undergo fast dephasing. Moreover, the $k_{||}$ dependent dressing which changes band dispersions with different external field strength enables tuning by optical control physical properties of solids that depend on the quasiparticle band mass. The resonant dressing of the bands shows departures from the expected behavior of perturbative light-matter interaction, which suggests that we are able to reach the threshold of nonperturbative strong-field light matter dynamics. I leave the progress in this direction to students who will follow in my footsteps.

In conclusion, my study demonstrates that the studies of the oldest optical material, a metallic surface, along with those of other high electron density solids, not only reflect the passive coherent responses to optical fields involving mPP single particle interband transitions and collective plasmonic excitations, but can also be actively controlled with sub-femtosecond precision by strong nonlinear interactions with phase and amplitude tailored optical fields.

Bibliography

1. Enoch, J. M., History of mirrors dating back 8000 years. *Optom Vis Sci* **2006,** *83* (10), 775-81.

2. Feibelman, P., Surface electromagnetic fields. *Progress in Surface Science* **1982,** *12* (4), 287-407.

3. Echenique, P. M.; Berndt, R.; Chulkov, E. V.; Fauster, T.; Goldmann, A.; Höfer, U., Decay of electronic excitations at metal surfaces. *Surface Science Reports* **2004,** *52* (7-8), 219-317.

4. Reinert, F.; Nicolay, G.; Schmidt, S.; Ehm, D.; Hüfner, S., Direct measurements of theL-gap surface states on the (111) face of noble metals by photoelectron spectroscopy. *Physical Review B* **2001,** *63* (11), 115415.

5. Bauer, M.; Marienfeld, A.; Aeschlimann, M., Hot electron lifetimes in metals probed by time-resolved two-photon photoemission. *Progress in Surface Science* **2015,** *90* (3), 319-376.

6. Petek, H.; Ogawa, S., Femtosecond time-resolved two-photon photoemission studies of electron dynamics in metals. *Progress in Surface Science* **1997,** *56* (4), 239-310.

7. Weinelt, M., Time-resolved two-photon photoemission from metal surfaces. *Journal of Physics: Condensed Matter* **2002,** *14* (43), R1099-R1141.

8. Chan, W. L.; Ligges, M.; Jailaubekov, A.; Kaake, L.; Miaja-Avila, L.; Zhu, X. Y., Observing the multiexciton state in singlet fission and ensuing ultrafast multielectron transfer. *Science* **2011,** *334* (6062), 1541-5.

9. Tautz, F. S., Structure and bonding of large aromatic molecules on noble metal surfaces: The example of PTCDA. *Progress in Surface Science* **2007,** *82* (9-12), 479-520.

10. Zhan, C.; Chen, X.-J.; Yi, J.; Li, J.-F.; Wu, D.-Y.; Tian, Z.-Q., From plasmon-enhanced molecular spectroscopy to plasmon-mediated chemical reactions. *Nature Reviews Chemistry* **2018,** *2* (9), 216-230.

11. Xu, J.; Zhu, X.; Tan, S.; Zhang, Y.; Li, B.; Tian, Y.; Shan, H.; Cui, X.; Zhao, A.; Dong, Z.; Yang, J.; Luo, Y.; Wang, B.; Hou, J. G., Determining structural and chemical heterogeneities of surface species at the single-bond limit. *Science* **2021,** *371* (6531), 818-822.

12. Puschnig, P.; Berkebile, S.; Fleming, A. J.; Koller, G.; Emtsev, K.; Seyller, T.; Riley, J. D.; Ambrosch-Draxl, C.; Netzer, F. P.; Ramsey, M. G., Reconstruction of molecular orbital densities from photoemission data. *Science* **2009,** *326* (5953), 702-6.

13. Leandri, C.; Lay, G. L.; Aufray, B.; Girardeaux, C.; Avila, J.; Dávila, M. E.; Asensio, M. C.; Ottaviani, C.; Cricenti, A., Self-aligned silicon quantum wires on Ag(110). *Surface Science* **2005,** *574* (1), L9-L15.

14. Ohta, M.; Watanabe, K.; Matsumoto, Y., Photoinduced Elimination of Oxygen at Ag(110)-p(2 × 1)-O: The Role of Surface Carbon Species. *The Journal of Physical Chemistry B* **2001,** *105* (34), 8170-8177.

15. Jansen, G. S. M.; Keunecke, M.; Düvel, M.; Möller, C.; Schmitt, D.; Bennecke, W.; Kappert, F. J. S.; Steil, D.; Luke, D. R.; Steil, S.; Mathias, S., Efficient orbital imaging based on ultrafast momentum microscopy and sparsity-driven phase retrieval. *New Journal of Physics* **2020,** *22* (6), 063012.

16. Wallauer, R.; Raths, M.; Stallberg, K.; Munster, L.; Brandstetter, D.; Yang, X.; Gudde, J.; Puschnig, P.; Soubatch, S.; Kumpf, C.; Bocquet, F. C.; Tautz, F. S.; Hofer, U., Tracing orbital images on ultrafast time scales. *Science* **2021,** *371* (6533), 1056-1059.

17. Aslam, U.; Rao, V. G.; Chavez, S.; Linic, S., Catalytic conversion of solar to chemical energy on plasmonic metal nanostructures. *Nature Catalysis* **2018,** *1* (9), 656-665.

18. Kamat, P. V.; Hartland, G. V., Plasmons for Energy Conversion. *ACS Energy Letters* **2018,** *3* (6), 1467-1469.

19. Cui, X.; Wang, C.; Argondizzo, A.; Garrett-Roe, S.; Gumhalter, B.; Petek, H., Transient excitons at metal surfaces. *Nature Physics* **2014,** *10* (7), 505-509.

20. Eckardt, H.; Fritsche, L.; Noffke, J., Self-Consistent Relativistic Band-Structure of the Noble-Metals. *Journal of Physics F-Metal Physics* **1984,** *14* (1), 97-112.

21. Rosei, R., Temperature modulation of the optical transitions involving the Fermi surface in Ag: Theory. *Physical Review B* **1974,** *10* (2), 474-483.

22. Shockley, W., On the Surface States Associated with a Periodic Potential. *Physical Review* **1939,** *56* (4), 317-323.

23. Oura, K., *Surface science : an introduction*. Springer: Berlin; London, 2011.

24. Echenique, P. M.; Pendry, J. B., Theory of image states at metal surfaces. *Progress in Surface Science* **1989,** *32* (2), 111-159.

25. Jackson, J. D., *Classical Electrodynamics*. 3rd Ed. ed.; John Wiley & Sons: New York, 1999.

26. Chulkov, E. V.; Silkin, V. M.; Echenique, P. M., Image potential states on metal surfaces: binding energies and wave functions. *Surface Science* **1999,** *437* (3), 330-352.

27. Giesen, K.; Hage, F.; Himpsel, F. J.; Riess, H. J.; Steinmann, W.; Smith, N. V., Effective mass of image-potential states. *Phys Rev B Condens Matter* **1987,** *35* (3), 975-978.

28. Urbach, L. E.; Percival, K. L.; Hicks, J. M.; Plummer, E. W.; Dai, H. L., Resonant surface second-harmonic generation: Surface states on Ag(110). *Phys Rev B Condens Matter* **1992,** *45* (7), 3769-3772.

29. Gerlach, A.; Meister, G.; Matzdorf, R.; Goldmann, A., High-resolution photoemission study of the $\bar{Y}$ surface state on Ag(110). *Surface Science* **1999,** *443* (3), 221-226.

30. Altmann, W.; Dose, V.; Goldmann, A., Momentum-resolved bremsstrahlung isochromat spectroscopy of silver surfaces. *Zeitschrift für Physik B Condensed Matter* **1986,** *65* (2), 171–180.

31. Pascual, J. I.; Song, Z.; Jackiw, J. J.; Horn, K.; Rust, H. P., Visualization of surface electronic structure: Dispersion of surface states of Ag(110). *Physical Review B* **2001,** *63* (24), 241103(R).

32. Eul, T.; Braun, J.; Stadtmuller, B.; Ebert, H.; Aeschlimann, M., Spectroscopic Evidence for a New Type of Surface Resonance at Noble-Metal Surfaces. *Phys Rev Lett* **2021,** *127* (19), 196405.

33. Kleimeier, N. F.; Wenzel, G.; Urban, A. J.; Tchalala, M. R.; Oughaddou, H.; Dedkov, Y.; Voloshina, E.; Zacharias, H., Unoccupied electronic band structure of pentagonal Si nanoribbons on Ag(110). *Phys Chem Chem Phys* **2019,** *21* (32), 17811-17820.

34. Tsirkin, S. S.; Eremeev, S. V.; Chulkov, E. V., Model pseudopotential for the Cu(110) surface. *Physics of the Solid State* **2010,** *52* (1), 188-194.

35. Tsirkin, S. S.; Chulkov, E. V., Image potential eigenstates and resonances on the (110) surfaces of noble metals: Energies and lifetimes. *Journal of Experimental and Theoretical Physics* **2014,** *118* (2), 167-175.

36. Li, A.; Reutzel, M.; Wang, Z.; Novko, D.; Gumhalter, B.; Petek, H., Plasmonic Photoemission from Single-Crystalline Silver. *ACS Photonics* **2021,** *8* (1), 247-258.

37. Novko, D.; Despoja, V.; Reutzel, M.; Li, A.; Petek, H.; Gumhalter, B., Plasmonically assisted channels of photoemission from metals. *Physical Review B* **2021,** *103* (20), 205401.

38. Winkelmann, A.; Akin Ünal, A.; Tusche, C.; Ellguth, M.; Chiang, C.-T.; Kirschner, J., Directk-space imaging of Mahan cones at clean and Bi-covered Cu(111) surfaces. *New Journal of Physics* **2012,** *14* (8), 083027.

39. Giesen, K.; Hage, F.; Himpsel, F. J.; Riess, H. J.; Steinmann, W., Two-photon photoemission via image-potential states. *Phys Rev Lett* **1985,** *55* (3), 300-303.

40. Garrett-Roe, S.; Shipman, S. T.; Szymanski, P.; Strader, M. L.; Yang, A.; Harris, C. B., Ultrafast electron dynamics at metal interfaces: intraband relaxation of image state electrons as friction. *J Phys Chem B* **2005,** *109* (43), 20370-8.

41. Marks, M.; Schwalb, C. H.; Schubert, K.; Güdde, J.; Höfer, U., Quantum-beat spectroscopy of image-potential resonances. *Physical Review B* **2011,** *84* (24), 245402.

42. Fauster, T.; Weinelt, M.; Höfer, U., Quasi-elastic scattering of electrons in image-potential states. *Progress in Surface Science* **2007,** *82* (4-6), 224-243.

43. Reutzel, M.; Li, A.; Petek, H., Coherent Two-Dimensional Multiphoton Photoelectron Spectroscopy of Metal Surfaces. *Physical Review X* **2019,** *9* (1), 011044.

44. Vitali, L.; Wahl, P.; Schneider, M. A.; Kern, K.; Silkin, V. M.; Chulkov, E. V.; Echenique, P. M., Inter- and intraband inelastic scattering of hot surface state electrons at the Ag() surface. *Surface Science* **2003,** *523* (1-2), L47-L52.

45. Höfer, U.; Echenique, P. M., Resolubility of image-potential resonances. *Surface Science* **2016,** *643*, 203-209.

46. Rosei, R.; Culp, C. H.; Weaver, J. H., Temperature modulation of the optical transitions involving the Fermi surface in Ag: Experimental. *Physical Review B* **1974,** *10* (2), 484-489.

47. Knoesel, E.; Hotzel, A.; Hertel, T.; Wolf, M.; Ertl, G., Dynamics of photoexcited electrons in metals studied with time-resolved two-photon photoemission. *Surface Science* **1996,** *368* (1-3), 76-81.

48. Tsirkin, S. S.; Eremeev, S. V.; Chulkov, E. V., Inelastic electron-electron scattering for surface states on Cu(110) and Ag(110). *Physical Review B* **2011,** *84* (11), 115451.

49. Borensztein, Y., Investigation of nonlocal electromagnetic phenomena in thin silver films near the plasma frequency. *Journal of the Optical Society of America* **1983,** *73* (1).

50. Borensztein, Y.; Mochan, W. L.; Tarriba, J.; Barrera, R. G.; Tadjeddine, A., Large anisotropy in the optical reflectance of Ag(110) single crystals: Experiment and theory. *Phys Rev Lett* **1993,** *71* (14), 2334-2337.

51. Calmels, L.; Inglesfield, J. E.; Arola, E.; Crampin, S.; Rasing, T., Local-field effects on the near-surface and near-interface screened electric field in noble metals. *Physical Review B* **2001,** *64* (12).

52. Bouarab, S.; Mebarki, M.; Ziane, A.; Khan, M. A., Ab initioorigin of optical anisotropy in Ag(110). *Physical Review B* **2001,** *63* (19).

53. Martin, D. S.; Blanchard, N. P.; Weightman, P.; Roseburgh, D. S.; Cole, R. J.; Hansen, J. K.; Bremer, J.; Hunderi, O., Optical reflectance anisotropy of Ag(110): Evidence for contributions from surface-modified bulk band transitions. *Physical Review B* **2007,** *76* (11), 115403.

54. Farrell, T.; Harrison, P.; Smith, C. I.; Martin, D. S.; Weightman, P., Azimuthal dependent reflection anisotropy spectroscopy of Ag(110) near the plasmon resonance energy. *Applied Physics Letters* **2008,** *93* (19), 191102.

55. Li, A.; James, N. A.; Wang, T.; Wang, Z.; Petek, H.; Reutzel, M., Towards full surface Brillouin zone mapping by coherent multi-photon photoemission. *New Journal of Physics* **2020,** *22* (7), 073035.

56. Kröger, J.; Becker, M.; Jensen, H.; von Hofe, T.; Néel, N.; Limot, L.; Berndt, R.; Crampin, S.; Pehlke, E.; Corriol, C.; Silkin, V. M.; Sánchez-Portal, D.; Arnau, A.; Chulkov, E. V.; Echenique, P. M., Dynamics of surface-localised electronic excitations studied with the scanning tunnelling microscope. *Progress in Surface Science* **2007,** *82* (4-6), 293-312.

57. Wern, H.; Courths, R.; Leschik, G.; Hüfner, S., On the band structure of silver and platinum from angle-resolved photoelectron spectroscopy (ARUPS) measurements. *Zeitschrift für Physik B Condensed Matter* **1985,** *60* (2), 293-310.

58. Roth, F.; Arion, T.; Kaser, H.; Gottwald, A.; Eberhardt, W., Angle resolved Photoemission from Ag and Au single crystals: Final state lifetimes in the attosecond range. *Journal of Electron Spectroscopy and Related Phenomena* **2018,** *224*, 84-92.

59. Miller, T.; McMahon, W. E.; Chiang, T. C., Interference between Bulk and Surface Photoemission Transitions in Ag(111). *Phys Rev Lett* **1996,** *77* (6), 1167-1170.

60. Miller, T.; Chiang, T. C., Lineshape effects in photoemission from the valence states of metals. *Journal of Physics: Condensed Matter* **2001,** *13* (49), 11115-11132.

61. Pawlik, S.; Burgermeister, R.; Bauer, M.; Aeschlimann, M., Direct transition in the system Ag(111) studied by one- and two-photon photoemission. *Surface Science* **1998,** *402-404*, 556-560.

62. Pontius, N.; Sametoglu, V.; Petek, H., Simulation of two-photon photoemission from the bulksp-bands of Ag(111). *Physical Review B* **2005,** *72* (11), 115105.

63. Winkelmann, A.; Sametoglu, V.; Zhao, J.; Kubo, A.; Petek, H., Angle-dependent study of a direct optical transition in thespbands of Ag(111) by one- and two-photon photoemission. *Physical Review B* **2007,** *76* (19), 195428.

64. Schubert, K.; Damm, A.; Eremeev, S. V.; Marks, M.; Shibuta, M.; Berthold, W.; Güdde, J.; Borisov, A. G.; Tsirkin, S. S.; Chulkov, E. V.; Höfer, U., Momentum-resolved electron dynamics of image-potential states on Cu and Ag surfaces. *Physical Review B* **2012,** *85* (20).

65. Schoenlein, R. W.; Fujimoto, J. G.; Eesley, G. L.; Capehart, T. W., Femtosecond relaxation dynamics of image-potential states. *Phys. Rev. B* **1991,** *43* (6), 4688-4698.

66. Lingle Jr, R. L.; Ge, N. H.; Jordan, R. E.; McNeill, J. D.; Harris, C. B., Femtosecond studies of electron tunneling at metal-dielectric interfaces. *Chem. Phys.* **1996,** *205* (1-2), 191-203.

67. Tsirkin, S. S.; Eremeev, S. V.; Chulkov, E. V.; Marks, M.; Schubert, K.; Güdde, J.; Höfer, U., Temperature dependence of the dynamics of the first image-potential state on Ag(111). *Phys. Rev. B* **2012,** *86* (8), 085424.

68. Ogawa, S.; Nagano, H.; Petek, H.; Heberle, A. P., Optical Dephasing in Cu(111) Measured by Interferometric Two-Photon Time-Resolved Photoemission. *Physical Review Letters* **1997,** *78* (7), 1339-1342.

69. Ogawa, S.; Nagano, H.; Petek, H., Phase and energy relaxation in an anti-bonding surface state: Cs/Cu(111). *Phys. Rev. Lett.* **1999,** *82*, 1931-1934.

70. Knoesel, E.; Hotzel, A.; Wolf, M., Temperature dependence of surface state lifetimes, dephasing rates and binding energies on Cu(111) studied with time-resolved photoemission. *Journal of Electron Spectroscopy and Related Phenomena* **1998,** *88-91*, 577-584.

71. Bisio, F.; Nyvlt, M.; Franta, J.; Petek, H.; Kirschner, J., Mechanisms of high-order perturbative photoemission from Cu(001). *Phys Rev Lett* **2006,** *96* (8), 087601.

72. Sirotti, F.; Beaulieu, N.; Bendounan, A.; Silly, M. G.; Chauvet, C.; Malinowski, G.; Fratesi, G.; Véniard, V.; Onida, G., Multiphotonk-resolved photoemission from gold surface states with 800-nm femtosecond laser pulses. *Physical Review B* **2014,** *90* (3), 035401.

73. Fann, W. S.; Storz, R.; Bokor, J., Observation of above-threshold multiphoton photoelectric emission from image-potential surface states. *Physical Review B* **1991,** *44* (19), 10980.

74. Aeschlimann, M.; Schmuttenmaer, C. A.; Elsayed-Ali, H. E.; Miller, R. J. D.; Cao, J.; Gao, Y.; Mantell, D. A., Observation of surface enhanced multiphoton photoemission from metal surfaces in the short pulse limit. *J. Chem. Phys.* **1995,** *102* (21), 8606-8613.

75. Homann, C.; Schriever, C.; Baum, P.; Riedle, E., Octave wide tunable UV-pumped NOPA: pulses down to 20 fs at 0.5 MHz repetition rate. *Optics Express* **2008,** *16* (8).

76. Schriever, C.; Lochbrunner, S.; Krok, P.; Riedle, E., Tunable pulses from below 300 to 970 nm with durations down to 14 fs based on a 2 MHz ytterbium-doped fiber system. *Optics Letters* **2008,** *33* (2).

77. Wang, C. Three Dimensional Coherent Photoemission Spectroscopy. University of Pittsburgh, 2017.

78. Keunecke, M.; Moller, C.; Schmitt, D.; Nolte, H.; Jansen, G. S. M.; Reutzel, M.; Gutberlet, M.; Halasi, G.; Steil, D.; Steil, S.; Mathias, S., Time-resolved momentum microscopy with a 1 MHz high-harmonic extreme ultraviolet beamline. *Rev Sci Instrum* **2020,** *91* (6), 063905.

79. Keunecke, M.; Reutzel, M.; Schmitt, D.; Osterkorn, A.; Mishra, T. A.; Möller, C.; Bennecke, W.; Jansen, G. S. M.; Steil, D.; Manmana, S. R.; Steil, S.; Kehrein, S.; Mathias, S., Electromagnetic dressing of the electron energy spectrum of Au(111) at high momenta. *Physical Review B* **2020,** *102* (16), 161403(R).

80. Medjanik, K.; Fedchenko, O.; Chernov, S.; Kutnyakhov, D.; Ellguth, M.; Oelsner, A.; Schonhense, B.; Peixoto, T. R. F.; Lutz, P.; Min, C. H.; Reinert, F.; Daster, S.; Acremann, Y.; Viefhaus, J.; Wurth, W.; Elmers, H. J.; Schonhense, G., Direct 3D mapping of the Fermi surface and Fermi velocity. *Nat Mater* **2017,** *16* (6), 615-621.

81. Hüfner, S., *Photoelectron Spectroscopy: Principles and Applications*. Springer: Berlin, Heidelberg, 2003.

82. Tan, S.; Dai, Y.; Zhang, S.; Liu, L.; Zhao, J.; Petek, H., Coherent Electron Transfer at the Ag/Graphite Heterojunction Interface. *Phys Rev Lett* **2018,** *120* (12), 126801.

83. Zhang, S.; Wang, C.; Cui, X.; Wang, Y.; Argondizzo, A.; Zhao, J.; Petek, H., Time-resolved photoemission study of the electronic structure and dynamics of chemisorbed alkali atoms on Ru(0001). *Physical Review B* **2016,** *93* (4).

84. Hertel, T.; Knoesel, E.; Wolf, M.; Ertl, G., Ultrafast electron dynamics at Cu(111): Response of an electron gas to optical excitation. *Phys Rev Lett* **1996,** *76* (3), 535-538.

85. Ueba, H.; Gumhalter, B., Theory of two-photon photoemission spectroscopy of surfaces. *Progress in Surface Science* **2007,** *82* (4-6), 193-223.

86. Weinelt, M., Decay and dephasing of image-potential states studied by time-resolved two-photon photoemission. *Surface Science* **2001,** *482-485*, 519-529.

87. Li, A.; Reutzel, M.; Wang, Z.; Schmitt, D.; Keunecke, M.; Bennecke, W.; Matthijs Jansen, G. S.; Steil, D.; Steil, S.; Novko, D.; Gumhalter, B.; Mathias, S.; Petek, H., Multidimensional multiphoton momentum microscopy of the anisotropic Ag(110) surface. *Physical Review B* **2022,** *105* (7).

88. Reutzel, M.; Li, A.; Petek, H., Above-threshold multiphoton photoemission from noble metal surfaces. *Physical Review B* **2020,** *101* (7), 075409.

89. Fauster, T.; Steinmann, W., Two-Photon Photoemission Spectroscopy of Image States. In *Photonic Probes of Surfaces*, Halevi, P., Ed. Elsevier: Amsterdam, 1995; pp 347-411.

90. Ogawa, S.; Petek, H., Two-photon photoemission spectroscopy at clean and oxidized Cu(110) and Cu(100) surfaces. *Surface Science* **1996,** *363* (1-3), 313-320.

91. Li, C. M.; Urbach, L. E.; Dai, H. L., Second-harmonic generation from a Ag(111) surface at the interband transition region: Role of the dielectric function. *Phys Rev B Condens Matter* **1994,** *49* (3), 2104-2112.

92. Miller, T.; Hansen, E. D.; McMahon, W. E.; Chiang, T. C., Direct transitions, indirect transitions, and surface photoemission in the prototypical system Ag(111). *Surface Science* **1997,** *376* (1-3), 32-42.

93. Reutzel, M.; Li, A.; Gumhalter, B.; Petek, H., Nonlinear Plasmonic Photoelectron Response of Ag(111). *Phys Rev Lett* **2019,** *123* (1), 017404.

94. Song, K. J.; Heskett, D.; Dai, H. L.; Liebsch, A.; Plummer, E. W., Dynamical screening at a metal surface probed by second-harmonic generation. *Phys Rev Lett* **1988,** *61* (12), 1380-1383.

95. Pitarke, J. M.; Silkin, V. M.; Chulkov, E. V.; Echenique, P. M., Theory of surface plasmons and surface-plasmon polaritons. *Reports on Progress in Physics* **2007,** *70* (1), 1-87.

96. Tsuei, K. D.; Plummer, E. W.; Liebsch, A.; Kempa, K.; Bakshi, P., Multipole plasmon modes at a metal surface. *Phys Rev Lett* **1990,** *64* (1), 44-47.

97. Rocca, M., Surface Plasmons and Plasmonics. In *Springer Handbook of Surface Science*, Rocca, M.; Rahman, T. S.; Vattuone, L., Eds. Springer International Publishing: Cham, 2020; pp 531-556.

98. Bisio, F.; Winkelmann, A.; Chiang, C. T.; Petek, H.; Kirschner, J., Band structure effects in above threshold photoemission. *J Phys Condens Matter* **2011,** *23* (48), 485002.

99. Liebsch, A., Dynamical screening at simple-metal surfaces. *Phys Rev B Condens Matter* **1987,** *36* (14), 7378-7388.

100. Merschdorf, M.; Kennerknecht, C.; Pfeiffer, W., Collective and single-particle dynamics in time-resolved two-photon photoemission. *Physical Review B* **2004,** *70* (19), 193401.

101. Unal, A. A.; Tusche, C.; Ouazi, S.; Wedekind, S.; Chiang, C.-T.; Winkelmann, A.; Sander, D.; Henk, J.; Kirschner, J., Hybridization between the unoccupied Shockley surface state and bulk electronic states on Cu(111). *Physical Review B* **2011,** *84* (7), 073107.

102. Haag, F.; Eul, T.; Thielen, P.; Haag, N.; Stadtmüller, B.; Aeschlimann, M., Time-resolved two-photon momentum microscopy—A new approach to study hot carrier lifetimes in momentum space. *Review of Scientific Instruments* **2019,** *90* (10), 103104.

103. Haag, F.; Eul, T.; Grad, L.; Haag, N.; Knippertz, J.; Mathias, S.; Cinchetti, M.; Aeschlimann, M.; Stadtmüller, B., Momentum and energy dissipation of hot electrons in a Pb/Ag(111) quantum well system. *Physical Review B* **2021,** *104* (10), 104308.

104. Wallauer, R.; Marauhn, P.; Reimann, J.; Zoerb, S.; Kraus, F.; Güdde, J.; Rohlfing, M.; Höfer, U., Momentum-resolved observation of ultrafast interlayer charge transfer between the topmost layers of MoS2. *Physical Review B* **2020,** *102* (12), 125417.

105. Sobota, J. A.; He, Y.; Shen, Z.-X., Angle-resolved photoemission studies of quantum materials. *Reviews of Modern Physics* **2021,** *93* (2), 025006.

106. Weiss, S.; Luftner, D.; Ules, T.; Reinisch, E. M.; Kaser, H.; Gottwald, A.; Richter, M.; Soubatch, S.; Koller, G.; Ramsey, M. G.; Tautz, F. S.; Puschnig, P., Exploring three-dimensional orbital imaging with energy-dependent photoemission tomography. *Nat Commun* **2015,** *6*, 8287.

107. Kubo, A.; Pontius, N.; Petek, H., Femtosecond Microscopy of Surface Plasmon Polariton Wave Packet Evolution at the Silver/Vacuum Interface. *Nano Lett.* **2007,** *7* (2), 470-475.

108. Huang, X.; El-Sayed, M. A., Plasmonic photo-thermal therapy (PPTT). *Alexandria Journal of Medicine* **2011,** *47* (1), 1-9.

109. Kauranen, M.; Zayats, A. V., Nonlinear plasmonics. *Nat Photon* **2012,** *6* (11), 737-748.

110. Zhang, R.; Zhang, Y.; Dong, Z. C.; Jiang, S.; Zhang, C.; Chen, L. G.; Zhang, L.; Liao, Y.; Aizpurua, J.; Luo, Y.; Yang, J. L.; Hou, J. G., Chemical mapping of a single molecule by plasmon-enhanced Raman scattering. *Nature* **2013,** *498* (7452), 82-86.

111. Yang, A.; Hryn, A. J.; Bourgeois, M. R.; Lee, W.-K.; Hu, J.; Schatz, G. C.; Odom, T. W., Programmable and reversible plasmon mode engineering. *Proceedings of the National Academy of Sciences* **2016**, 201615281.

112. Cocker, T. L.; Peller, D.; Yu, P.; Repp, J.; Huber, R., Tracking the ultrafast motion of a single molecule by femtosecond orbital imaging. *Nature* **2016,** *539* (7628), 263-267.

113. Priebe, K. E.; Rathje, C.; Yalunin, S. V.; Hohage, T.; Feist, A.; Schäfer, S.; Ropers, C., Attosecond electron pulse trains and quantum state reconstruction in ultrafast transmission electron microscopy. *Nature Photonics* **2017,** *11* (12), 793-797.

114. Dąbrowski, M.; Dai, Y.; Petek, H., Ultrafast Microscopy: Imaging Light with Photoelectrons on the Nano–Femto Scale. *J. Phys. Chem. Lett.* **2017,** *8*, 4446-4455.

115. Spektor, G.; Kilbane, D.; Mahro, A. K.; Frank, B.; Ristok, S.; Gal, L.; Kahl, P.; Podbiel, D.; Mathias, S.; Giessen, H.; Meyer zu Heringdorf, F.-J.; Orenstein, M.; Aeschlimann, M., Revealing the subfemtosecond dynamics of orbital angular momentum in nanoplasmonic vortices. *Science* **2017,** *355* (6330), 1187-1191.

116. Morimoto, Y.; Baum, P., Diffraction and microscopy with attosecond electron pulse trains. *Nature Physics* **2018,** *14* (3), 252-256.

117. Tagliabue, G.; Jermyn, A. S.; Sundararaman, R.; Welch, A. J.; DuChene, J. S.; Pala, R.; Davoyan, A. R.; Narang, P.; Atwater, H. A., Quantifying the role of surface plasmon

excitation and hot carrier transport in plasmonic devices. *Nature Communications* **2018,** *9* (1), 3394.

118. Lee, J.; Crampton, K. T.; Tallarida, N.; Apkarian, V. A., Visualizing vibrational normal modes of a single molecule with atomically confined light. *Nature* **2019,** *568* (7750), 78-82.

119. Atwater, H. A., The Promise of Plasmonics. *Scientific American* **2007,** *296* (4), 56-62.

120. Kravtsov, V.; Ulbricht, R.; Atkin, J. M.; Raschke, M. B., Plasmonic nanofocused four-wave mixing for femtosecond near-field imaging. *Nat Nanotechnol* **2016,** *11* (5), 459-64.

121. Cavanagh, R. R.; King, D. S.; Stephenson, J. C.; Heinz, T. F., Dynamics of Nonthermal Reactions: Femtosecond Surface Chemistry. *J. Phys. Chem.* **1993,** *97* (4), 786-798.

122. Zhu, X. Y., Electronic structure and electron dynamics at molecule-metal interfaces: implications for molecule-based electronics. *Surf. Sci. Rep.* **2004,** *56* (1-2), 1-82.

123. Frischkorn, C.; Wolf, M., Femtochemistry at Metal Surfaces: Nonadiabatic Reaction Dynamics. *Chem. Rev.* **2006,** *106* (10), 4207-4233.

124. Merschdorf, M.; Pfeiffer, W.; Thon, A.; Voll, S.; Gerber, G., Photoemission from multiply excited surface plasmons in Ag nanoparticles. *Appl. Phys. A* **2000,** *71* (5), 547-552.

125. Christopher, P.; Xin, H.; Linic, S., Visible-light-enhanced catalytic oxidation reactions on plasmonic silver nanostructures. *Nat Chem* **2011,** *3* (6), 467-472.

126. Bernardi, M.; Mustafa, J.; Neaton, J. B.; Louie, S. G., Theory and computation of hot carriers generated by surface plasmon polaritons in noble metals. *Nat Commun* **2015,** *6*.

127. Narang, P.; Sundararaman, R.; Jermyn, A. S.; Goddard, W. A.; Atwater, H. A., Cubic Nonlinearity Driven Up-Conversion in High-Field Plasmonic Hot Carrier Systems. *The Journal of Physical Chemistry C* **2016,** *120* (37), 21056-21062.

128. Narang, P.; Sundararaman, R.; Atwater, H. A., Plasmonic hot carrier dynamics in solid-state and chemical systems for energy conversion. *Nanophotonics* **2016,** *5* (1), 96-111.

129. Podbiel, D.; Kahl, P.; Makris, A.; Frank, B.; Sindermann, S.; Davis, T. J.; Giessen, H.; Hoegen, M. H.; Meyer Zu Heringdorf, F. J., Imaging the Nonlinear Plasmoemission Dynamics of Electrons from Strong Plasmonic Fields. *Nano Lett* **2017,** *17* (11), 6569-6574.

130. Gargiulo, J.; Berté, R.; Li, Y.; Maier, S. A.; Cortés, E., From Optical to Chemical Hot Spots in Plasmonics. *Accounts of Chemical Research* **2019,** *52* (9), 2525-2535.

131. Dąbrowski, M.; Dai, Y.; Petek, H., Ultrafast Photoemission Electron Microscopy: Imaging Plasmons in Space and Time. *Chemical Reviews* **2020,** *120* (13), 6247-6287.

132. Dombi, P.; Pápa, Z.; Vogelsang, J.; Yalunin, S. V.; Sivis, M.; Herink, G.; Schäfer, S.; Groß, P.; Ropers, C.; Lienau, C., Strong-field nano-optics. *Reviews of Modern Physics* **2020,** *92* (2), 025003.

133. Cortés, E.; Govorov, A. O.; Misawa, H.; Willets, K. A., Special topic on emerging directions in plasmonics. *The Journal of Chemical Physics* **2020,** *153* (1), 010401.

134. Brown, A. M.; Sundararaman, R.; Narang, P.; Goddard, W. A., 3rd; Atwater, H. A., Nonradiative Plasmon Decay and Hot Carrier Dynamics: Effects of Phonons, Surfaces, and Geometry. *ACS Nano* **2016,** *10* (1), 957-66.

135. Tan, S.; Argondizzo, A.; Ren, J.; Liu, L.; Zhao, J.; Petek, H., Plasmonic coupling at a metal/semiconductor interface. *Nature Photonics* **2017,** *11* (12), 806-812.

136. Tan, S.; Liu, L.; Dai, Y.; Ren, J.; Zhao, J.; Petek, H., Ultrafast Plasmon-Enhanced Hot Electron Generation at Ag Nanocluster/Graphite Heterojunctions. *J Am Chem Soc* **2017,** *139* (17), 6160-6168.

137. Fröhlich, H.; Pelzer, H., Plasma Oscillations and Energy Loss of Charged Particles in Solids. *Proceedings of the Physical Society. Section A* **1955,** *68* (6), 525-529.

138. McAlister, A. J.; Stern, E. A., Plasma Resonance Absorption in Thin Metal Films. *Physical Review* **1963,** *132* (4), 1599-1602.

139. Liebsch, A., *Electronic Excitations at Metal Surfaces*. Plenum: New York, 1997; p 336.

140. Marini, A.; Del Sole, R.; Onida, G., First-principles calculation of the plasmon resonance and of the reflectance spectrum of silver in theGWapproximation. *Physical Review B* **2002,** *66* (11).

141. Wang, Y.; Plummer, E. W.; Kempa, K., Foundations of Plasmonics. *Advances in Physics* **2011,** *60* (5), 799-898.

142. Apell, P.; Ljungbert, Å.; Lundqvist, S., Non-Local Optical Effects at Metal Surfaces. *Physica Scripta* **1984,** *30* (5), 367.

143. Kempa, K.; Schaich, W. L., Nonlocal corrections to Fresnel optics: Jellium-model calculations above the bulk-plasmon threshold. *Physical Review B* **1989,** *39* (18), 13139-13145.

144. Capretti, A.; Wang, Y.; Engheta, N.; Dal Negro, L., Enhanced third-harmonic generation in Si-compatible epsilon-near-zero indium tin oxide nanolayers. *Optics Letters* **2015,** *40* (7).

145. Alam, M. Z.; Leon, I. D.; Boyd, R. W., Large optical nonlinearity of indium tin oxide in its epsilon-near-zero region. *Science* **2016,** *352*, 795.

146. Reshef, O.; Giese, E.; Zahirul Alam, M.; De Leon, I.; Upham, J.; Boyd, R. W., Beyond the perturbative description of the nonlinear optical response of low-index materials. *Opt Lett* **2017,** *42* (16), 3225-3228.

147. Yang, H. U.; D'Archangel, J.; Sundheimer, M. L.; Tucker, E.; Boreman, G. D.; Raschke, M. B., Optical dielectric function of silver. *Physical Review B* **2015,** *91* (23).

148. Smith, N. V.; Spicer, W. E., Photoemission Studies of the Alkali Metals. I. Sodium and Potassium. *Physical Review* **1969,** *188* (2), 593-605.

149. Smith, N. V.; Fisher, G. B., Photoemission Studies of the Alkali Metals. II. Rubidium and Cesium. *Physical Review B* **1971,** *3* (11), 3662-3670.

150. Gornyi, N. B.; Makarova, E. N., Detection of the plasmon photoeffect of alkali metals in photoelectron energy distribution curves. *Soviet Physics Journal* **1973,** *16* (10), 1406-1410.

151. Barman, S. R.; Horn, K., Photoemission study of electronic excitations at clean metal surfaces and thin metal films. *Applied Physics A* **1999,** *69* (5), 519-527.

152. Levinson, H. J.; Plummer, E. W., The surface photoeffect. *Phys. Rev. B* **1981,** *24* (2), 628.

153. Berglund, C. N.; Spicer, W. E., Photoemission Studies of Copper and Silver: Experiment. *Physical Review* **1964,** *136* (4A), A1044-A1064.

154. Barman, S. R.; Horn, K.; Häberle, P.; Ishida, H.; Liebsch, A., Photoinduced plasmon excitations in alkali-metal overlayers. *Physical Review B* **1998,** *57* (11), 6662-6665.

155. Krasovskii, E. E.; Silkin, V. M.; Nazarov, V. U.; Echenique, P. M.; Chulkov, E. V., Dielectric screening and band-structure effects in low-energy photoemission. *Physical Review B* **2010,** *82* (12).

156. Hopfield, J. J., Effect of Electron-Electron Interactions on Photoemission in Simple Metals. *Physical Review* **1965,** *139* (2A), A419-A424.

157. Barman, S. R.; Biswas, C.; Horn, K., Electronic excitations on silver surfaces. *Phys. Rev. B* **2004,** *69* (4), 045413.

158. Barman, S. R.; Biswas, C.; Horn, K., Collective excitations on silver surfaces studied by photoyield. *Surface Science* **2004,** *566-568*, 538-543.

159. Sipe, J. E., The ATR spectra of multipole surface plasmons. *Surface Science* **1979,** *84* (1), 75-105.

160. Raseev, G., Plasmon resonances of Ag(001) and Ag(111) studied by power density absorption and photoyield. *Surface Science* **2013,** *615*, 6-20.

161. Moresco, F.; Rocca, M.; Zielasek, V.; Hildebrandt, T.; Henzler, M., Evidence for the presence of the multipole plasmon mode on Ag surfaces. *Phys. Rev. B* **1996,** *54* (20), R14333-R14336.

162. Tsuei, K. D.; Plummer, E. W.; Liebsch, A.; Pehlke, E.; Kempa, K.; Bakshi, P., The normal modes at the surface of simple metals. *Surface Science* **1991,** *247* (2-3), 302-326.

163. Silkin, V. M.; Lazić, P.; Došlić, N.; Petek, H.; Gumhalter, B., Ultrafast electronic response of Ag(111) and Cu(111) surfaces: From early excitonic transients to saturated image potential. *Physical Review B* **2015,** *92* (15), 155405.

164. Velic, D.; Knoesel, E.; Wolf, M., Observation of a direct transition in the sp-band of Cu(111) and (√3x √3)R30° -CO/Cu(111) in one- and two-photon photoemission. *Surf. Sci.* **1999,** *424* (1), 1-6.

165. Bartynski, R. A.; Jensen, E.; Gustafsson, T.; Plummer, E. W., Angle-resolved photoemission investigation of the electronic structure of Be: Surface states. *Physical Review B* **1985,** *32* (4), 1921-1926.

166. Marks, M.; Schöll, A.; Höfer, U., Formation of metal–organic interface states studied with 2PPE. *J. Electron. Spectrosc. Relat. Phenom.* **2014,** *195* (0), 263-271.

167. Politano, A.; Formoso, V.; Chiarello, G., Collective Electronic Excitations in Thin Ag Films on Ni(111). *Plasmonics* **2013,** *8* (4), 1683-1690.

168. Nazarov, V. U.; Silkin, V. M.; Krasovskii, E. E., Role of the kinematics of probing electrons in electron energy-loss spectroscopy of solid surfaces. *Physical Review B* **2016,** *93* (3).

169. Saavedra, J. R. M.; Asenjo-Garcia, A.; García de Abajo, F. J., Hot-Electron Dynamics and Thermalization in Small Metallic Nanoparticles. *ACS Photon* **2016,** *3* (9), 1637-1646.

170. Phillips, J. C., Further Evidence for Collective Resonances in Monovalent Metals. *Physical Review* **1965,** *137* (6A), A1835-A1838.

171. Berglund, C. N.; Spicer, W. E., Photoemission Studies of Copper and Silver: Theory. *Physical Review* **1964,** *136* (4A), A1030-A1044.

172. Wang, L.-M.; Sametoglu, V.; Winkelmann, A.; Zhao, J.; Petek, H., Two-Photon Photoemission Study of the Coverage-Dependent Electronic Structure of Chemisorbed Alkali Atoms on a Ag(111) Surface. *J. Phys. Chem. A* **2011,** *115* (34), 9479-9484.

173. Marks, M. Ueber die Dynamik von Elektronen auf Silber-Einkristalloberflaechen, an metall-organischen Grenzschichten und in PTCDA-Monolagen. Ph.D. thesis, Philipps-Universitaet Marburg, Marburg, Germany, 2012.

174. Ogawa, S.; Nagano, H.; Petek, H., Hot-electron dynamics at Cu(100), Cu(110) and Cu(111) surfaces: comparison of experiment with Fermi liquid theory. *Phys. Rev. B* **1997,** *55* (16), 10869-10877.

175. Khurgin, J. B.; Boltasseva, A., Reflecting upon the losses in plasmonics and metamaterials. *MRS Bulletin* **2012,** *37* (8), 768-779.

176. Kliewer, K. L., Surface photoeffect for metals. *Physical Review B* **1976,** *14* (4), 1412-1428.

177. Apell, P.; Ljungbert, Å., A General Non-Local Theory for the Electromagnetic Response of a Small Metal Particle. *Physica Scripta* **1982,** *26* (2), 113-118.

178. Sonoda, Y., Electronic states of Cu(110) investigated with angle-resolved two-photon photoemission spectroscopy. *Physical Review B* **2011,** *83* (24), 245410.

179. Hirayama, M.; Okugawa, R.; Miyake, T.; Murakami, S., Topological Dirac nodal lines and surface charges in fcc alkaline earth metals. *Nat Commun* **2017,** *8*, 14022.

180. Shao, Y.; Rudenko, A. N.; Hu, J.; Sun, Z.; Zhu, Y.; Moon, S.; Millis, A. J.; Yuan, S.; Lichtenstein, A. I.; Smirnov, D.; Mao, Z. Q.; Katsnelson, M. I.; Basov, D. N., Electronic correlations in nodal-line semimetals. *Nature Physics* **2020,** *16* (6), 636-641.

181. Mele, E. J., Dowsing for nodal lines in a topological semimetal. *Proc Natl Acad Sci U S A* **2019,** *116* (4), 1084-1086.

182. Petek, H.; Nagano, H.; Weida, M. J.; Ogawa, S., The role of Auger decay in hot electron excitation in copper. *Chemical Physics* **2000,** *251* (1-3), 71-86.

183. Petek, H.; Heberle, A. P.; Nessler, W.; Nagano, H.; Kubota, S.; Matsunami, S.; Moriya, N.; Ogawa, S., Optical Phase Control of Coherent Electron Dynamics in Metals. *Physical Review Letters* **1997,** *79* (23), 4649-4652.

184. Nessler, W.; Ogawa, S.; Nagano, H.; Petek, H.; Shimoyama, J.; Nakayama, Y.; Kishio, K., Femtosecond Time-Resolved Study of the Energy and Temperature Dependence of Hot-Electron Lifetimes inBi2Sr2CaCu2O8+δ. *Physical Review Letters* **1998,** *81* (20), 4480-4483.

185. Trebino, R., *Frequency-Resolved Optical Gating: The Measurement of Ultrashort Laser Pulses*. Springer US: New York, 2000.

186. Anderson, A.; Deryckx, K. S.; Xu, X. G.; Steinmeyer, G.; Raschke, M. B., Few-Femtosecond Plasmon Dephasing of a Single Metallic Nanostructure from Optical Response Function Reconstruction by Interferometric Frequency Resolved Optical Gating. *Nano Lett.* **2010,** *10* (7), 2519-2524.

187. Mascheck, M.; Schmidt, S.; Silies, M.; Yatsui, T.; Kitamura, K.; Ohtsu, M.; Leipold, D.; Runge, E.; Lienau, C., Observing the localization of light in space and time by ultrafast second-harmonic microscopy. *Nature Photonics* **2012,** *6* (5), 293-298.

188. Mauritsson, J.; Remetter, T.; Swoboda, M.; Klunder, K.; L'Huillier, A.; Schafer, K. J.; Ghafur, O.; Kelkensberg, F.; Siu, W.; Johnsson, P.; Vrakking, M. J.; Znakovskaya, I.; Uphues, T.; Zherebtsov, S.; Kling, M. F.; Lepine, F.; Benedetti, E.; Ferrari, F.; Sansone, G.; Nisoli, M., Attosecond electron spectroscopy using a novel interferometric pump-probe technique. *Phys Rev Lett* **2010,** *105* (5), 053001.

189. Tan, S.; Argondizzo, A.; Wang, C.; Cui, X.; Petek, H., Ultrafast Multiphoton Thermionic Photoemission from Graphite. *Physical Review X* **2017,** *7* (1).

190. Smith, N. V., Classical generalization of the Drude formula for the optical conductivity. *Phys. Rev. B* **2001,** *64* (15), 155106.

191. Banfi, F.; Giannetti, C.; Ferrini, G.; Galimberti, G.; Pagliara, S.; Fausti, D.; Parmigiani, F., Experimental Evidence of Above-Threshold Photoemission in Solids. *Phys. Rev. Lett.* **2005,** *94* (3), 037601.

192. Timm, C.; Bennemann, K. H., Response theory for time-resolved second-harmonic generation and two-photon photoemission. *Journal of Physics: Condensed Matter* **2004,** *16* (4), 661-694.

193. Weida, M. J.; Ogawa, S.; Nagano, H.; Petek, H., Parallel excitation pathways in ultrafast interferometric pump-probe correlation measurements of hot-electron lifetimes in metals. *Appl. Phys. A* **2000,** *71* (5), 553-559.

194. de la Torre, A.; Kennes, D. M.; Claassen, M.; Gerber, S.; McIver, J. W.; Sentef, M. A., Colloquium: Nonthermal pathways to ultrafast control in quantum materials. *Reviews of Modern Physics* **2021,** *93* (4).

195. Higuchi, T.; Stockman, M. I.; Hommelhoff, P., Strong-Field Perspective on High-Harmonic Radiation from Bulk Solids. *Physical Review Letters* **2014,** *113* (21), 213901.

196. Krüger, M.; Schenk, M.; Hommelhoff, P., Attosecond control of electrons emitted from a nanoscale metal tip. *Nature* **2011,** *475* (7354), 78-81.

197. Cerullo, G.; De Silvestri, S., Ultrafast optical parametric amplifiers. *Review of Scientific Instruments* **2003,** *74* (1), 1-18.

198. Reutzel, M.; Li, A.; Wang, Z.; Petek, H., Coherent multidimensional photoelectron spectroscopy of ultrafast quasiparticle dressing by light. *Nat Commun* **2020,** *11* (1), 2230.

199. Oka, T.; Kitamura, S., Floquet Engineering of Quantum Materials. *Annual Review of Condensed Matter Physics* **2019,** *10* (1), 387-408.

200. De Giovannini, U.; Hübener, H.; Rubio, A., Monitoring Electron-Photon Dressing in WSe_2. *Nano Letters* **2016,** *16* (12), 7993-7998.

201. Sie, E. J.; McIver, J. W.; Lee, Y.-H.; Fu, L.; Kong, J.; Gedik, N., Valley-selective optical Stark effect in monolayer WS_2. *Nature Materials* **2014,** *14*, 290.

202. Fröhlich, D.; Nöthe, A.; Reimann, K., Observation of the Resonant Optical Stark Effect in a Semiconductor. *Physical Review Letters* **1985,** *55* (12), 1335-1337.

203. Mücke, O. D.; Tritschler, T.; Wegener, M.; Morgner, U.; Kärtner, F. X., Signatures of Carrier-Wave Rabi Flopping in GaAs. *Physical Review Letters* **2001,** *87* (5), 057401.

204. Mahmood, F.; Chan, C.-K.; Alpichshev, Z.; Gardner, D.; Lee, Y.; Lee, P. A.; Gedik, N., Selective scattering between Floquet-Bloch and Volkov states in a topological insulator. *Nat Phys* **2016,** *12* (4), 306-310.

205. Mücke, O. D.; Tritschler, T.; Wegener, M.; Morgner, U.; Kärtner, F. X., Role of the Carrier-Envelope Offset Phase of Few-Cycle Pulses in Nonperturbative Resonant Nonlinear Optics. *Physical Review Letters* **2002,** *89* (12), 127401.

206. Mucke, O. D.; Tritschler, T.; Wegener, M.; Morgner, U.; Kartner, F. X.; Khitrova, G.; Gibbs, H. M., Carrier-wave Rabi flopping: role of the carrier-envelope phase. *Opt Lett* **2004,** *29* (18), 2160-2.

207. Shirley, J. H., Solution of the Schrödinger Equation with a Hamiltonian Periodic in Time. *Physical Review* **1965,** *138* (4B), B979-B987.

208. Earl, S. K.; Conway, M. A.; Muir, J. B.; Wurdack, M.; Ostrovskaya, E. A.; Tollerud, J. O.; Davis, J. A., Coherent dynamics of Floquet-Bloch states in monolayer WS2 reveals fast adiabatic switching. *Physical Review B* **2021,** *104* (6).

209. Wang, Y. H.; Steinberg, H.; Jarillo-Herrero, P.; Gedik, N., Observation of Floquet-Bloch states on the surface of a topological insulator. *Science* **2013,** *342* (6157), 453-7.

210. Krüger, M.; Schenk, M.; Förster, M.; Hommelhoff, P., Attosecond physics in photoemission from a metal nanotip. *Journal of Physics B: Atomic, Molecular and Optical Physics* **2012,** *45* (7).

211. Fleischhauer, M.; Imamoglu, A.; Marangos, J. P., Electromagnetically induced transparency: Optics in coherent media. *Reviews of Modern Physics* **2005,** *77* (2), 633-673.

212. Hosseini, S. A.; Goswami, D., Coherent control of multiphoton transitions with femtosecond pulse shaping. *Physical Review A* **2001,** *64* (3).

213. Dil, J. H.; Meier, F.; Osterwalder, J., Rashba-type spin splitting and spin interference of the Cu(1 1 1) surface state at room temperature. *Journal of Electron Spectroscopy and Related Phenomena* **2015,** *201*, 42-46.

214. Höfer, U.; Shumay, I. L.; Reuß, C.; Thomann, U.; Wallauer, W.; Fauster, T., Time-Resolved Coherent Photoelectron Spectroscopy of Quantized Electronic States on Metal Surfaces. *Science* **1997,** *277* (5331), 1480-1482.